University of California
Santa Barbara

Geometry and Topology of Soft Elastic Systems

A dissertation submitted in partial satisfaction
of the requirements for the degree

Doctor of Philosophy

in

Physics

by

Roberto Abril Valenzuela

Committee in charge:

      Professor Mark J. Bowick, Co-chair
      Professor Sebastian Streichan, Co-chair
      Professor Cristina Marchetti

September 2024

The Dissertation of Roberto Abril Valenzuela is approved.

_____

Professor Cristina Marchetti

_____

Professor Sebastian Streichan , Committee Co-chair

_____

Professor Mark J. Bowick, Committee Co-chair

August 2024

Geometry and Topology of Soft Elastic Systems

Copyright © 2024

by

Roberto Abril Valenzuela

Para mi familia

Acknowledgements

During the span of my graduate career, I experienced some of the highest and lowest points of my life, and the scales for both ends of the spectrum were positively shifted because of the people who were involved in my life during this time.

First and foremost, I have the deepest of gratitude to my advisor, Mark Bowick. Mark was my introduction to the soft matter field and his enthusiasm for physics made me want to learn about a field that I previously had not even considered going into and it inspires me to have a better outlook on science in general. Mark's incredible guidance, patience, and support were essential for my completion of this degree. Secondly, Cristina Marchetti for serving as part of my committee and for welcoming me into her weekly group meetings. Along these lines, I would also like to thank the Marchetti group members Toshi Parmar, Paarth Gulathi, Austin Hopkins, Zhitao Chen, and Arthur Hernandez for the discussions and for allowing me to feel like I'm part of a large theory group. I would also like to thank Sebastian Streichan for also being part of my committee and for his overall positive presence in the 6th floor of Broida and the soft matter community.

I owe my mental stability to all the friends who have been part of my life during the toughest years of my studies. My housemates and close friends Rémi Boros, Toshi Parmar, David Scully, Eric Rind, and John Berezney for countless moments of joy and laughter over the past 4 years. My college friends Sergio Aguayo, Jesus Aguilar, Nick Rubio, Roger Martinez Reyes, and Blayne Wagner for staying in contact despite no longer seeing each other as often as we once did. To the people who made the first-year trailer an enjoyable experience: Ryan Schmitz, Adolfo Holguin, Michael Oshiro, Mina Lee, and Erin Yandel to name a few.

Last but not least, a toda mi famila. Mil gracias a todos los que estuvieron presentes y ayudaron en cada paso de mi carrera. Sin el apoyo de mi Máma nada de esto hubiera

sido posible. Muchas gracias por todo tu amor y apoyo. A mi Pápa muchas gracias por todas tus llamadas semanales y por darme el animo que siempre ocupo para continuar.

Roberto Abril Valenzuela

Curriculum Vitae

Roberto Abril Valenzuela
☎ +1 (619) 548 6197
✉ roberto9601@gmail.com
🌐 rabril.github.io

Education

University of California, Santa Barbara

Ph.D. in Physics	In progress
M.Sc. in Physics	Sept. 2019 - Sept. 2021

Thesis: *Geometry and Topology of Soft Elastic Systems*
Advisor: Mark J. Bowick

California Polytechnic State University, San Luis Obispo

B.Sc. in Physics	Sept. 2014 - June 2018
B.Sc. in Mathematics	Sept. 2014 - June 2018

Bachelor's Thesis: *Simulating the Electrical Properties of Random Carbon Nanotube Networks Using a Simple Model Based on Percolation Theory*
Advisor: Colleen A. Marlow

Publications

• Jin-Sheng Wu, **Roberto Abril Valenzuela**, Mark J. Bowick, and Ivan I. Smalyukh. Non-abelian defect junctions in chiral nematic systems with biaxial symmetry. *In preparation*.

• **Roberto Abril Valenzuela**, Paul Z. Hanakata, and Mark J. Bowick. Geometric control of tilt transition dynamics in single-clamped thermalized elastic sheets. *Phys. Rev. E*, 108:045002, Oct 2023.

• Leo A. Browning, William Watterson, Erica Happe, Savannah Silva, **Roberto Abril Valenzuela**, Julian Smith, Marissa P. Dierkes, Richard P. Taylor, Natalie O. V. Plank, and Colleen A. Marlow. Investigation of fractal carbon nanotube networks for biophilic neural sensing applications. *Nanomaterials*, 11(3), 2021.

Presentations

• *Topologically stable links and biaxiality in chiral nematic systems*, Roberto Abril Valenzuela, Jin-Sheng Wu, Ivan Smalyukh, Mark J. Bowick (*APS March Meeting Minneapolis,*

2024)

• *Geometrical Control of the Tilt Transition in Single-Clamped Thermalized Elastic Sheets*, Roberto Abril Valenzuela, Mark J. Bowick (*APS March meeting Las Vegas, 2023*)

• *Classifying Non-trivial Links of Biaxial Nematic Defect Lines*, Roberto Abril Valenzuela, Jin-Sheng Wu, Ivan Smalyukh, Mark J. Bowick (*APS March Meeting Chicago, 2022*)

Research Interests

Geometry and topology in soft matter systems, elasticity of sheets and membranes, physical and mathematical modeling of biological systems, dynamical systems, machine learning

Awards

• Louis Stokes Alliance for Minority Participation Bridge to the Doctorate fellowship recipient (2018)

Teaching

Learning Assistant in Chemistry (Cal Poly, SLO)

CHEM 127 General Chemistry for Agriculture and Life Science I	Fall 2015
CHEM 124 General Chemistry for Physical Science and Engineering I	Winter 2016
CHEM 124 General Chemistry for Physical Science and Engineering I	Spring 2016

Workshop Assistant in Math (Cal Poly, SLO)

MATH 241 - Calculus IV	Fall 2016
MATH 241 - Calculus IV	Winter 2017
MATH 244 - Linear Analysis I	Spring 2017
MATH 244 - Linear Analysis I	Fall 2017
MATH 244 - Linear Analysis I	Winter 2018
MATH 241 - Calculus IV	Spring 2018

Teaching Assistant (Cal Poly, SLO)

PHYS 202 - Physics on the Computer	Winter 2018

Teaching Assistant (UCSB)

PHYS 128AL - Advanced Experimental Physics	Summer 2024

Outreach

○ Physics Incoming Student Mentor Program, *Mentor* (2020-2021)

- ○ "Thriving, Not Surviving: Navigating Higher Education as a First Generation Student", *Panelist* (2019)
- ○ Physics Circus (2018)

Technical Skills

Programming: Python, C++, MATLAB, Mathematica, LaTeX

Packages & Libraries: HOOMD-blue, LAMMPS, FEniCS, Dedalus

Abstract

Geometry and Topology of Soft Elastic Systems

by

Roberto Abril Valenzuela

We study two separate systems each of which emphasizes the geometrical and topological aspects of soft condensed matter systems. The geometry side of condensed matter is exemplified by the geometrical frustration experienced by constrained thermalized membranes. We study the dynamics of the novel tilted phase of thermalized cantilevers and find that the geometry of the system plays an important role in determining the behavior of the underdamped dynamics. We then delve into the topology of soft matter by studying the non-Abelian braiding of singular defect lines of systems with biaxial symmetry. Biaxial nematic defects have a non-Abelian topology that allows for the formation of topologically stable braided structures. We devise a braid theory that incorporates strand labeling via colors and allows for crossing relations that take colorings into account. We use this colored braid theory to translate complex braided structures into algebraic expressions that can be used to determine whether the braid is entangled under the algebra of its assigned fundamental group. We supplement this with possible experimental realizations of the non-Abelian structures inherent to the biaxial nematic system.

Contents

Chapter 1

Introduction

In this dissertation, we will explore problems in soft matter systems that are not inherently "soft" in the traditional sense of the word. Soft matter systems are often characterized by energy scales comparable to that of the system's temperature. In other words, soft matter systems are those in which entropic effects will dominate. Such systems have been thoroughly studied for over a century now for their vast applications in fields of statistical mechanics and their success in explaining several problems in material physics. Soft matter problems can span several length scales and- from the microscale in the modeling of biological systems such as morphogenesis and tissue mechanics [1, 2], to the macroscale in the active dynamics of flocking [3].

We will focus on two separate topics: the dynamics of constrained thermalized membranes and the classification of knots and links of biaxial nematic defect lines. The former will elucidate the role of geometry in the dynamics of a thin, elastic solid at finite temperatures while the latter will showcase the rich topology that is tied to biaxial nematic systems and their singular disclination lines.
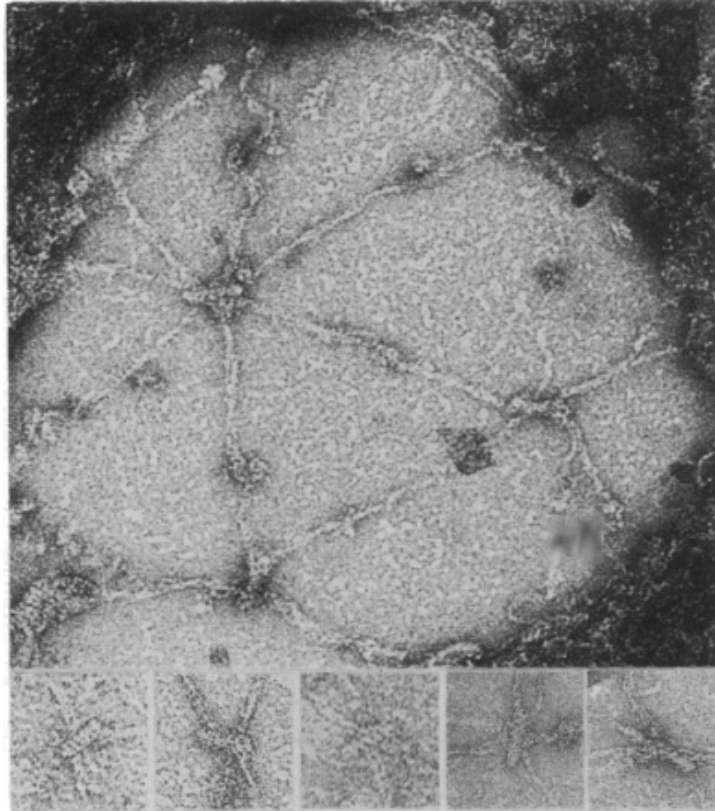
Figure 1.1: Magnified electron micrograph of a "ghost" erythrocyte cytoskeleton obtained by removing the surrounding lipid bilayer. Figure adapted from [4].

1.1 Statistical Mechanics of Crystalline Membranes

The physics of thin plates with thickness t much smaller than the length of the system, L, has been predominantly studied within continuum mechanics for decades [5]. From studying their elastic properties and vibrational modes [6], one might think the classical mechanics of plates and shells has nothing more to reveal. Interest in the mechanics of thin sheets has been rekindled recently in fields such as metamaterials [7, 8, 9] and biology, where one finds many examples of two-dimensional plate-like systems [10, 11, 12], more appropriately referred to as a membranes. In classical mechanics, scales are large enough where the effect of thermal fluctuations can be ignored. Biological membranes, however, are often subject to media where external fluctuations significantly impact the

2

physics.

The model systems for thermalized membranes, both solid and liquid, are often mo-
tivated by biological systems. Lipid membranes are prime examples of liquid membranes
while the two-dimensional cytoskeletal cortex structures in red cell membranes, which can
be separated from the lipid layer [11, 4], are that of solid membranes [12], an experimen-
tally imaged isolated sample of which can be seen in Fig. 1.1. Both of these examples have
elastic properties that are modified by thermal fluctuations. In the presence of such large
thermal fluctuations the elastic properties of the system become scale-dependent. As we
will later explain, this scale dependency, becomes ubiquitous in the study of membranes
at non-zero temperature.

Perhaps unsurprisingly, the interest in solid membranes, specifically, has been rekin-
dled in the last decade due to the emergence of graphene as a wonder material with
manifold applications in physics and materials engineering. There has been no short-
age of research on the electronic properties of graphene over the last few decades. The
elastic properties of graphene, however, have been much less explored and provide a rich
playground for extreme mechanics at finite temperatures. Room temperature graphene
is an experimentally accessible system to probe the elastic properties of thermalized solid
membranes, however, the same physical analysis applies to a vast number of 2D meta-
materials. Taking graphene as our membrane of choice, we will focus on the mechanical
properties of solid membranes.

I will now introduce the most commonly used model of the continuum elastic proper-
ties of a two-dimensional membrane or sheet embedded in an ambient space $\mathbb{R}^3$. Consider
an initially flat sheet configuration on the plane, $\mathbf{r}_0 = (x_1, x_2, 0)$. A distortion, $\mathbf{r}'$, on this
flat state can then be parametrized using the Monge parametrization [13]:

$$\mathbf{r}(\mathbf{x}, h) = \mathbf{r}_0 + \mathbf{r}' = (x_i + u_i(\mathbf{x}))\hat{e}_i + h(\mathbf{x})\hat{e}_3 \qquad (1.1)$$
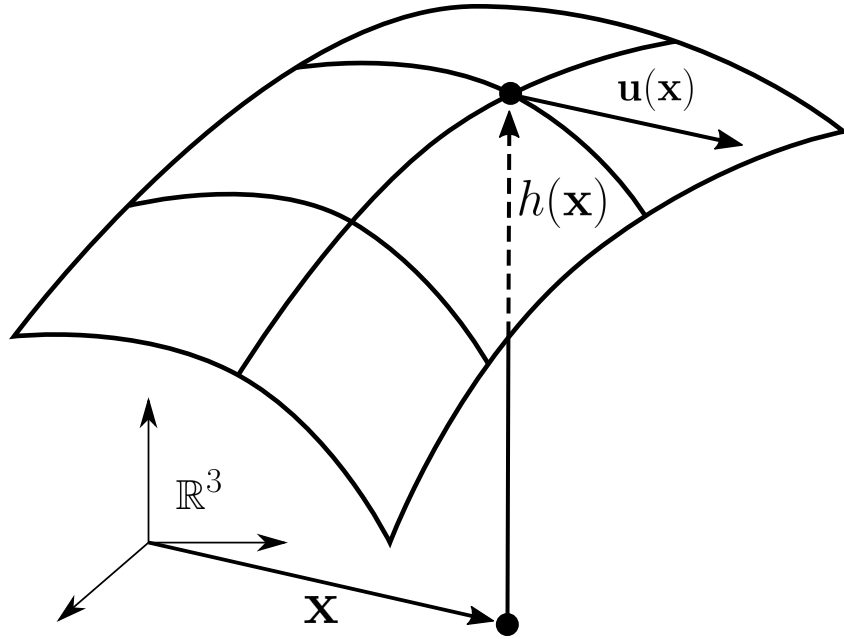
Figure 1.2: Relevant fields in the continuum model of elastic sheets in 3D. The in-plane field, $\mathbf{u}(\mathbf{x})$, measures displacements in the plane of the sheet while the out-of-plane field, $h(\mathbf{x})$, measures the displacements in the dimension transverse to the sheet.

where $i = 1, 2$. Here, there are two continuum fields of interest: (1) a vector in-plane displacement field $\mathbf{u}(\mathbf{x}) \in \mathbb{R}^2$ and (2) a scalar out-of-plane displacement field $h(\mathbf{x}) \in \mathbb{R}$, both of which are pictorially depicted in Fig. 1.2. We can then measure infinitesimal distortions of a line segment, $d\mathbf{r}$, and write down the metric for the sheet,

$$\mathrm{d}r^2 = dr_0^2 + 2u_{ij}dx_i dx_j, \tag{1.2}$$

where u_{ij} is the so-called non-linear strain tensor, which, to lowest order in gradients of u_i and h, is given by

$$u_{ij} \approx \frac{1}{2}\left(\partial_i u_j + \partial_j u_i\right) + \frac{1}{2}\partial_i h \partial_j h. \tag{1.3}$$

Note that the second term of the strain tensor provides a non-linear contribution which separates the mechanics of 3D materials from those of 2D sheets in $\mathbb{R}^3$. This non-linearity manifests itself in several forms, but most important of all is the long-range interaction

4

of out-of-plane fluctuations.

The energy of an elastic sheet configuration can now be formulated to have two main contributions: an energetic cost to bending and an energetic cost to stretching. This takes the form [5, 13]

$$\mathcal{F}[h(\mathbf{x}), \mathbf{u}(\mathbf{x})] = \int d^2\mathbf{x} \left(\frac{\kappa}{2}(\nabla^2 h)^2 + \mu u_{ij}^2 + \frac{\lambda}{2} u_{kk}^2 \right) \tag{1.4}$$

where the energy of bending is mediated by a bending rigidity, κ, physically penalizing local changes of Gaussian curvature, $\nabla^2 h$, and has units of energy. On the other hand, stretching is measured through the non-linear strain tensor and mediated by the so-called Lamé coefficients, μ and λ, which have units of energy per unit area. The equilibrium equations of plates, better known as the Föppl-von Kármán equations, can then be derived via variation of the free energy above ($\delta\mathcal{F} = 0$). The resulting equations are non-linear and biharmonic, meaning they are a set of fourth-order partial differential equations that are extremely difficult to solve with scarce analytic solutions [5].

We have assumed zero-temperature so far. In order to study the statistical mechanics of membranes, however, we must analyze the partition function given by the free energy Eq. 1.4. This takes the form of the following functional integral[1]

$$Z = \iint \mathcal{D}h\,\mathcal{D}\mathbf{u}\,e^{-\mathcal{F}[h,\mathbf{u}]/k_B T}. \tag{1.5}$$

In this form, we can simplify the model by noting that the in-plane modes, u_i, appear quadratically in $\mathcal{F}$. This means that the u_i integral is Gaussian and can be integrated

---

[1]Note that we have written this in terms of a free energy and not as energy. This is because we can partition the sum over all different configurations into a sum over groups of configurations with the same energy levels; that is, $Z = \sum_i e^{-E_i/k_B T} = \sum_E \Omega(E)e^{-E/k_B T}$ where $\Omega(E) = e^{S/k_B}$ is the degeneracy of the configuration with energy E.

to derive an effective theory in h; that is we write

$$\mathcal{F}_{\text{eff}}[h(\mathbf{x})] = -k_B T \ln \int \mathcal{D}u_i \, e^{-\mathcal{F}[h(\mathbf{x}), \mathbf{u}(\mathbf{x})]/k_B T}, \tag{1.6}$$

which, after integration (see Appendix A for the details), yields the effective theory

$$\mathcal{F}_{\text{eff}}[h(\mathbf{x})] = \int d^2\mathbf{x} \left(\frac{\kappa}{2} \left(\nabla^2 h(\mathbf{x}) \right)^2 + \frac{Y}{8} (P_{ij}^T \partial_i h \partial_j h)^2 \right), \tag{1.7}$$

where $P_{ij}^T = \delta_{ij} - \partial_i \partial_j / \nabla^2$ is the transverse projection operator and we have also introduced the 2D Young's modulus, Y,

$$Y = \frac{4\mu(\mu + \lambda)}{2\mu + \lambda}, \tag{1.8}$$

which measures a material's bulk resistance to strain due to applied forces. In this form, the model now presents the non-linearity in the strain tensor upfront in the form of a quartic term, making the effective energy resemble that of a ϕ^4 model.

Now that we have a $T > 0$ theory with one field, we can study the role of thermal fluctuations, which, in a solid membrane, play an essential role in modifying the elastic properties. To see this, consider the height-height correlator, which in the Gaussian theory ($Y = 0$) in Fourier space reads

$$\langle h(q)h(-q) \rangle_0 = \frac{k_B T}{A\kappa q^4}, \tag{1.9}$$

where A is the area of the sheet and $\langle \cdot \rangle_0$ denotes the Gaussian average. Allowing now $Y \neq 0$, we write the correlator

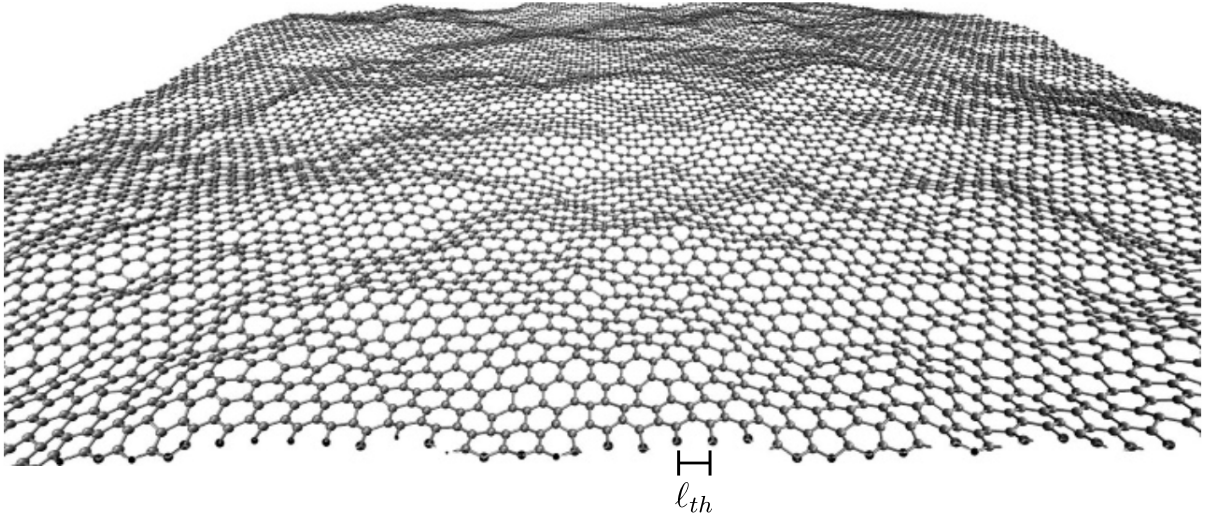$$\langle h(q)h(-q) \rangle = \frac{k_B T}{A\kappa_R(q)q^4}, \tag{1.10}$$

Figure 1.3: Finite temperature configuration of a simulated free-standing sheet of graphene [15]. Scale bar shows the relative size of the thermal lengthscale, $\ell_{th} \approx 2$ Å.

where the correction provided by the non-linear stretching term is said to *renormalize* the bending rigidity, defining the renormalized, scale-dependent bending rigidity

$$\kappa_R(q) = \frac{k_B T}{q^4 \langle h(q)h(-q)\rangle}. \tag{1.11}$$

A self-consistent approach leads a solution for κ_R which has the scaling form [14],

$$\kappa_R(q) \sim q^{-1}, \tag{1.12}$$

which tells us how thermal fluctuations modify the bending rigidity. Such fluctuations, however, only become relevant beyond a certain lengthscale, referred to as the *thermal lengthscale*,

$$\ell_{th} = \sqrt{\frac{32\pi^3 \kappa_0^2}{3 K_B T Y_0}}, \tag{1.13}$$

for bare zero-temperature values κ_0, Y_0 (see Appendix B for a derivation).

More sophisticated approaches beyond the self-consistent approach, such as ϵ-expansions,

7

reveal that thermalized sheets are controlled by a Föppl-von Kármán fixed point where all the elastic constants are scale-dependent. That is, the bending and stretching moduli $\kappa(\ell), \mu(\ell), \lambda(\ell)$ are promoted to functions of the system size, ℓ as follows

$$\frac{\kappa_R(\ell)}{\kappa_0} \sim \left(\frac{\ell}{\ell_{th}}\right)^{\eta} \tag{1.14}$$

$$\frac{\mu(\ell)}{\mu_0}, \frac{\lambda(\ell)}{\lambda_0}, \frac{Y(\ell)}{Y_0} \sim \left(\frac{\ell}{\ell_{th}}\right)^{-\eta_u}, \tag{1.15}$$

where the anomalous exponent is estimated by both analytic calculations and simulations to be $\eta \approx 0.8$ [16, 17, 18, 19, 20, 21, 22] while the second exponent, η_u, is exactly related to η by the rotational invariance Ward identity (see Appendix C)

$$\eta_u = 2 - 2\eta, \tag{1.16}$$

yielding an estimate of $\eta_u \approx 0.4$. The renormalization group analysis tells us that, at scales beyond the thermal lengthscale ($\ell \gg \ell_{th}$), the bending rigidity increases and the system becomes *stiffer* to bending. At the same time, the stretching moduli decrease, meaning the stretching modes are *softened* by thermal fluctuations. This is a remarkable example of attaining order from disorder as states with higher thermal fluctuations tend to be stabilized into an extended or flat state. The mean square displacements of the height field due to thermal fluctuations is

$$\langle h^2 \rangle = \int \frac{d^2q}{(2\pi)^2} \langle h(q)h(-q) \rangle \sim L^{2-\eta} \equiv L^{2\zeta}, \tag{1.17}$$

where ζ is the roughness exponent and is approximated to be $\zeta \approx 0.6$ [13]. This tells us that the root-mean-square displacements scale as $h_{rms}/L = \sqrt{\langle h^2 \rangle}/L = L^{-\eta/2}$ which approaches zero as $L \to \infty$, indicating the system is flat but rough. It is this same rough-

ening of the membrane surface that helps explain the stabilization of graphene as a 2D crystal that "seemingly" violates the Mermin-Wagner theorem (see Fig. 1.3). The logic of Mermin-Wagner would lead one to believe that long wavelength modes would destroy the ordered phase as the mean square displacement diverges logarithmically with system size. The codimensionality of the surface once again allows out-of-plane fluctuations to interact at long ranges with the help of a bilaplacian mediator, thus circumventing the Mermin-Wagner restrictions. This stability only lasts until an inevitable crumpling transition at some critical temperature, $T_{\text{crumpling}}$, where disorder dominates and surface normals are no longer correlated.

In practice, the elastic properties of membranes can often be quantified using the Föppl-von Kármán number, which for system of size L, is given by

$$\text{vK} = YL^2/\kappa \tag{1.18}$$

and it roughly measures the relative importance of stretching versus bending. We may rewrite vK by writing $Y = Et$ and $\kappa = Et^3$, where E is the three dimensional Young's modulus and t the thickness of the membrane. This means that for any material, $\text{vK} \approx (L/t)^2$, which makes $\text{vK} \gg 1$ for $t \ll L$, generally indicating that stretching is more energetically costly than bending deformations, leading to F leading to bending domination in thin membranes. For the case of graphene, the microscopic elastic values are $\kappa \approx 1.2$ eV and $Y \approx 20$ eV Å^{-2}, which for a system size of order 100 μm gives $\text{vK} \approx 10^{12}$. What makes graphene, additionally special is that, the thermal lengthscale is of the order $\ell_{th} \sim 2$ Å, which is comparable to the thickness of a monolayer sample of graphene. This means that any experimental sample of graphene will be in the thermalized limit $\ell \gg \ell_{th}$ at low temperatures, which makes it an ideal material to study the properties of thermalized membranes experimentally. To put this into perspective, the

thermal lengthscale for a membrane such as the aforementioned red blood cytoskeleton is $\ell_{th} \approx 10 \ \mu$m which is slightly larger than the typical size of red blood cells $\ell \approx 8 \ \mu$m. On the same note, a more sizeable material like paper, has $\ell_{th} \approx 50$ km, meaning thermal fluctuations cannot be witnessed in a regular sheet of printer paper.

Chapter 2 of this thesis will make use of the membrane physics introduced in this section as applied to explain the rich dynamics of a symmetry-breaking phase transition, which we aptly refer to as the tilt transition. It can be thought of as a thermalized cantilever analog to the Euler buckling transition in classical elastic beam theory. We will see how the interplay between geometry and thermalization leads to a unique dynamic phase of tilting where, at the onset of transition, the system spontaneously chooses one of two available states but can dynamically "tunnel" into the opposite state. This is based on work published in [23].
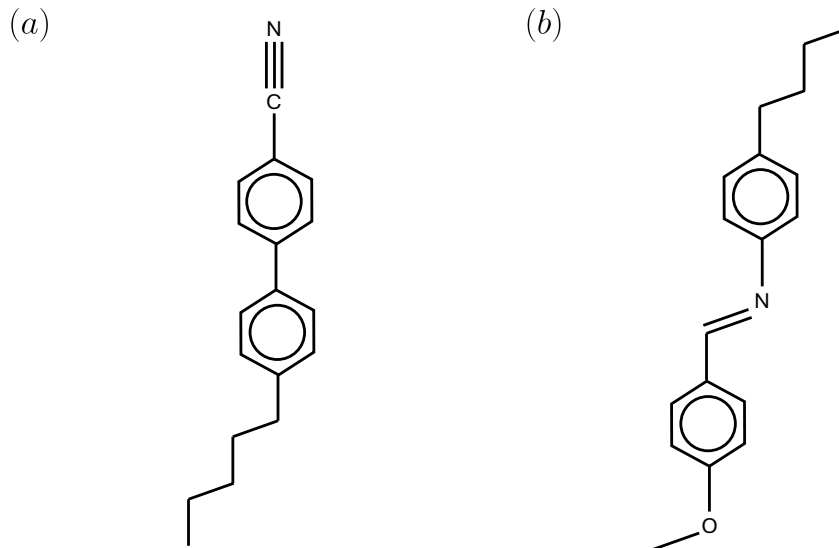

Figure 1.4: Molecular structure of the most commonly used nematic constituent molecules, (a) 5CB and (b) MBBA, both of which exhibit nematic transitions near room temperature. The latter is often used in liquid crystal displays (LCDs).

1.2   Topology of Biaxial Nematics

The second half of this thesis will focus on a different project that explores the rich topology of biaxial nematic systems.

Before introducing the biaxial system, it is instructive to consider its simpler cousin, the uniaxial nematic, one of the most thoroughly studied systems in soft condensed matter, due to its analytical simplicity coupled to its vast range of applications in other fields of physics [24], including biological physics systems such as the supracellular actin fiber networks in Hydra [25]. Nematics are known as the most basic phase of liquid crystal systems, which are aptly named as they flow like liquids but possess long-range elastic distortions like crystals. More complex phases exist, such as the layered smectic phase and the chiral nematic (cholesteric) phase with twisting layers [26]. Liquid crystals are composed of thin rod-like molecules such as 5CB and MBBA[2] (see Fig. 1.4) which have rod-like or cylindrical symmetry, D_∞, which is depicted in Fig 1.5. As they have no particular polarity, nematic molecules are often characterized by an angular orientation of a director $\mathbf{n}$, which is a unit vector with head-tail symmetry, that is, $\mathbf{n} = -\mathbf{n}$.

Biaxial nematics were first theoretically introduced about 50 years ago by Toulouse in his seminal paper where he described the system as a generalization of *uniaxial* nematic liquid crystals [27]. In his paper, Toulouse expands upon the rod-like symmetry of local geometries by considering constituent molecules with rectangular point-group symmetry, D_2, instead of rod-like symmetry, D_∞, of uniaxial molecules. Biaxial nematics, in that sense, follow a similar construction as uniaxial nematics and can be seen as an extension with reduced symmetry.

Consider an ensemble of molecules with the same rotational symmetry except now we consider the rectangle's rotational symmetry, D_2. One can think of biaxial molecules

---

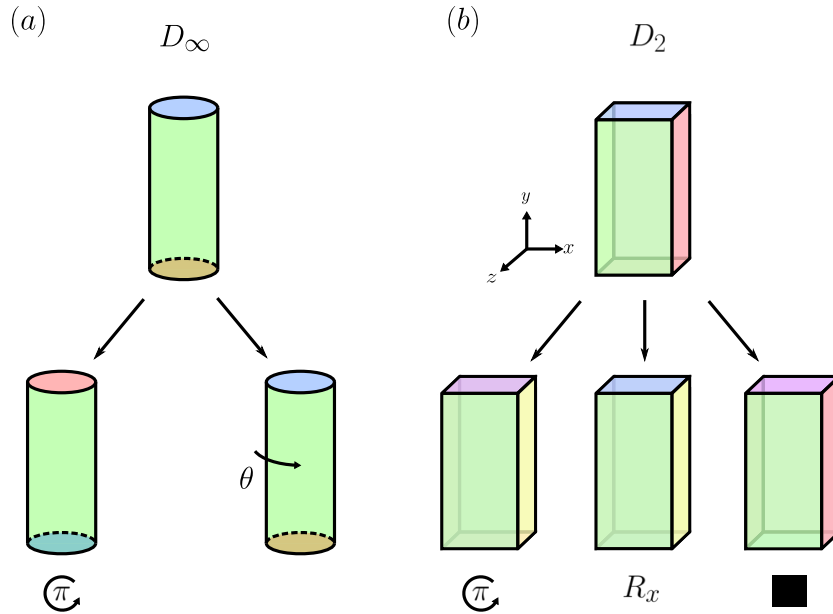[2]p-Pentyl-p'-Cyanobiphenyl and N-(p-Methoxybenzylidene)-p'-Butylaniline

Figure 1.5: (a) Visual representation of the symmetry group of uniaxial nematics, D_∞ which is generated by a reflection along the long axis of the rod (left) and an infinite set of rotations about the long axis parametrized by an angle, θ (right). (b) Visual representation of the 4-element symmetry group of biaxial nematics, D_2. This group is generated by a π rotation about the z-axis (left) and reflections along the x (middle) and y axes (right).

as "brick"-like constituents. Note that the group D_∞ is infinitely large, as its elements correspond to the reflection along the molecule's long axis as well as rotations around it, parametrized by an angle $\theta \in \mathbb{R}$ (see Fig. 1.5(a)). On the other hand, the rectangular group, D_2, is only generated by 3 non-trivial elements that correspond to a π rotation about the out-of-plane axis as well as reflections across the long and short axes (see Fig. 1.5(b)). Similar to the uniaxial director, the orientation of a biaxial molecule can be described using a triad of directors, $(\mathbf{n}, \mathbf{m}, \mathbf{l})$ each corresponding to a principal axis of

symmetry and all of which are unit length and obey

$$\mathbf{n} = -\mathbf{n} \tag{1.19}$$

$$\mathbf{m} = -\mathbf{m} \tag{1.20}$$

$$\mathbf{l} = -\mathbf{l}. \tag{1.21}$$

The orientational information of all three directors can be combined into a traceless-symmetric tensor, Q_{ij}, known simply as the Q-tensor. It has the form,

$$Q_{ij} = S\left(n_i n_j - \frac{\delta_{ij}}{3}\right) + T\left(m_i m_j - \frac{\delta_{ij}}{3}\right), \tag{1.22}$$

where S and T are the uniaxial and biaxial order parameters, respectively. Here, we can recover the uniaxial Q-tensor as simply the case where $T = 0$.

1.3   Topological Defects

Typically, one may consider global or average nematic configuration textures and their overall phase or alignment often characterizes the degree of order. However, at the local level, the orientation fields may become singular at a region in space. These singularities are what are known as topological defects, usually characterized by a topological invariant (charge), and may vary in dimensionality depending on the dimension of the system and the dimension of a measuring surface that encloses it.

Take for example a nematic in 2D which has a Q-tensor of the form

$$Q = \frac{1}{2}\begin{pmatrix} \cos\theta & \sin\theta \\ \sin\theta & -\cos\theta \end{pmatrix}, \tag{1.23}$$

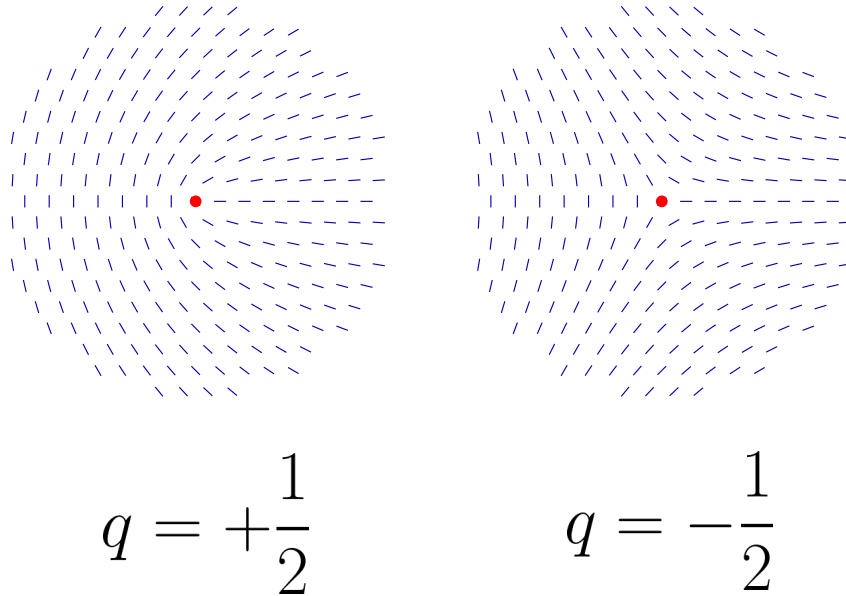$$q = +\frac{1}{2} \qquad\qquad q = -\frac{1}{2}$$

Figure 1.6: The two defect textures with equal and opposite winding numbers found in 2-dimensional uniaxial nematics. Note that in 3D, these would extend in the third dimension and the defect core would become a defect line.

where θ is the local orientation of the nematic. Topological point defects for this configuration would then present themselves as a singularity in θ and are characterized by a winding number $q \in \mathbb{Z}/2$ given by

$$2\pi q = \oint d\theta, \tag{1.24}$$

which simply measures the amount by which the angle θ winds around a circle that encloses the defect. 2D nematics are host to two fundamental point defect charges $q = \pm 1/2$, both of which are depicted in Figure 1.6. Higher winding number defects exist, however, these are more rare as they are higher in energy by a factor of $\sim q^2$.

In three dimensions, we may have line defects or disclinations, which are similarly described by a topological number, q, which measures the amount by which the angle rotates along a circuit surrounding the defect line. Note that we can still have point defects in 3D, however, the classification system using the winding number in 2D no

longer has any meaning, as we cannot draw a loop around a point in 3D. Instead, we must take a more sophisticated approach.

1.3.1   Homotopy group theory

Tuolouse and Kleman first introduced the topological classification of defects in [28] and then popularized by Mermin in his seminal review [29]. They applied the mathematical machinery of homotopy theory, which studies families of continuous mappings $h_t : X \longrightarrow Y$, known as homotopies between spaces X and Y, where $t \in [0, 1]$. The homotopy map, h_t, forms an equivalence relation, written as $\simeq$, between two spaces $h_0 = X$ and $h_1 = Y$ and they are said to be homotopic to each other. Topologically speaking, this forms a sense of topological equivalence between two topological spaces as one can just be deformed into the other without puncturing or gluing. If one chooses a familiar space for the space X such as the the n-sphere, $S^n = \{x \in \mathbb{R}^{n+1} \mid |x| = 1\}$, the set of equivalence classes of maps from $S^n \longrightarrow Y$, forms a group called the nth homotopy group, $\pi_n(Y)$.

In practice, for the space of allowed configurations known as the order parameter space, OP, the first homotopy group, more commonly referred to as the fundamental group, $\pi_1(OP)$, classifies the singularities of codimension 2 available in some order parameter space than can be enclosed by closed curves as shown in Fig. 1.7(a). Generally, the n-th homotopy group, $\pi_n(OP)$, classifies singularities of codimension $n + 1$ (i.e. dimension $D - n - 1$) which can be contained within n-spheres.

Let us take for example, 3D uniaxial nematics, whose order parameter space is given by all the allowed local rotations $(SO(3))$ that obey the symmetry of the molecule (D_∞), that is

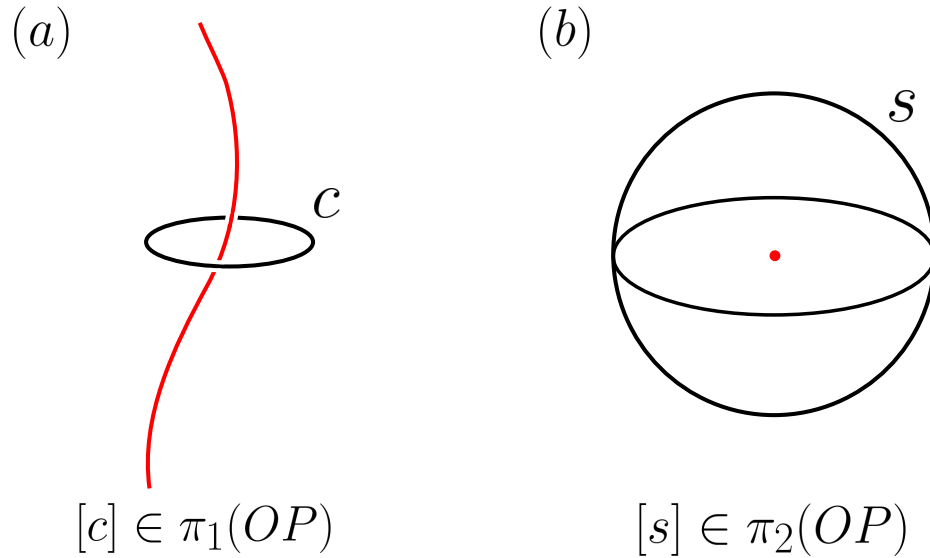$$OP_{\text{uniaxial}} = SO(3)/D_\infty \simeq S^2/\mathbb{Z}_2 \simeq \mathbb{RP}^2 \tag{1.25}$$

Figure 1.7:   In 3D, (a) a singular defect line classified by circular loop c whose equivalence classes up to homotopy, $[c]$, define the specific element by which the line is classified under the fundamental group, $\pi_1(OP)$. (b) A point defect surrounded by a sphere, s, is classified by the equivalence classes, $[s]$, in the second homotopy group, $\pi_2(OP)$.

where $\mathbb{RP}^2$ is the real projective plane (the set of all lines through the origin). Defect lines or disclinations are then classified by the fundamental group of the real projective plane,

$$\pi_1(\mathbb{RP}^2) = \mathbb{Z}_2. \tag{1.26}$$

This is an Abelian (commutative) group of order 2, which tells us that there is only one topologically distinct 1-dimensional defect other than the identity. In addition, the

16

second homotopy group, which classifies point defects is

$$\pi_2(\mathbb{RP}^2) = \mathbb{Z}. \tag{1.27}$$

meaning unit point charges exist in 3D uniaxial nematics. This group is also Abelian. In fact, only the fundamental group can be non-Abelian as all higher homotopy groups can be shown to always be either trivial or Abelian for any topological space [30].

In breaking azimuthal symmetry in the plane perpendicular to the constituent molecules' long axis, i.e $D_\infty \longrightarrow D_2$, we vastly reduce the available local degenerate states. This ultimately leads to exotic properties in the singular defects that become topologically accessible to biaxial systems in three dimensions. On that note, biaxial disclinations are have an order parameter space given by

$$OP_{\text{biaxial}} = SO(3)/D_2. \tag{1.28}$$

The corresponding fundamental group is then

$$\pi_1(SO(3)/D_2) \simeq \pi_1(SU(2)/\mathbb{Q}) = \mathbb{Q}, \tag{1.29}$$

where $\mathbb{Q} = \{\pm 1, \pm i, \pm j, \pm k\}$ is the group of quaternions, which is non-Abelian ($ij = k \neq ji$). The proof of this statement is quite lengthy but can be summarized in the following short exact sequence [30]

$$0 \longrightarrow \pi_1(SU(2)) \longrightarrow \pi_1(SU(2)/\mathbb{Q}) \longrightarrow \pi_0(\mathbb{Q}) \simeq \mathbb{Q} \longrightarrow 0, \tag{1.30}$$

along with the fact that $\pi_1(SU(2)) \simeq \pi_1(S^3) = 0$. A sketch of the full proof is given in Appendix F. Here the crucial distinction between the uniaxial and biaxial systems is

that the biaxial fundamental group is non-Abelian, which can be seen as a consequence of the reduced symmetry. In contrast to the uniaxial case, the second homotopy group is

$$\pi_2(SU(2)/\mathbb{Q}) = 0, \tag{1.31}$$

which means the biaxial nematic system does not admit point defects.

From a mathematical standpoint, the homotopy groups considered so far must be made up of restricted maps fixed at a basepoint, x_0. If we allow the base point to shift we must adjust the elements of the group accordingly and this procedure turns out to be an inner automorphism that sends an element $\alpha \in \pi_1(X)$ to a conjugate $\beta\alpha\beta^{-1}$ for $\beta \in \pi_1(X)$. If the fundamental group is abelian, this shift is clearly trivial, so the base point is irrelevant and the *free* homotopy group is often implied. In a non-Abelian setting, however, this conjugation forces one to classify based on its conjugacy classes of π_1 rather than the group elements of π_1. The quaternion group of 8 elements, for example, partitions into 5 conjugacy classes:

$$\mathbb{Q} = \{1\} \cup \{-1\} \cup \{i, -i\} \cup \{j, -j\} \cup \{k, -k\}, \tag{1.32}$$

each of which represents a class of line defects. Physically, this non-commutativity manifests itself in path dependence when combining two defect lines, meaning that the result of fusing two defect lines may differ depending on the path taken around other disclinations in the medium. This can be seen algebraically in the quaternions as $i(ij) = -j$ but $(ij)i = -iij = j$. In topological quantum computing, this is typically known as having multiple fusion channels and is a result of braiding two 2D anyons in $(2+1)$ dimensions [31]. Unlike the anyons, however, we have 1D strands that can be braided in real space. Toulouse, along with mathematician Valentin Poenaru, rigorously described the effects of

(*a*)   Abelian

(*b*)   non-Abelian
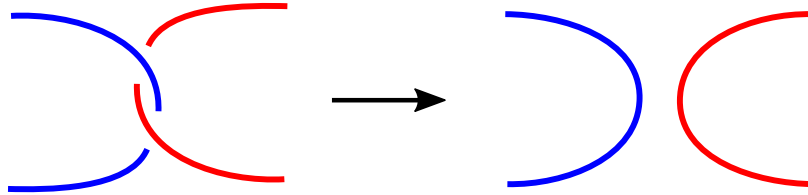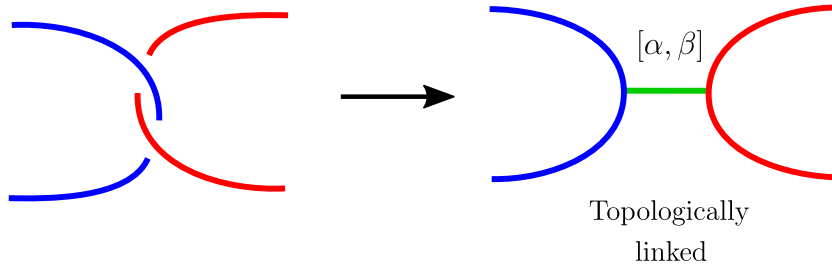

Topologically
linked

Figure 1.8: (a) Two linked Abelian defect lines may disentangle themselves while
(b) non-Abelian defect lines necessarily produce tethering defect line with topological
charge given by the commutator of the two defects, $[\alpha, \beta] = \alpha\beta\alpha^{-1}\beta^{-1}$, if they cross.

this path dependence in the process of crossing two defect lines. One can show through
various deformations of a measuring loop that in the non-Abelian case, the braiding re-
sults in a topologically stable structure and they may only disentangle by generating a
tether with conjugacy class given by the commutator, $[\alpha, \beta] = \alpha\beta\alpha^{-1}\beta^{-1}$, of the two
entangled defects [32] (Fig. 1.8(b)). In contrast, Abelian defect lines, such as those in
3D uniaxials, are topologically allowed to freely cross through each other without any
obstruction as their commutator are always trivial (Fig. 1.8(a)).

Nearly 50 years after the theoretical formulation of biaxial nematics, there is still
no concrete experimental evidence for a pure biaxial system. There has been, how-
ever, progress in obtaining systems that, although not purely biaxial, mimic or exhibit
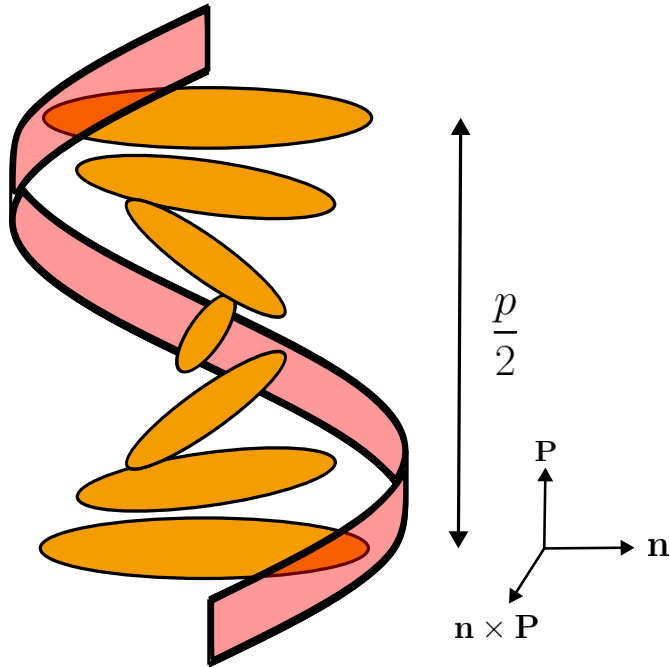
Figure 1.9: Chiral liquid crystal ground state structure with right handed twist, $q_0 < 0$. The twisted structure defines a pitch direction, $\mathbf{P}$, as well as a length scale known as the pitch, p, defined to be the length of a 2π rotation.

a relatively high degree of biaxiality and which provide an approximation and a testing ground for the topological entanglement of biaxial defects. One such system is chiral (or cholesteric) liquid crystals (CLCs). These are liquid crystals in which the ground state energetically favors a twist q_0, which breaks chiral symmetry of the nematic thus defining a handedness (see Fig. 1.9) through some chiral dopant in the medium. Despite the fact that the system is locally uniaxial at the molecular scale, the twist sets a pitch scale $p = 2\pi/q_0$, which, defines a direction along which the molecules rotate, $\mathbf{P}$. This, along with the nematic director and the cross product $\mathbf{n} \times \mathbf{P}$, define an orthonormal triad that breaks the uniaxial symmetry at the pitch scale. CLCs, therefore, have ground states that are topologically identical to those of biaxials.

Chapter 3 of this thesis begins with a more detailed introduction to the biaxial system as well as a more in-depth presentation of the entangled non-Abelian structures. I will

then introduce a classification system for complex braided structures that takes advantage of the non-Abelian properties of the system. We will conclude with simple examples of structures that are experimentally realizable in chiral systems as part of an experimental collaboration. This is based upon work currently in preparation [33].

Chapter 2

Switching Dynamics of Thermalized Graphene Cantilevers

The rise in popularity of graphene-based materials in the hard condensed matter field reinstated the interest in the study of thermalized membranes. Graphene as a membrane possesses fantastic elastic properties that provide a testing ground for the predictions made decades ago about thin solid materials subject to thermal fluctuations. One such important prediction is the renormalization of the elastic constants. In Chapter 1, we discussed that thermal fluctuations stiffen the bending rigidity, κ, while the stretch modes controlled by the Young's modulus, Y, are softened. Experimental efforts to verify these effects in thermalized graphene have yielded positive results wherein κ was found to be significantly enhanced by $\kappa_R/\kappa_0 \sim 4000$ in graphene cantilevers [34] while the in-plane stiffness decreases as $Y_R/Y_0 \sim 1/20 - 1/3$ at room temperature [35].

2.1   The tilted phase

The thermalization of graphene membranes modifies not only the aforementioned elastic properties, but also the geometry of the sheet itself. At zero temperature, a rectangular sheet has area $W_0 \times L_0$ (Fig. 2.1(a)). Once a sheet is thermalized, thermal corrugations store some of the area in the form of out-of-plane fluctuations leading to overall thermal shrinking and smaller average projected area, $W_{th} \times L_{th}$, at thermal equilibrium (see Fig. 2.1(b)). Here the values have the property $L_{th} < L_0$ and $W_{th} < W_0$.
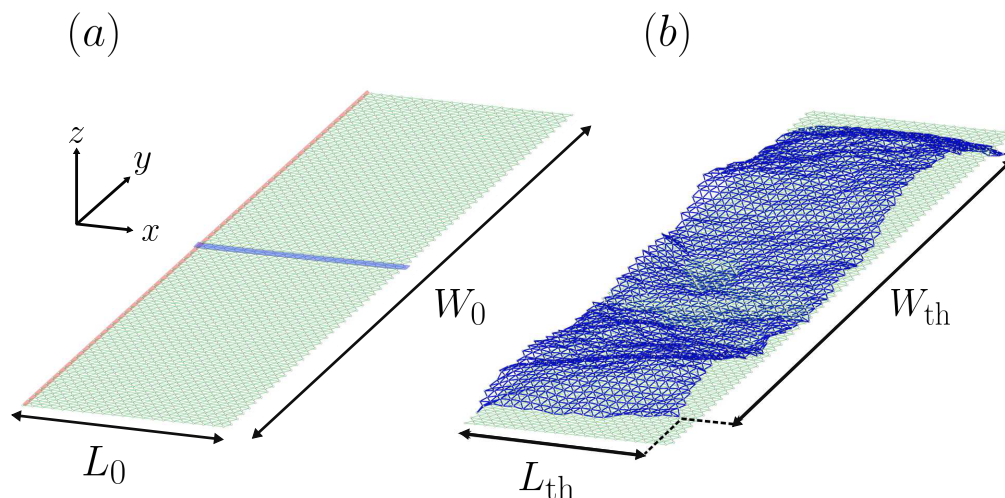

Figure 2.1: (a) $T = 0$ triangulated sheet with length L_0, width, W_0 and aspect ratio $\alpha = W_0/L_0 = 5$. Highlighted in red (along $(x, y) = (0, y)$) are the fixed vertices corresponding to the clamp at $x = 0$. Highlighted in blue and outlined in black (along $(x, y) = (x, 0)$) are the vertices that constitute the middle slice of the sheet (b) Same sheet, shown in blue (top), at finite temperature with free boundary conditions: the finite temperature dimensions L_{th}, W_{th} are smaller than their zero-temperature counterparts.

We now proceed to exploit this thermal shrinkage in order to study a symmetry-broken phase, the tilted phase. Consider an elastic sheet with zero-temperature width W_0, length L_0 so that the aspect ratio of the sheet is $\alpha = W_0/L_0$. We clamp along one of the two extended edges, say at $x = 0$ (pink box in Fig. 2.1(a)) so that the clamped width

is W_{clamp}. Unlike zero temperature elasticity, deformations upon this initial configuration will not be in reference to the sheet of area $W_0 \times L_0$ but rather the thermalized sheet with area $W_{th} \times L_{th}$, which we will refer to as the thermalized reference state.

In the cantilever configuration described above, if $T > 0$, the clamped edge will attempt to adjust back to the reference thermal reference state length, $W_{th} < W_0$. This will in turn generate a clamping strain

$$\epsilon_{clamp} = \frac{W_{clamp} - W_{th}}{W_{th}} \tag{2.1}$$

which, in the case where $W_{clamp} = W_0$, is simply the thermal shrinkage. The clamping then generates a source of stress localized around the clamped edge, generating some stress in the perpendicular direction. As we mentioned in the introduction, thin membranes are easier to bend than to stretch, thus the most energetically favored way to alleviate this stress is through bending. This means that the sheet can take on curved configurations as seen in classical buckling instabilities such as Euler buckling [5] which has a thermalized analogue [36]. This curved configuration creates a buckled phase known as the tilted phase, where the free end has a non-zero height in some spontaneously chosen direction (see Fig. 2.2). The existence of this tilted phase was first explored both theoretically and numerically in [37] where they found the phase requires aspect ratios $\alpha > 1$ as well are some low and high-temperature cutoffs.

2.2   1D Strip model

The complex nature of the elastic free energy of this system makes it incredibly difficult to analyze it in the context of tilt. However, we can make use of the mirror symmetry along the y-axis in order to make further reductions. Consider taking a slice
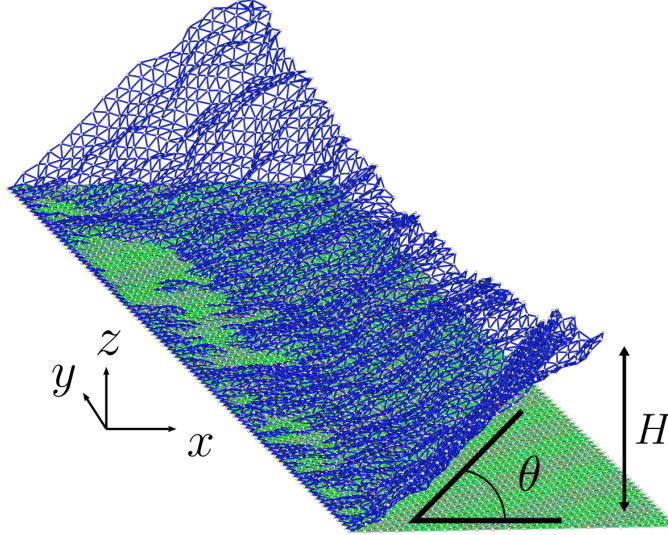
Figure 2.2: Thermalized sheet with aspect ratio $\alpha = 8$ in the tilted state with height, H, and tilt angle, θ.

of the cantilever setup along the $y = 0$ axis (blue box in Fig. 2.1(a)). We refer to this as the middle slice. We can then reduce our free energy into a model for this middle slice.

We start with the classical elastic model given by Eq. 1.4 and average along the y-direction, which yields a factor of W_{clamp} and gives

$$\mathcal{F}_{1D} = \int_0^L dx \left[\frac{\tilde{\kappa}}{2} \left(\frac{\mathrm{d}^2 h}{\mathrm{d}x^2} \right)^2 + \frac{\tilde{Y}}{2} \left(\frac{\mathrm{d}u_x}{\mathrm{d}x} + \frac{1}{2} \left(\frac{\mathrm{d}h}{\mathrm{d}x} \right)^2 \right) \right] \tag{2.2}$$

where the tilde indicates a factor of W, e.g. $\tilde{\kappa} = W\kappa$. The Fourier expansions of the in-plane and out-of-plane modes can then be written as

$$\frac{\partial u_x}{\partial x} = u_0 + \sum_{q \neq 0} iqu(q)e^{iqx} \tag{2.3}$$

$$A(x) \equiv \frac{1}{2} \left(\frac{\partial f}{\partial x} \right)^2 = A_0 + \sum_{q \neq 0} A(q)e^{iqx} \tag{2.4}$$

where we have separated the zero modes, u_0 and A_0. Upon substitution of the Fourier

expansions, the stretching part of the energy becomes

$$\mathcal{F}_{\text{stretch}} = \frac{\tilde{Y}L}{2}\left[(u_0 + A_0)^2 + \sum_{q \neq 0}|iqu(q) + A(q)|^2\right] \tag{2.5}$$

If we fix the height profile, $h(q)$, the stretching energy will be minimized when $u(q) = -iA(q)/q$ and the second term above vanishes. We can now apply the cantilever boundary conditions:

$$u_x(x = 0) = 0 \tag{2.6}$$

$$u_x(x = L) = -\Delta \tag{2.7}$$

where Δ is some displacement. Doing so, we find the following expressions for the in-plane zero mode:

$$u_0 = \frac{1}{L}\int_0^L dx \, \frac{\mathrm{d}u_x}{\mathrm{d}x} = -\frac{\Delta}{L} \tag{2.8}$$

and the out-of-plane mode is

$$A_0 = \frac{1}{2L}\int_0^L dx \left(\frac{\mathrm{d}h}{\mathrm{d}x}\right)^2. \tag{2.9}$$

Putting everything together, we find a model for the 1D slice of the tilted membrane

$$\mathcal{F}_{1D} = \frac{\tilde{\kappa}}{2}\int_0^L dx \left(\frac{\mathrm{d}^2 h}{\mathrm{d}x^2}\right)^2 - \frac{\tilde{Y}\Delta}{2L}\int_0^L dx \left(\frac{\mathrm{d}h}{\mathrm{d}x}\right)^2 + \frac{\tilde{Y}}{8L}\int_0^L\int_0^L dx \, dx' \left(\frac{\mathrm{d}h}{\mathrm{d}x}\right)^2\left(\frac{\mathrm{d}h}{\mathrm{d}x'}\right)^2. \tag{2.10}$$

The first term is the usual bending term that penalizes curvature of h. The second term is a force term arising from the free boundary condition and acts as the "mass" term of the theory. Note that we don't have a quadratic term such as this one in the free

26

theory (Eqn. 1.4) as we did not include external forces. The third term is our non-linear, *non-local* stretching term. Note that the energy landscape is symmetric about the flat state (Fig. 2.3). We can generalize this by adding a symmetry-breaking, transverse field (such as a gravitational or an electric field) that couples linearly to the height $h(x)$ in Eq. 2.10. This will create an asymmetric potential well, resulting in two distinct minima.

Near the tilt transition, we choose as an ansatz the first buckling mode in the $T = 0$ cantilever problem, $h(x) = H \left[1 - \cos \left(\frac{\pi x}{2L} \right) \right]$, where H is the height of the free end [38]. Upon inserting this ansatz into Eq. 2.10, we obtain a mean field energy

$$E_{MFT}(H) = a \left(\Delta_c - \Delta \right) H^2 + bH^4 \tag{2.11}$$

where $a = \pi^2 W Y_R / 16 L^2$ and $b = a \pi^2 / 32 L$. This yields a critical compression

$$\Delta_c = \frac{\pi^2}{4L} \frac{\tilde{\kappa}_R}{\tilde{Y}_R}. \tag{2.12}$$

In this form, it is easy to see a clear separation between the flat phase ($\Delta < \Delta_c$) and the tilted phase ($\Delta > \Delta_c$) as shown in Fig. 2.3.

In the tilted phase there are two minima, $E_\pm$, separated by an energy barrier,

$$\Delta E_b = |E_{flat} - E_\pm| \tag{2.13}$$

where $E_{flat} = E(H = 0) = 0$ is the energy of the unstable flat state and $E_\pm = E(H_\pm)$ is the energy of a tilted state (see Fig. 2.3. We can calculate the location of the minima $H_\pm$ to find

$$H_\pm = \pm \frac{4\sqrt{L}}{\pi} \sqrt{\Delta - \Delta_c} \tag{2.14}$$
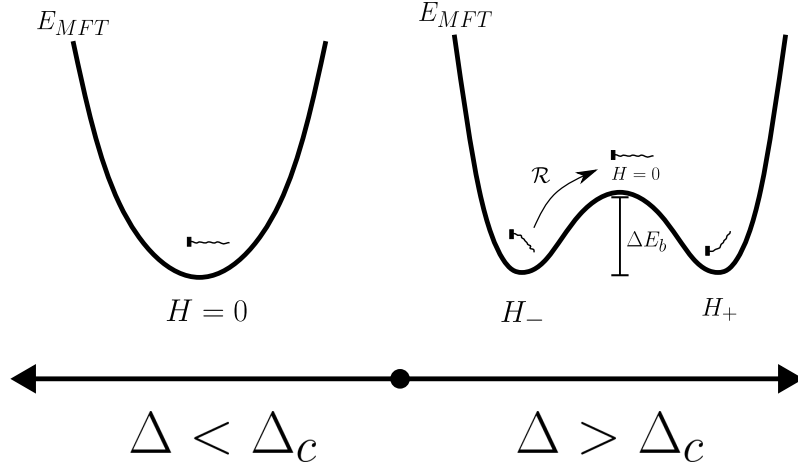
Figure 2.3: Diagramatic depiction of the effective mean-field energy $E_{MFT}(H)$ for $\Delta < \Delta_c$ (left) and $\Delta > \Delta_c$ (right). The finite energy barrier, E_b, separating the two tilted states allows for transitions from one state to the other with probability $\mathcal{R}$.

which makes the energy barrier

$$\Delta E_b = \frac{\pi^4 \bar{\Delta}^2 W}{32 L^3} \frac{\kappa^2}{Y},\tag{2.15}$$

where we define a relative compression

$$\bar{\Delta} = \frac{\Delta - \Delta_c}{\Delta_c}\tag{2.16}$$

which is positive in the tilted phase. This relative compression can be estimated by obtaining an expression for the compression of the free end due to a clamping stress. This has a form [37]

$$\Delta \approx \frac{L_0 \alpha \epsilon}{2 \sinh^2\left(\frac{\pi\alpha}{4}\right)} \left[\frac{\pi\alpha}{4} \cosh\left(\frac{\pi\alpha}{4}\right)(1 + \nu_R) - \sinh\left(\frac{\pi\alpha}{4}\right)(1 - \nu_R)\right],\tag{2.17}$$

where ν_R is the renormalized Poisson ratio and ϵ is none other than the thermal shrinking strain at the clamp, which is given by [39]

$$\epsilon \equiv \left\langle \frac{W_{clamp} - W_{th}}{W_{th}} \right\rangle \approx \frac{1}{8\pi\tilde{\kappa}_0} \left[\frac{1}{\eta} - \frac{1}{\eta} \left(\frac{L_0}{\ell_{th}} \right)^{-\eta} + \ln\left(\frac{\ell_{th}}{a} \right) \right]. \tag{2.18}$$

Once the system is in one of the tilted states, as in any such two-state systems [40], there is a non-zero probability of transitioning from one state to the other with maximal transition probability at some resonant value of an external parameter such as temperature or an external driving frequency [41]. One might expect the transition rate at finite temperatures to be controlled primarily by thermal fluctuations over the barrier. However, we show that the dimensionless and purely geometrical aspect ratio is a key determiner.

2.3 Transition Rates

Consider a system with an energy landscape given by Eq. 2.11 and assume that $\Delta > \Delta_c$ so that we are in the tilted phase. We can assign each of the extrema of E_{MFT} a characteristic frequency, $\omega_\pm$ and ω_B, which are obtained from the second-order expansion of $E(H)$ at one of the tilted states ($H = H_\pm$) and the saddle point ($H = 0$), respectively. We can estimate the rate $\mathcal{R}$ of transitioning from one of the tilted wells to the other using Kramers' theory [42, 43], which predicts

$$\mathcal{R} \approx R_0 e^{-\Delta E_b / k_B T} \tag{2.19}$$

where the amplitude R_0 will take a form that depends on the friction of the system, $\beta = \gamma/m$, which is the ratio of the friction to the mass m of the sheet and has the units

of frequency. The system can be underdamped ($\beta \ll \omega_B$) or overdamped ($\beta \gg \omega_B$). Given the energy barrier Eq. 2.15, this yields a transition rate

$$\mathcal{R} \approx R_0 \exp\left[-\frac{\pi^4 \bar{\Delta}^2 W}{32 L^3} \frac{\kappa^2}{k_B T Y}\right].$$ (2.20)

Here, we do not include an inversion symmetry-breaking field and so we assume that the transition rates are equal regardless of direction. That is, $\mathcal{R}_{+\rightarrow-} = \mathcal{R}_{-\rightarrow+} = \mathcal{R}$.

As previously mentioned, the prefactor R_0 depends on the magnitude of the friction, β. It takes the form [42]

$$R_0 \approx \begin{cases} \frac{m\beta \Delta E_b}{\pi k_B T}, & \beta \ll \omega_B \\[2mm] \frac{\omega_\pm \omega_B}{2\pi\beta}, & \beta \gg \omega_B, \end{cases}$$ (2.21)

where we see a turnover from a linear to an inversely proportional dependence in β.

We are interested in system sizes sufficiently large that thermal fluctuations are important. This means the length of the sheet satisfies $L \gg \ell_{th}$, where ℓ_{th} is the characteristic thermal length scale beyond which the elastic constants become scale-dependent as given in Eq. 1.13. As introduced in the previous chapter, the elastic moduli κ and Y are renormalized by thermal fluctuations, rendering them length-scale dependent [44]. They must then be replaced by their respective renormalized values given by the scalings

$$\kappa_R \sim \kappa_0 \left(\frac{L}{\ell_{th}}\right)^\eta$$ (2.22)

$$Y_R \sim Y_0 \left(\frac{L}{\ell_{th}}\right)^{-\eta_u},$$ (2.23)

which make the boltzmann factor in Eq. 2.20

$$\frac{\pi^4 \bar{\Delta}^2 W}{32 L^3} \frac{\kappa^2}{k_B T Y} \xrightarrow{L \gg \ell_{th}} \frac{\pi^4 \bar{\Delta}^2 W}{32 L^3} \frac{\kappa_R^2}{k_B T Y_R} = \frac{\pi^4 \bar{\Delta}^2 W}{32 L^3} \frac{\kappa_0^2}{k_B T Y_0} \left(\frac{L}{\ell_{th}} \right)^{2\eta + \eta_u} \tag{2.24}$$

$$= \frac{\pi^4 \bar{\Delta}^2 W}{32 L^3} \frac{\kappa_0^2}{k_B T Y_0} \left(\frac{L}{\ell_{th}} \right)^2 \tag{2.25}$$

$$= \frac{\pi^4 \bar{\Delta}^2}{32} \frac{\kappa_0^2}{k_B T Y_0 \ell_{th}^2} \frac{W}{L} \tag{2.26}$$

$$= \frac{3\pi \bar{\Delta}^2}{512} \alpha \tag{2.27}$$

where the second equality used the Ward identity $\eta_u = 2 - 2\eta$ and the last equality uses the definition of ℓ_{tg} (Eq. 1.13). For a fixed relative compression, $\bar{\Delta}$, corresponding to a fixed value of the tilt order parameter or energy barrier, the transition rate is controlled by the aspect ratio α in the exponential, which therefore plays the role of a Boltzmann factor. Effectively geometry is replacing temperature as the main driver for transitions. Temperature enters implicitly in tuning to a fixed relative compression as well as in the amplitude.

In the thermalized limit, $L \gg \ell_{th}$, we obtain the following prefactors

$$R_0 \approx \begin{cases} \frac{3 m \beta \bar{\Delta}^2}{512} \alpha, & \beta \ll \omega_B \\ \frac{\pi^3 \bar{\Delta} \kappa_0}{32\sqrt{2} m \beta L^2} \left(\frac{L}{\ell_{th}} \right)^\eta \alpha, & \beta \gg \omega_B, \end{cases} \tag{2.28}$$

in which we note that the temperature dependence in the overdamped case comes from the renormalization of the bending rigidity as given by the scaling of κ_R. In the underdamped case, we see the same cancellation of temperature that occurs in the Arrhenius factor in Eq. 2.27 and we have explicit independence of temperature at constant compression $\bar{\Delta}$. Note that for both cases, we expect the Arrhenius factor to provide the dominant behavior for significant compression $\bar{\Delta}$.

To summarize, focusing on the underdamped case, the transition rate is given by

$$\mathcal{R}(L \gg \ell_{th}) \approx \frac{\pi^3 \bar{\Delta} \kappa_0}{32\sqrt{2} m \beta L^2} \left(\frac{L}{\ell_{th}} \right)^{\eta} \alpha \exp\left(-\frac{3\pi \bar{\Delta}^2}{512} \alpha \right). \tag{2.29}$$
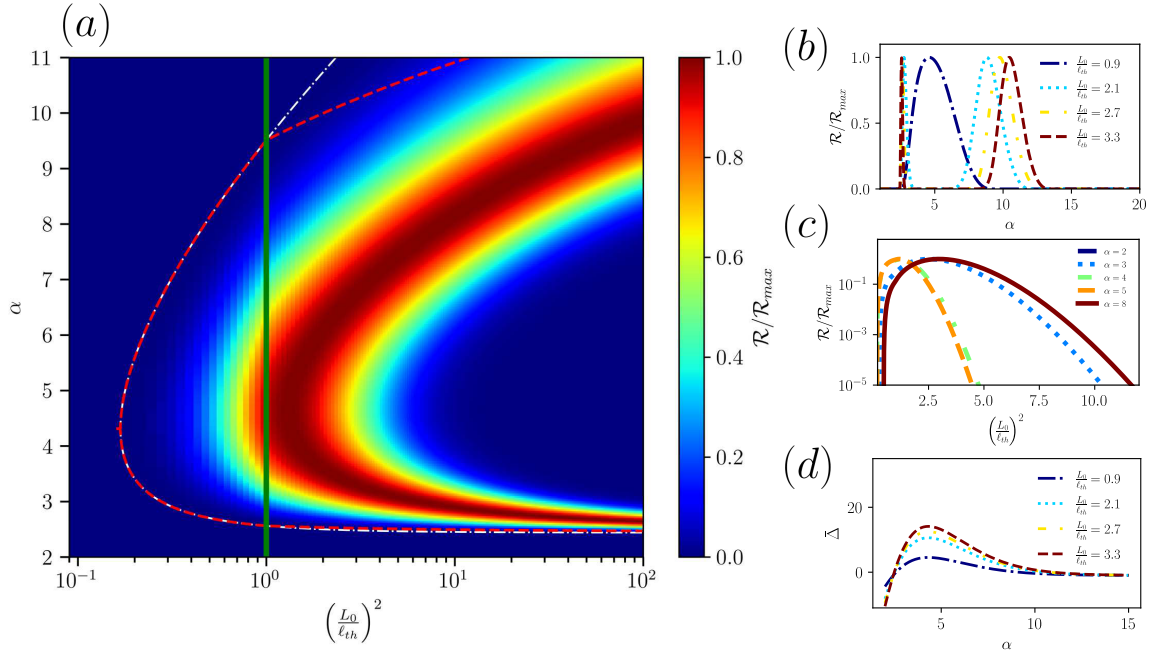

Figure 2.4: (a) Density plot of the theoretical transition rate as a function of aspect ratio and temperature ($\propto (L/\ell_{th})^2$) with color, as indicated by the color bar (right), representing the estimated transition rate normalized by the maximum value within the range. Mean field theory prediction of the tilted phase boundary is shown as a red dashed line, where we differentiate between bare and renormalized elastic constants beyond the $L_0/\ell_{th} = 1$ line (green solid line). The white dash-dotted line shows the phase boundary were the elastic constants to have no scale dependence beyond the thermal length scale. (b-c) 2D slices of the theoretical transition rate as a function of aspect ratio (b) and temperature (c). (d) Plot of the reduced compression, $\bar{\Delta}$, as a function of the aspect ratio, α, as predicted by Eqn. 2.17. Note that the regions of positive $\bar{\Delta}$ coincides with regions of $\mathcal{R} > 0$.

Having all the pieces, we can now visualize the different regions of tilt transition behavior by plotting the transition rate as a function of aspect ratio, α, and temperature in the form of $(L/\ell_{th})^2 \sim k_B T$. Fig. 2.4 shows a density plot of the underdamped transition

rate as a function of temperature and aspect ratio, normalized by the maximum rate in the displayed region as predicted by Eq. 2.20. We include a phase boundary provided by setting the predicted compression, Δ in Eq. 2.17, equal to the critical compression, Δ_c, computed from the 1D mean field theory (Eq. 2.12). In other words, we plot the line

$$\Delta = \Delta_c \tag{2.30}$$

accounting for renormalization of the elastic constants for $L_0 > \ell_{th}$. To the left of this boundary, the system is in the flat phase ($\Delta < \Delta_c$) and the transition rate vanishes. Note the high transition rate localized near the phase boundary. As the temperature is increased deep in the tilted state the transition rate reaches a dynamically stable "basin" with long dwell times, as indicated by the dark blue region. The α-scaling form of Eq. 2.29 does not capture the full behavior near the upper branch of the phase boundary as it neglects the higher order contributions coming from $\bar{\Delta}$. Indeed our mean field theory will break down in the limit of large α where the length of the membrane becomes negligible compared to the width and the 1D midline model is no longer applicable.

Temperature is a more traditional parameter to tune the dynamics of these types of oscillator systems as higher temperatures often decrease the energy barrier and allows for higher transition probabilities. In this system, however, we see that thermalization gives access to another possible parameter that controls transitions namely, α, and with the addition of thermal factors in the prefactor, we see that high temperature instead stabilizes the system in one of the stable tilted states with close to zero transition probability. This can be thought of as temperature decreasing the rest area of the reference state, thereby effectively increasing the clamping strain. Based on the predicted form of the transition rate, we can expect $\mathcal{R} \approx 0$ for large temperatures, where we expect the sheet to be in a fully tilted state. This means that in an experimental setting, low

33

temperatures are needed to access the dynamic tilted state, where $\mathcal{R} \neq 0$, and in order to retain a specific constant transition rate, the temperature must remain constant. One can circumvent this by considering the aspect ratio of the sample as a tunable parameter. We can prescribe appropriate geometrical dimensions corresponding to an aspect ratio that leads to the desired transition rate at some constant temperature. Thus, the aspect ratio gives access to a larger sample parameter space in the production of nano-mechanical actuators and may prove to be are more desirable parameter to tune in the manufacturing of such devices.

2.4   Simulating tilt transition rates

In order to verify the validity of our findings, we turn to simulating sheets in the dynamic tilted state. To do so, we turn to a discrete or coarse-grained version of our elastic free energy 1.4. It can be verified that on a triangularized 2-dimensional sheet with lattice constant a, the elastic free energy takes the form

$$E = \hat{\kappa} \sum_{\langle I,J \rangle} \left(1 - \hat{\mathbf{n}}_I \cdot \hat{\mathbf{n}}_J\right) + \frac{k_{\text{stretch}}}{2} \sum_{\langle i,j \rangle} (r_{ij} - a)^2, \qquad (2.31)$$

where the continuum bare bending rigidity κ_0 and Young's modulus Y_0 are related to the discrete bending rigidity $\hat{\kappa}$ and the harmonic spring constant k_{stretch} by $\kappa_0 = \sqrt{3}\hat{\kappa}/2$ and $Y_0 = 2k_{\text{stretch}}/\sqrt{3}$. The first term represents the discretized bending energy resulting from normals on adjacent plaquettes (triangular faces) that are not perfectly aligned and the second term is a harmonic stretching energy between adjacent nodes. The first sum is performed over all nearest neighbor plaquettes, $\langle I, J \rangle$, while the second sum is over all nearest-neighbor vertices $\langle i, j \rangle$ (see Fig. 2.5).

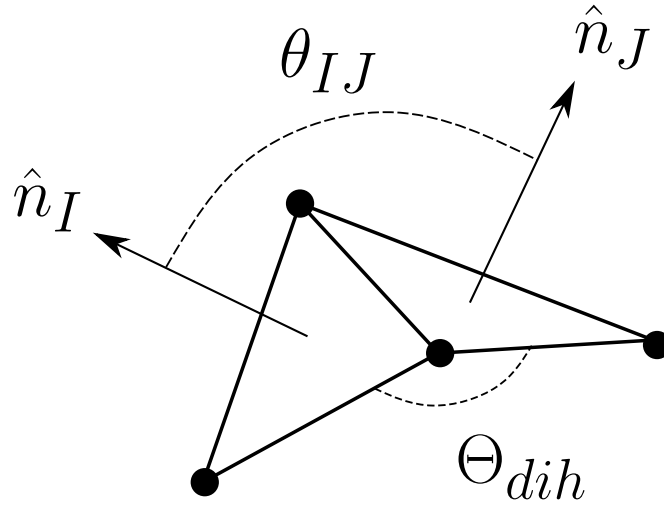The coarse-grained energy (2.31) can be simulated using the HOOMD-blue python

Figure 2.5: Two neighboring plaquettes in the course-grained system forming a dihe-dral. Simple geometry can be used to replace the angle between the two plaquette normals, θ_{IJ}, by the dihedral angle, Θ_{dih}: $\theta_{IJ} = \pi - \Theta_{dih}$. Using this dihedral angle proves to be more convenient when working with MD packages, such as HOOMD-blue, that have energies associated to dihedral angles readily available.

package for molecular dynamics (MD) [45] for a triangular lattice with $a = 1$. The stretching term is treated as a harmonic potential between two nodes and the bending energy has a discrete representation in terms of the dihedral angle formed by neighboring triangular plaquettes, $\Theta_{dih} = \pi - \theta_{IJ}$, where θ_{IJ} is the angle between the two plaquette normals (see Fig.2.5). Dihedral angles can be readily obtained using HOOMD-blue. A triangular lattice with fixed dimensions is initialized with two rows along the y-axis held fixed to simulate the clamp at one edge. The width of the clamp may be varied by adjusting the x-positions of the clamped nodes with some prescribed displacement. The system is then integrated in an NVT ensemble for a total of $N = 2 \times 10^7 - 10^8$ time steps with step size $dt = 0.005$ time steps and with energy scale set by $k_B T$. The first half of these time steps is discarded to ensure thermalization. We extract the time series of the out-of-plane height of a single node at the middle of the free edge opposite the clamped edge: $(x, y) = (L, 0)$. We generate multiple independent runs ($n = $ 3-5) for each set

35

of initial parameters to generate error statistics which are computed using the jackknife procedure [46].

To test the predicted transition rate, we simulate multiple systems with elastic properties parallel to that of real crystalline systems ($Y_0 = 20\,\text{eV}\,\text{Å}^{-2}$, $\kappa = 1.2\,\text{eV}$) at fixed length $L = 20a$ (≈ 50 Å for graphene) and for a range of temperatures $k_B T/\kappa \approx 0.01 - 2$ (or $L/\ell_{th} \approx 0.8 - 5$) and aspect ratios $\alpha = 2 - 9$ [1]. Once we ensure thermalization we can proceed to analyze the dynamics of the tagged node. We estimate the thermalized length of the system, L_{th}, as the length of the free membrane at a given temperature, projected onto the $z = 0$ plane, shown in Fig. 2.1(b). We then define the compressed length, L_c, as the projected length in the clamped configuration, illustrated in Fig. 2.1(d).

The up-down transition rate is calculated by tabulating the average time spent in a tilted state, the dwell time τ_{dwell}. Residence in the tilted state is determined conditionally with a threshold height $h_{th} = 0.1 \times L_0$: viz. $|h(t_n)| > h_{th}$ is assigned to the tilted state. The transition probability is then $\mathcal{R} \sim 1/\tau_{dwell}$.

A more elaborate method of determining the dwell time is by computing the autocorrelation function of the time series post-thermalization. The normalized autocorrelation function, $\rho(\tau) \equiv C_t(\tau)/C_t(0)$, will decay exponentially with a time constant, τ_{ac}. This time constant corresponds to the shortest time scale available to the system, which in this case is the time spent in a given tilted state: $\tau_{dwell} \approx \tau_{ac}$.

One can think of the dynamics of the sheet in the flat state, specifically the average height of the tagged node, as a Brownian particle trapped in a harmonic well. In the pre-buckling regime, the Langevin equation for the position $z(t)$ of a particle of mass m is

$$\ddot{z}(t) = -\frac{\gamma}{m}\dot{z}(t) - \omega_0^2 z(t) + \frac{1}{m}\xi(t) \tag{2.32}$$

---

[1]Note that at fixed L, α is controlled by the clamped width W_{clamp} which is equal to W_0 unless otherwise stated

where $\omega_0 = k/m$ and $\xi(t)$ is Gaussian noise with

$$\langle \xi(t) \rangle = 0 \tag{2.33}$$

$$\langle \xi(t)\xi(t') \rangle = 2m\beta k_B T \delta(t - t'). \tag{2.34}$$

Fourier transforming $\left(\frac{d^n}{dt^n} z(t) \to (-i\omega)^n z(\omega)\right)$ gives

$$z(\omega) = \frac{1}{m} \frac{\xi(\omega)}{\omega_0^2 - \omega^2 + i\frac{\gamma}{m}\omega}. \tag{2.35}$$

We can now compute the correlation function via the inverse Fourier transform of the squared average in frequency space,

$$C_t(t') = \langle z(t)z(t') \rangle = \int_{-\infty}^{\infty} \frac{d\omega}{2\pi} \langle |z(\omega)|^2 \rangle e^{-i\omega t} \tag{2.36}$$

$$= \frac{\gamma k_B T}{\pi m^2} \int_{-\infty}^{\infty} d\omega \frac{e^{-i\omega t}}{(\omega^2 - \omega_0^2)^2 + \frac{\gamma}{m}\omega^2}. \tag{2.37}$$

The integral in Eq. (2.37) via complex methods with a semicircular contour

$$C_t(\tau) = \frac{k_B T}{m\omega_0^2} e^{-\frac{\gamma\tau}{2m}} \left[\cos\omega_1\tau + \frac{\gamma}{2m\omega_1} \sin\omega_1\tau \right]. \tag{2.38}$$

The normalized autocorrelation function is then

$$\rho(\tau) = \frac{C_t(\tau)}{C_t(0)} = e^{-\frac{\gamma\tau}{2m}} \left[\cos\omega_1\tau + \frac{\gamma}{2m\omega_1} \sin\omega_1\tau \right]. \tag{2.39}$$

For sufficiently long times ($\tau \gg t_{dwell}$) and for systems with low tilt transitions the autocorrelation will decay as [46]

$$\rho(\tau) \sim \exp(-\tau/\tau_{ac}). \tag{2.40}$$

Comparing Eqs. (2.39) and (2.40) shows that

$$\tau_{ac} \approx \frac{2m}{\gamma} \tag{2.41}$$

We now provide a more detailed comparison between the simple average dwell time method and the autocorrelation method.
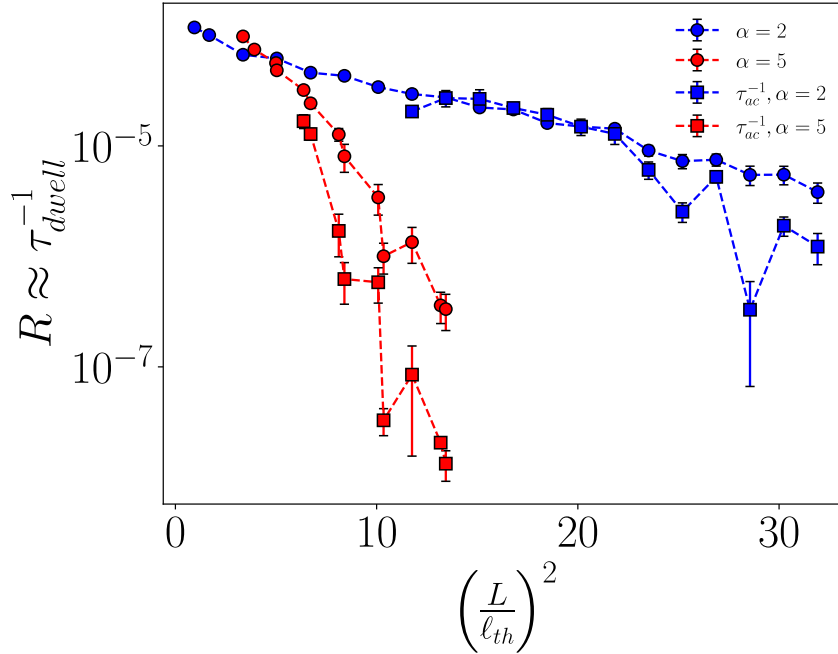

Figure 2.6: Transition rates for $\alpha = 2, 5$ as a function of temperature as measured by $\frac{L}{\ell_{th}}$. The points are computed from both dwell time averaging over multiple runs (circles) and from extracting the time constant τ_{ac} from a fit of the autocorrelation function, $\rho(\tau)$, to Eqs. (2.39, 2.40) for the regime with observable transitions and the fully tilted, low transition-rate regime, respectively (squares).

We compute the autocorrelation function of the height time series within a state and fit the curve to a function of the form of Eq. (2.39), extracting the time constant, τ. We can then compare to our previous results. Fig. 2.6 shows a semilog plot of $\tau_{\mathrm{dwell}}^{-1}$ as a function of $(L/\ell_{th})^2$, which is proportional to $k_B T$. The transition rate data $\tau_{\mathrm{dwell}}^{-1}$ are approximated using two methods: (i) height filtering and (ii) fitting to the autocorrelation function. Note that in the tilted regime, using autocorrelation to extract

the time constant may sample smaller timescales than the one of interest, namely the transition time, $\tau_{trans} < \tau_{dwell}$, which is the time it takes to jump from one state to the other. Fig. 2.6 shows autocorrelation estimates and we see that both methods provide roughly the same probability values and trends. There is, however, high variance in the autocorrelation estimate which can be attributed to uncertainty in the fit. The two methods agree qualitatively and for the purposes of studying the trends in the transition rate, we chose the former to save computational time.

To investigate the role of clamping we simulated several systems clamped at a range of strains close to $W_{clamp} = W_{th}$. Fig. 2.7 shows the time series of the height field $h = h(x = L, y = 0)$, for several clamping strains, $\epsilon \equiv (W_{clamp} - W_{th})/W_{th}$. Clamping sufficiently close to W_{th} does not induce tilt – the sheet fluctuates about a mean horizontal state (blue curve). Above a positive parameter-dependent threshold for ϵ we see the onset of tilt and the accompanying up-down inversions (red curve). The dwell time increases with ϵ (black curve).

It is instructive to measure the effective plane stress throughout the clamped sheet, as determined by displacements with respect to a fixed average thermalized free state. We take the particle positions of a sheet configuration at a fixed timestep and compute the displacements relative to the average thermalized, free reference state. Treating our lattice as a triangulated mesh and embedding the displacement field to the vertices of this mesh, we compute the linear 2D plane stress via finite element analysis. Appendix D.2 describes a related method that transforms the stresses back into the nodal basis.
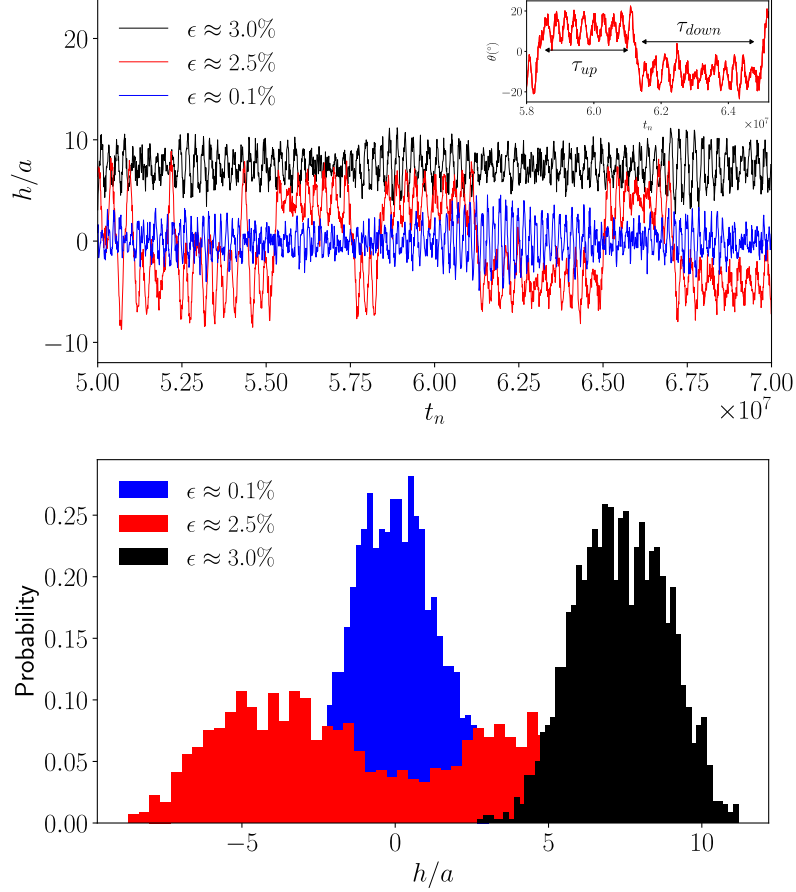
Figure 2.7: (left) Simulated time series of the height, $h(t_n)$, at timestep t_n of the middle slice at the free end of a sheet for $\alpha = 3$ and $\kappa/k_B T = 4$ ($L/\ell_{th} \approx 3$). Each curve represents a different value of the clamping strain, $\epsilon = (W_{clamp} - W_{th})/W_{th}$ (in %). When clamped at near zero strain, $\epsilon \approx 0.1$ (blue), we see oscillations centered around zero tilt, while at larger strains, $\epsilon \approx 2.5, 3\%$ (red, black resp.), we observe transitions between two nonzero tilt states and oscillations around a single nonzero tilt state, respectively. Note that the height can be easily translated into a tilt angle: see the red curve which oscillates between $\theta = \pm 20°$, as measured from the xy plane (see inset). Inset shows examples of the definition of the up and down dwell times, $\tau_{up/down}$. (right) Histogram of the probability distribution of heights for the time series time window above. Each distribution corresponds to a different clamping strain and shows the three possible cases: unimodal with zero mean (blue, back), bimodal (red, middle), and unimodal with nonzero mean (black, front). These correspond to the states where the sheet is flat, tilted with frequent transitions, and tilted with infrequent transitions, respectively.
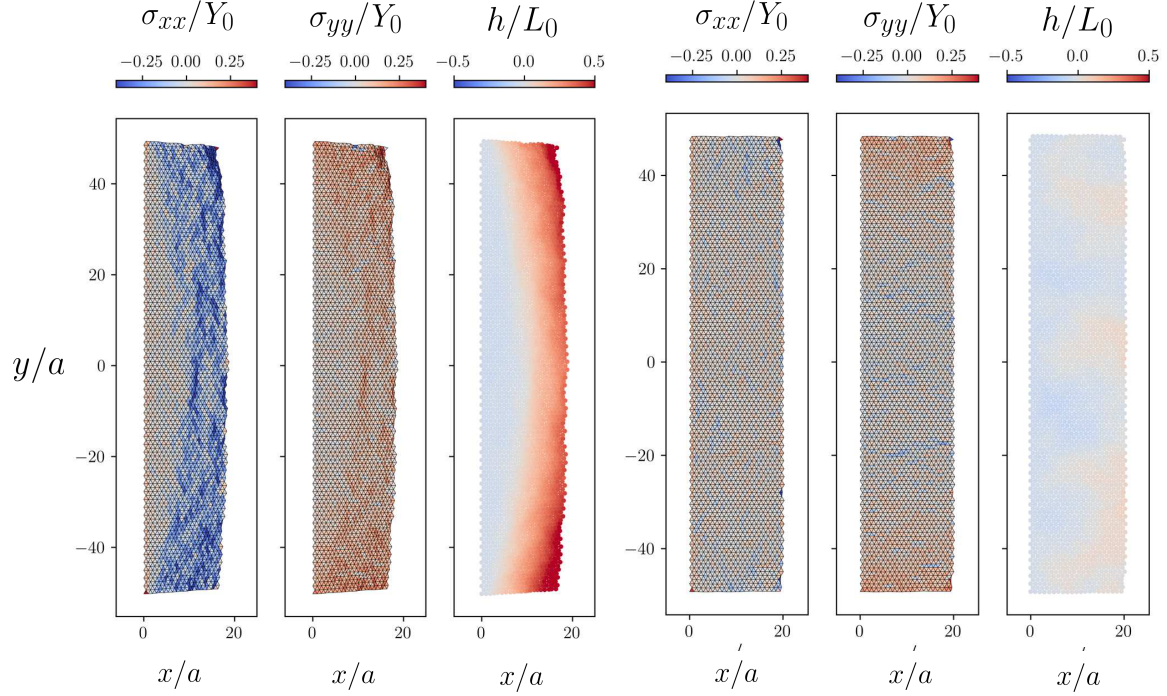
Figure 2.8: Diagonal components of the effective plane stress on the simulated sheet with $\alpha = 5$ and $L/\ell_{th} \approx 3$ along with a map of the height field for (left) $W_{clamp} = W_0 > W_{th}$ and (right) $W_{clamp} \approx W_{th}$. Sheet is shown as the projection of the deformed state onto the plane. The strain tensor is computed directly by differentiating the displacements from the free thermalized state.

For an effective extensive strain concentrated at the clamp ($W_{clamp} > W_{th}$), there are two competing effects: (1) the zero-temperature elastic response associated with a standard positive Poisson ratio, leading to compression along x and (2) the response associated with a negative Poisson ratio thermalized sheet associated with the known behavior at the thermal föppl-von Kármán fixed point, which creates an extensive response along x. The first effect should dominate in a zone of influence near the clamp as stretching suppresses thermal fluctuations. The second effect should dominate sufficiently far from the clamp where the sheet closely resembles a free fluctuating membrane. Fig. 2.8 shows a simulated map of both diagonal elements of the stress tensor at fixed

time steps obtained using the finite element method described above. We see that the σ_{xx} component confirms compressive stress for the tilted state ($W_{clamp} = W_0 > W_{th}$) and very little stress in the flat state ($W_{clamp} \approx W_{th}$), as expected. The σ_{yy} component shows the expected extension in the tilted phase. We note that the flat phase also exhibits some extension, which we attribute to the fact that we have a nearly but not quite zero strain at the clamp. We can also compare these stress maps to results found in previous work on tilted flaps [37].
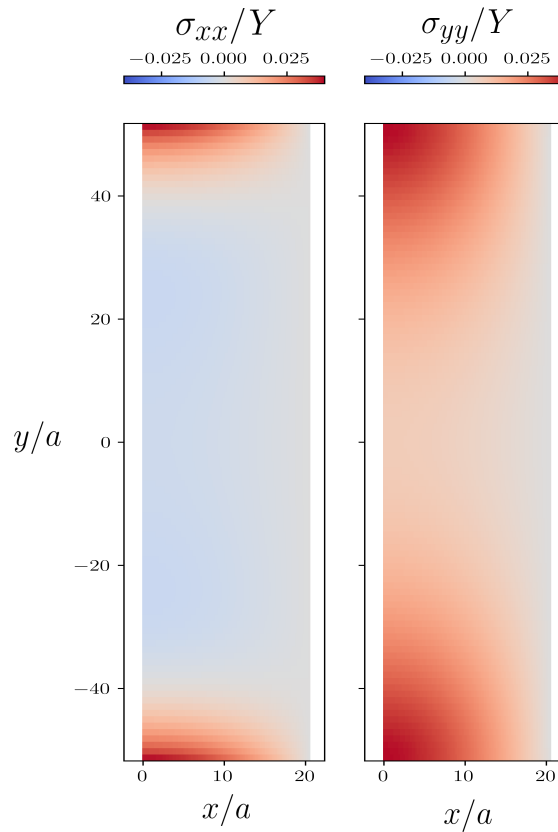

Figure 2.9: Theoretical approximation of the plane stress for an $\alpha = 5$ sheet with extension $\epsilon = 0.02$ at $T = 0$.

The estimated stress components are shown in Fig. 2.9 for a sheet of $\alpha = 5$ and $\epsilon = 0.02$. Comparing to the simulated stresses in Fig.2.8 we see that we have a similar accumulation of high extensive stress in the yy component for both theory and simulation,

indicating the extension of the clamp in reference to the free thermalized stress. We do see, however, a discrepancy in the location of this extension along the x-axis. Theory predicts this should be localized near the clamped side ($x = 0$). In the simulated stress we instead have high extension near the edge opposite to the clamp ($x = 20a$) with a region of low extension near the middle of the clamped edge. A possible explanation of this is the auxetic behavior of a free thermalized sheet. It is well known that free thermalized polymerized sheets are controlled by a föppl-von Kármán fixed point with a negative Poison ratio. Using a negative Poisson ratio for the stiffness matrix used to calculate our simulated stresses leads to extensive behavior not found in typical solids. If we assume clamping renders the Poisson ratio positive (at least in a neighborhood of the clamp which can be quite large) we can recover the compressive behavior in σ_{xx}.

One can confirm that the flat state reflects a zero-stress configuration from by the height-height correlation function, which is expected to scale as

$$\langle |h(q)|^2 \rangle \approx \frac{k_B T}{A(\kappa_R(q)q^4 + \sigma_{ij}q_i q_j)}. \tag{2.42}$$

where σ is the stress due to the clamp, A is the projected area of the sheet and κ_R scales as in Eq. 2.22. In the absence of stress, the bending term dominates and the correlation function will scale as $q^{-(4-\eta)}$. On the other hand, if there is a significant source of stress, we expect the quadratic term to dominate. Fig. 2.10 shows the mean-squared height fluctuations in momentum space for three classes of clamp width. For clamping near the thermalized width ($\varepsilon \approx 0$) the slope is approximately $-(4 - \eta)$, indicative of bending dominance. The other two classes exhibit a quadratic fall-off, indicating stress dominance at low wavevector (see Eq. 2.42).
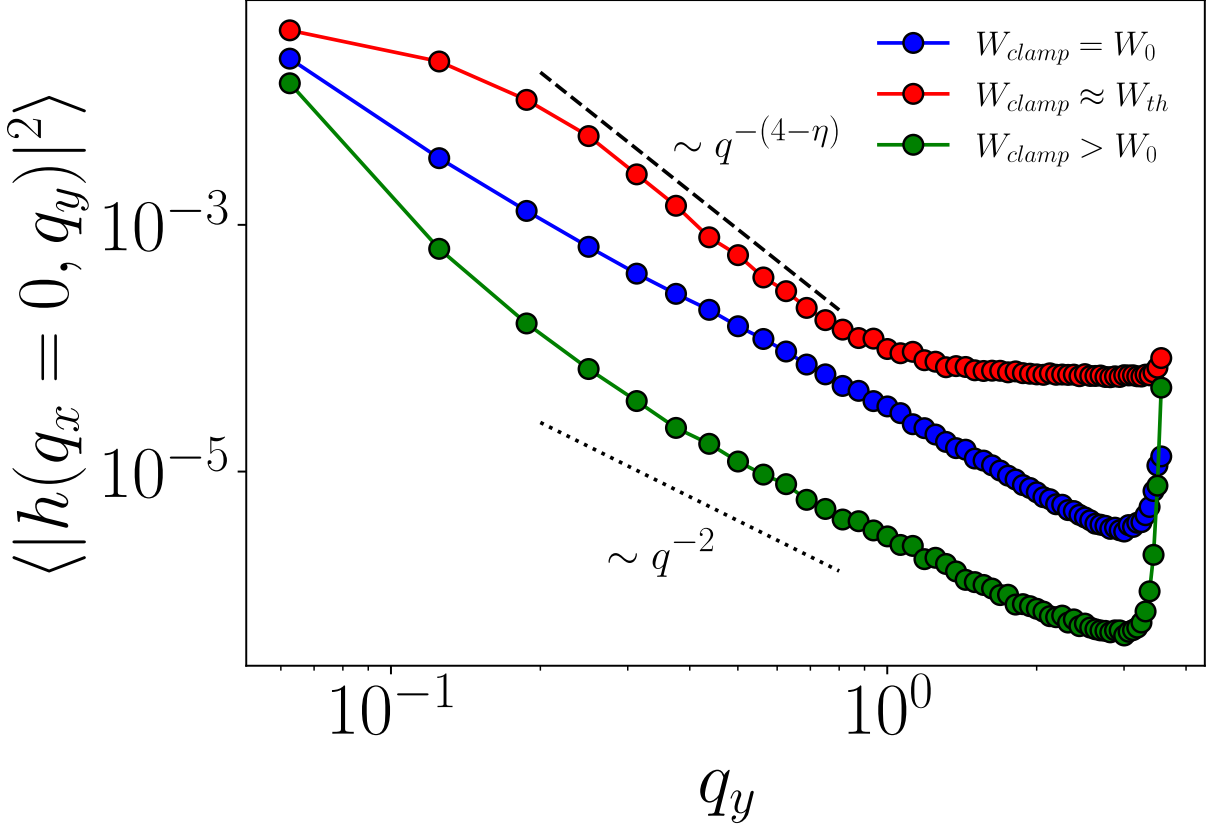
Figure 2.10: Height-height spatial correlation function, $\langle |h(q_x = 0, q_y)|^2 \rangle$, as a function of wavevector in the y-direction at fixed temperature $L/\ell_{th} \approx 3$. Clamping near the thermalized width, W_{th} (red, top, $\epsilon \approx 0.007$), leads to a scaling with power law $q^{-(4-\eta)}$ indicating a negligible stress term in Eq. 2.42. Note that $W_{th} < W_0$. For non-zero strain, we have $W_{clamp} = W_0, \epsilon \approx 0.013$ (blue, middle) and $W_{clamp} > W_0, \epsilon \approx 0.024$ (green, bottom). The correlations have quadratic scaling, indicating there is significant stress in the y direction.
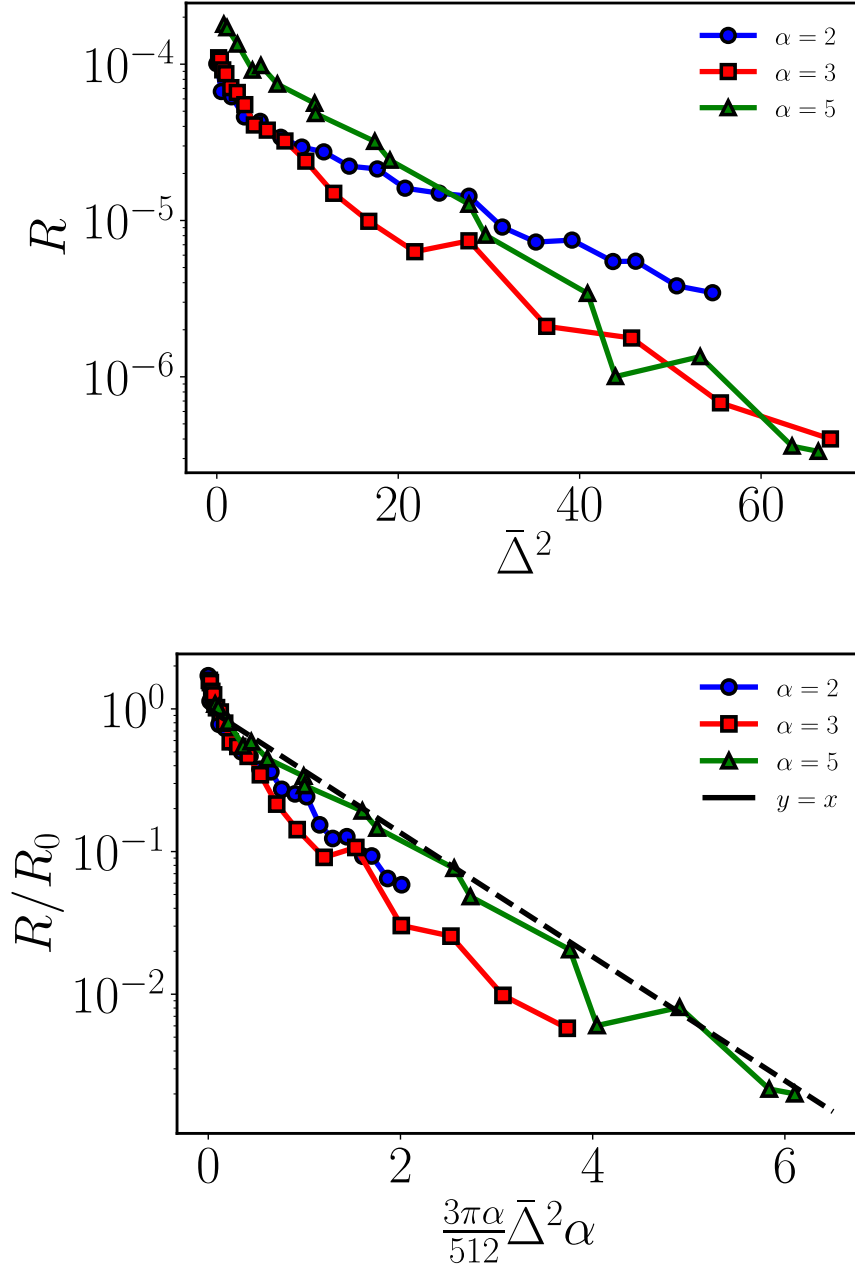
Figure 2.11: (Top) Transition rate as a function of the squared relative compression, $\bar{\Delta}$. Each curve represents a different value of the aspect ratio. (Bottom) Same data as the plot above but scaled by the R_0 obtained from fitting the top curves to a line. The x axis is scaled by the constants predicted in Eq. 2.29. We see a near collapse onto the line $y = x$, as predicted for a temperature independent Arrhenius factor.

We can now verify the predictions we found summarized in Fig. 2.4 made by the underdamped Kramers' theory along with the elastic mean field theory described in Sec. I. We first estimate $\bar{\Delta} = (\Delta - \Delta_c)/\Delta_c$ using a time average of the in-plane displacement at a variety of temperatures. The critical compression is obtained by computing the height susceptibility in analogy to the classical Ising model [36].

Eq. 2.29 predicts that the log of the transition rate falls linearly with slope $-3\pi\alpha\bar{\Delta}^2/512$. Fig. 2.11 shows a semi-log plot of the transition rate as a function of $\bar{\Delta}$: the curves are indeed linear at large $\bar{\Delta}$. Further confirmation of 2.29 is found by normalizing R by the best-fit y-intercept, R_0. This in turn isolates the boltzmann factor and focuses on the energetic contribution to the transitions. The bottom plot of Fig. 2.11 shows the normalized transition rate, R/R_0, as a function of the full argument $3\pi\alpha\bar{\Delta}^2/512$. We see a near linear collapse.

Thermal fluctuations usually promote transitions between distinct energy minima. We find instead that they suppress transitions in the $L \gg \ell_{th}$ regime, locking the membrane in one of the two tilted states. Recall that displacements are being measured with respect to a free-standing configuration where thermal fluctuations shrink the overall area: $W(T_1) < W(T_2)$ for $T_1 > T_2$. As temperature is increased the strain induced at the clamp grows, driving the system deeper into the tilted phase.

We now turn to the role of geometry as controlled by the aspect ratio. Geometrical tuning offers a very different addition to the experimental toolkit which may well be more feasible and reliable [47, 48] than precise tuning of temperature and does not require any new materials or external fields. To explore this dependence we fix a temperature in the tilted phase and simulate a set of distinct aspect ratios in the range $0.5 < \alpha < 9$ and extract the simulated dwell time, τ_{dwell}.

Fig. 2.12 shows the inverse dwell time normalized by the maximum value for a set of temperatures corresponding to $L/\ell_{th} \approx 0.9, 2.1, 2.7, 3.3$. For $L > \ell_{th}$, there is a clear
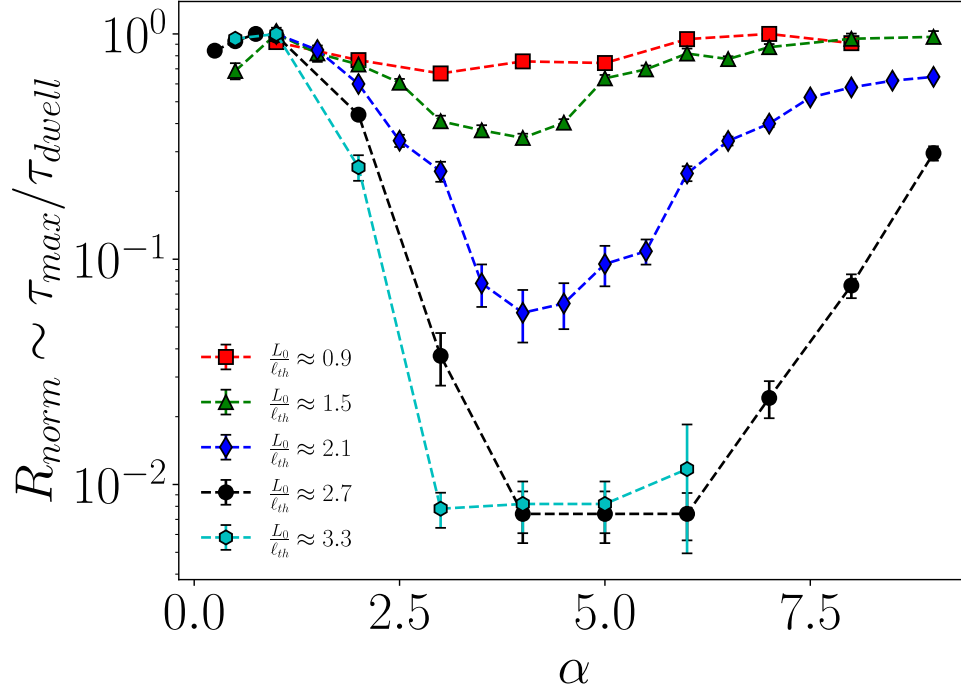
Figure 2.12: Inverse average dwell time as a function of the aspect ratio, α, for various temperatures as shown in the legend. We see a clear dependence on α, with a peak reaching nearly the entire simulation time around $\alpha = 4 - 5$, indicating the sheet is tilted for the entire simulation run. Note that for $L < \ell_{th}$ (red points), while the dwell time is non-zero, it is significantly lower than the thermalized curves.

α-dependence with a minimum for $\alpha \approx 4 - 5$. We can compare this to Fig. 2.4(b) where Kramers' theory also predicts this low transition-rate region. This dynamically stable basin can be interpreted as a region where elastic effects dominate over thermal fluctuations and we recover zero-temperature behavior, where the sheet is stress-locked into one of the tilted states until the aspect ratio becomes large enough. Further comparison can be found in Fig. 2.13, in which we showcase the data taken from Fig. 2.12 overlayed on top of Fig. 2.4(a). We see general agreement in the trends derived from the mean field treatment, that is a dynamically stable region surrounded by a highly dynamic region near the tilt transition point.

To summarize this chapter, we combine a one-dimensional mean-field model of a thermalized thin elastic sheet with cantilever boundary conditions and Kramers' transition
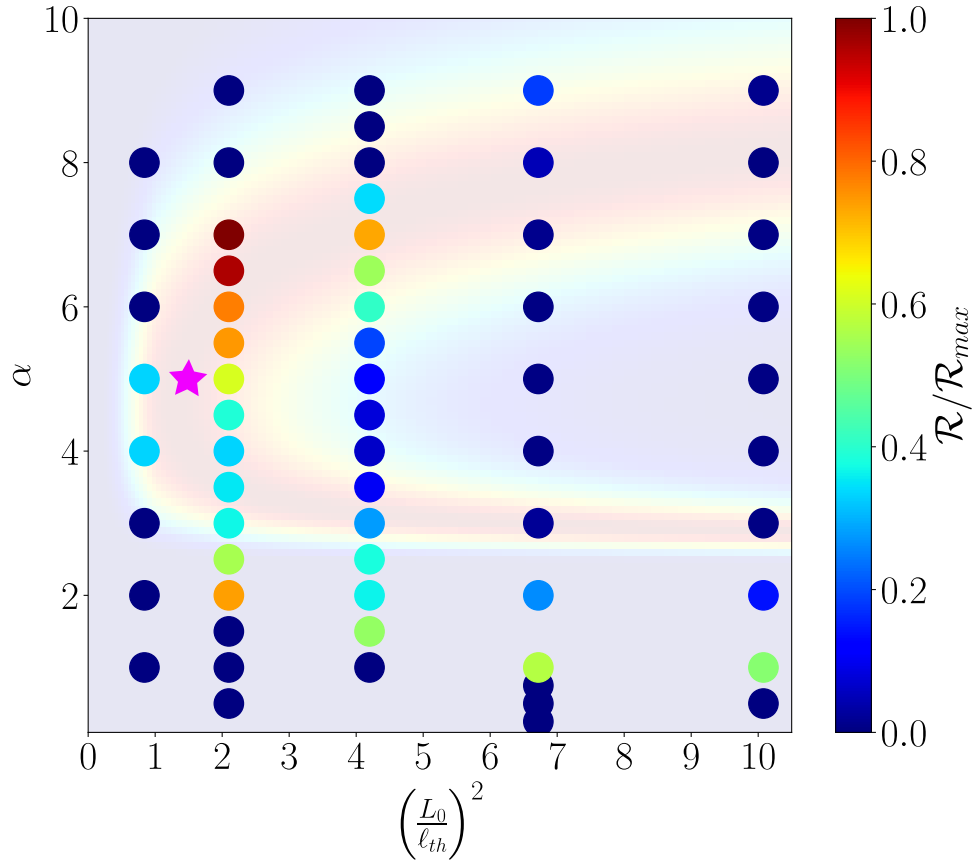
Figure 2.13: Density plot of the transition rate as a function temperature and aspect ratio as obtained from molecular dynamics data. Comparing this plot to Fig. 2.4 (shown as the background colors) we see general agreement with the high rates (red) localized in two regions of α, separated by a dynamically stable region (blue). For reference, the magenta star in the plot denotes the location of a graphene sample of the same size ($L \approx 50$ Å) at room temperature.

state theory, to analyze the transition dynamics of the tilted state in the regime where the width exceeds the length ($\alpha > 1$). Renormalization of the elastic constants due to thermal fluctuations beyond the thermal lengthscale leads to a cancellation of temperature in the Boltzmann factor of the transition probability, leaving a dominant dependence on the aspect ratio. Implicit temperature dependence enters via the relative compression $\bar{\Delta}$, slowing the dynamics and suppressing transitions between the two degenerate tilted states. Below the critical crumpling transition, the transition rate is low, locking the system in one of the two tilted phases. A key role is played by the effective stress at the

clamp with respect to a free thermalized sheet.

The predictions of Kramers theory are verified by analyzing the variation of the transition rate with the compression $\bar{\Delta}$. The transition rate dependence in the transition rate exhibits the expected Arrhenius behavior $\sim \exp\left(-C\bar{\Delta}^2\right)$ with $C = 3\pi\alpha/512$.

The temperature ranges where we observe the behavior studied here are currently beyond standard 2D-metamaterials such as micron-scale room temperature graphene. Perforated sheets and other kirigami-like structures [49] which lower the bare bending rigidity and enhance bending fluctuations, as well as permitting new bending configurations, may allow the observation of tilt and its dynamics in experimentally realizable systems. In particular geometric control of the dynamical switching exhibited by the elastic sheets studied here should have rich applications in micro- and nanoelectromechanical systems (MEMS/NEMS) [50, 51].

Chapter 3

Topologically Stable Braids in Biaxial Nematic Systems

This chapter will cover the topology half alluded by the title of this thesis. Topological concepts may arise in the study of thermalized membranes, especially when you delve deeper into the differential geometry of sheets embedded in spaces with codimension 1, however, in the case of the thermalized cantilever, geometrical frustration at the clamp became the dominating effect. Thus, to showcase the use of topology in soft condensed matter, I will focus on a completely different system.

Chapter 1 briefly the biaxial nematic system as an extension of the usual uniaxial nematics that have been thoroughly studied in the field. Compared to uniaxial nematics, the topology of the biaxial phase is considerably richer. In this chapter, I will begin with a more detailed look at the topology of the biaxial system and the entanglement of defects that arise from it. I will then introduce a classification that serves as an extension of mathematical braid theory and takes advantage of the unique defect interactions of this system to create topologically stable structures. Then we will look at the colored braid theory through examples of allowed complex structures that can be formed and how it

applies to links. This chapter will conclude with comparisons to experimental structures found in chiral nematic systems which serve as an approximation to a real biaxial system.

3.1   Classification of biaxial nematic defects

First introduced by Freiser [52] and later analyzed by Toulouse [27], the topological novelty of biaxial symmetry in ordered systems has been studied theoretically in the last 50 years [29, 32, 53]. Soon after the topological classification of singular defects in biaxial systems was elucidated. Recall from the introductory chapter of this thesis that the classification of defect lines is governed by the fundamental group of the order parameter space, which, for systems with biaxial symmetry is

$$\mathcal{M} = SO(3)/D_2, \tag{3.1}$$

the space of all 3-dimensional rotations, $SO(3)$, that obey the symmetry of the rectangle, D_2. In contrast to uniaxial nematics, whose fundamental group algebra is Abelian (the integers in 2-dimensions or $\mathbb{Z}_2$ in three dimensions), the fundamental group of biaxial nematics is non-Abelian and is in fact given by the quaternion group,

$$\pi_1[SO(3)/D_2] = \mathbb{Q} = \{1, -1, i, -i, j, -j, k, -k\}. \tag{3.2}$$

In fact, the quaternion group is the smallest non-Abelian group that arises by modding out a discrete group from the rotation group [29]. The multiplication table for the group elements of Q_8 is given in Table 3.1.

One of the principal consequences of the loss of commutativity in the fundamental is the loss of path independence. Mathematically speaking, the leads to paths with similar endpoints to be related via inner automorphisms. Physically, this means that the

×	1	−1	i	−i	j	−j	k	−k
1	1	−1	i	−i	j	−j	k	−k
−1	−1	1	−i	i	−j	j	−k	k
i	i	−i	−1	1	k	−k	−j	j
−i	−i	i	1	−1	−k	k	j	−j
j	j	−j	−k	k	−1	1	i	−i
−j	−j	j	k	−k	1	−1	−i	i
k	k	−k	j	−j	−i	i	−1	1
−k	−k	k	−j	j	i	−i	1	−1

Table 3.1: Multiplication table of the quaternion group elements $\mathbb{Q}$. Conjugacy class assignments are highlighted by different colors.

one-dimensional defects are no longer classified via the group elements of $\pi_1[SO(3)/D_2]$ [29, 54]. Instead, the conjugacy classes of the fundamental group classify the topologically distinct line defects in systems with non-Abelian fundamental groups. These classes are represented pictorially in Table 3.1 as colors. The quaternion group can be partitioned into 5 conjugacy classes

$$\mathbb{Q} = \{1\} \cup \{-1\} \cup C_i \cup C_j \cup C_k \tag{3.3}$$

where $C_i = \{\pm i\}$, $C_j = \{\pm j\}$, $C_k = \{\pm k\}$, each corresponding to one of the conjugacy classes. One can interpret the defect class $C_{i/j/k}$ as a defect texture in which there is a singularity in all symmetry directions except the direction corresponding to $i/j/k$. Examples of defects of class C_k (singular in both i but non-singular in j) as well as a non-removable -1 disclination are shown in Fig. 3.1 [1]. One important thing to note is that from symmetry of the coloring of Table 3.1, we can see that the conjugacy classes are additive or Abelian. This can be seen easier if we look at the addition table for the

---

[1] Note that Fig. 3.1(a) and Fig. 3.1(b) can be continuously interchanged by a local π rotation of each triad about the horizontal axis since they belong to the same conjugacy class. They are, however, topologically distinguishable as group elements by their winding numbers - one can transform into the other by circumnavigation around a third defect, as shown in Fig. 3.2
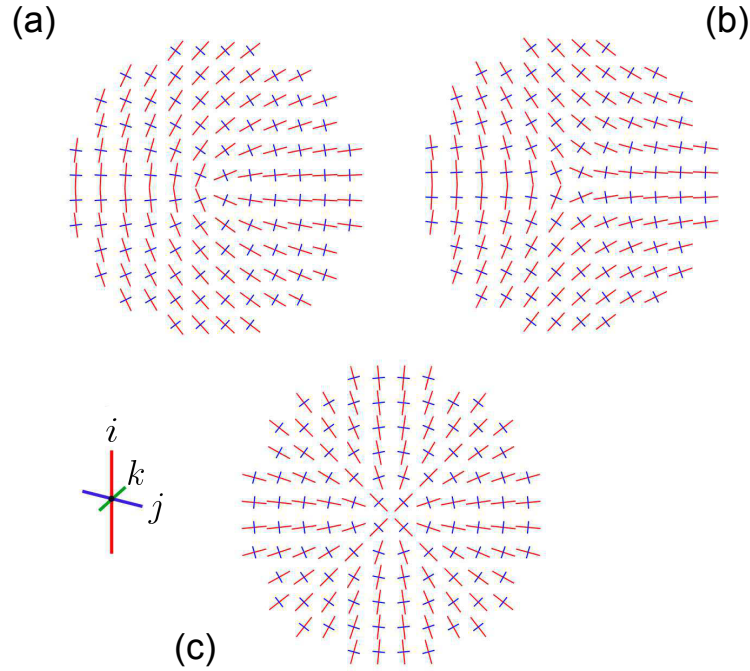
conjugacy classes of the quaternions, Table 3.2.

Figure 3.1: (a) $+k$ representative of the C_k class, forming a $1/2$ disclination in both the i and j fields and nonsingular in k. Escaping into the third dimension (discontinuously) transforms into the $+1/2$ equivalents of the C_i and C_j classes. (b) $-k$ representative of the C_k class, forming a $-1/2$ disclination in i and j and nonsingular in k. Similarly, escaping into the third dimension gives the C_i and C_j equivalents. (c) One of the three representatives of the -1 class of defects. Note that the usual escape into the third dimension in either i or j axes results in another (singular) representative of the -1 class, unlike in uniaxial nematics, where the same transformation removes the singularity.

Naively, the fact that we go from a non-Abelian fundamental group structure to classification via the Abelian conjugacy structure may seem like there is no longer an interesting structure left in biaxial defects. However, the non-Abelian path dependence remains in the conjugacy structure in the form of ambiguous results or "channels" as referred to in the context of non-Abelian anyon fusion [31]. That is, when combining two defects belonging to the same class, the resulting defect is either $+1$ or -1, and the

$+$	$+1$	-1	C_i	C_j	C_k
$+1$	$+1$	-1	C_i	C_j	C_k
-1	$+1$	$+1$	C_i	C_j	C_k
C_i	C_i	C_i	$2(+1) \oplus 2(-1)$	$2C_k$	$2C_j$
C_j	C_j	C_j	$2C_k$	$2(+1) \oplus 2(-1)$	$2C_i$
C_k	C_k	C_k	$2C_j$	$2C_i$	$2(+1) \oplus 2(-1)$

Table 3.2: Multiplication table for the conjugacy classes of $\mathbb{Q}$. Note that combining two defects belonging to the same class produces an ambiguous result, $2(+1) \oplus 2(-1)$, where the 2 indicates the degeneracy of the result (see Table 3.1), in which case the actual result is determined by the path taken to combine the two initial defects.

result depends on the path taken to combine the defects. Fig. 3.2 is an example of two such paths. In the presence of a third defect, such as C_k, we can form two non-homotopic curves, c_1 and c_2, that are possible path histories. The path given by c_1 avoids the third defect and leads to the two defects annihilating, which is algebraically equivalent to $+1$. The path given by c_2 is equivalent to the composition $c_1 \circ c_3$, which braids the left defect around the top defect along c_3 and then takes c_1 to combine the defects. This total path leads to a -1 defect line, meaning that the act of braiding changes the composition of the defect without changing its topological classification under the lens of the fundamental group.

Arguably of more importance is the result of braiding two non-Abelian defects around each other. A loop drawn around the crossing can be deformed up to homotopy to show that the configuration is equivalent to the commutator of the two defect classes [32, 29, 55].

To see this, suppose we take two defects $\alpha, \beta \in \mathbb{Q}$ and braid them around each other as shown in Fig. 3.3(a). In order to figure out the topological classification of the effective defect generated by the braid we may draw a loop, c, around the middle braid (see Fig. 3.3(a)). We may continuously deform c in such a way that we can form the collection of loops shown in Fig. 3.3(b). We recall that a loop around defect lines defines
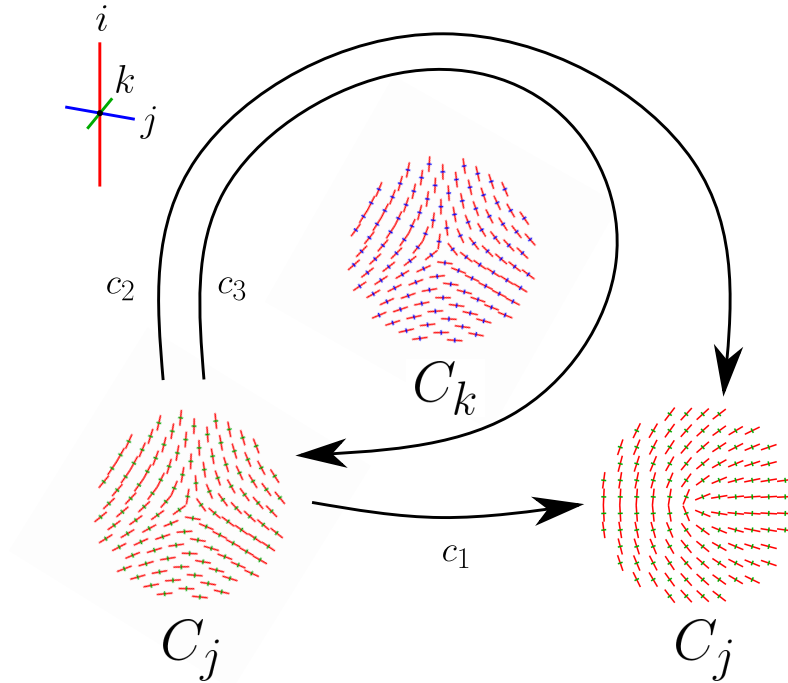
Figure 3.2: Fusion of two defects belonging to the same class, showing the path dependence of the resulting defect. The top path braids the defect around a third defect belonging to a different class, C_k, which continuously rotates the director structure of the defect without changing it's conjugacy class resulting in a -1 defect. The bottom path avoids the third defect, resulting in annihilation.

the topological charge of the defect, so each of these loops signify different factors of the corresponding defect charge. In other words, if we were to pull apart the braid, the effective defect charge formed in the middle can be read off from the loops in Fig. 3.3(b) and it corresponds to the commutator

$$[\alpha, \beta] = \alpha\beta\alpha^{-1}\beta^{-1}. \tag{3.4}$$

One can check that due to the structure of the quaternion group, this commutator can only result in either ± 1. The trivial result occurs when α and β belong to the same conjugacy class or one of the ± 1 classes. On the other hand, when the two lines belong

to different conjugacy classes, we obtain the non-trivial result, -1. This leads to the ability to form non-trivial entangled structures that are topologically stable to external fluctuations.
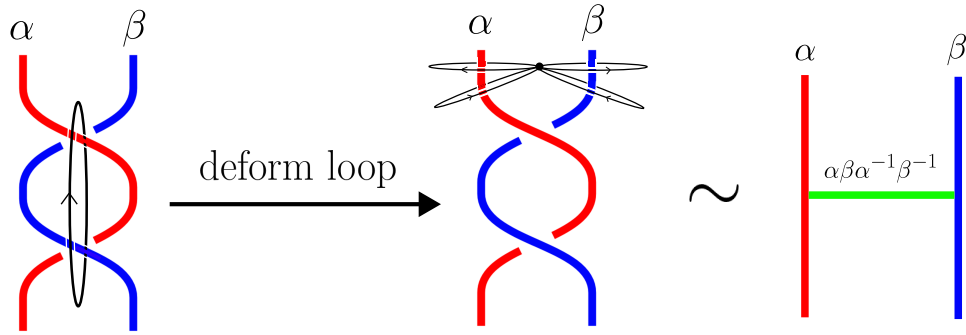

Figure 3.3: Braided structure formed by two defect lines of conjugacy classes α and β. Black loop classifies the homotopy class of the braided crossing. The black loop can be isotopically deformed to the equivalent set of 4 loops shown which reveals that pulling the lines apart results in a third defect of charge given by the commutator of the two initial defects, $[\alpha, \beta] = \alpha\beta\alpha^{-1}\beta^{-1}$.

This example of the topological entanglement of two disclination lines is one of the key signatures of non-Abelian behavior in a system. We extend on the idea of the left side of Fig. 3.3 where we can think of two connected trivalent junctions of the type $(\alpha, \alpha, [\alpha, \beta])$ and $(\beta, \beta, [\alpha, \beta])$ and define other trivalent junctions based on the algebra of the group $\mathbb{Q}$, that being the cyclic property $ij = k$ and the square property $i^2 = j^2 = k^2 = -1$. Diagramatically, we represent the three types of junctions as shown in Fig. 3.4.

These junctions provide another signature of the non-Abelian fundamental group for biaxial like systems. Additionally, we can use these as fundamental building blocks to form more complex structures.

Amongst the possible complex structures, there are non-trivial links and networks. The simplest possible network can be realized minimally with two junctions. Take, for example, a (λ, τ, χ)-junction. One can take two legs and connect them on the third leg,
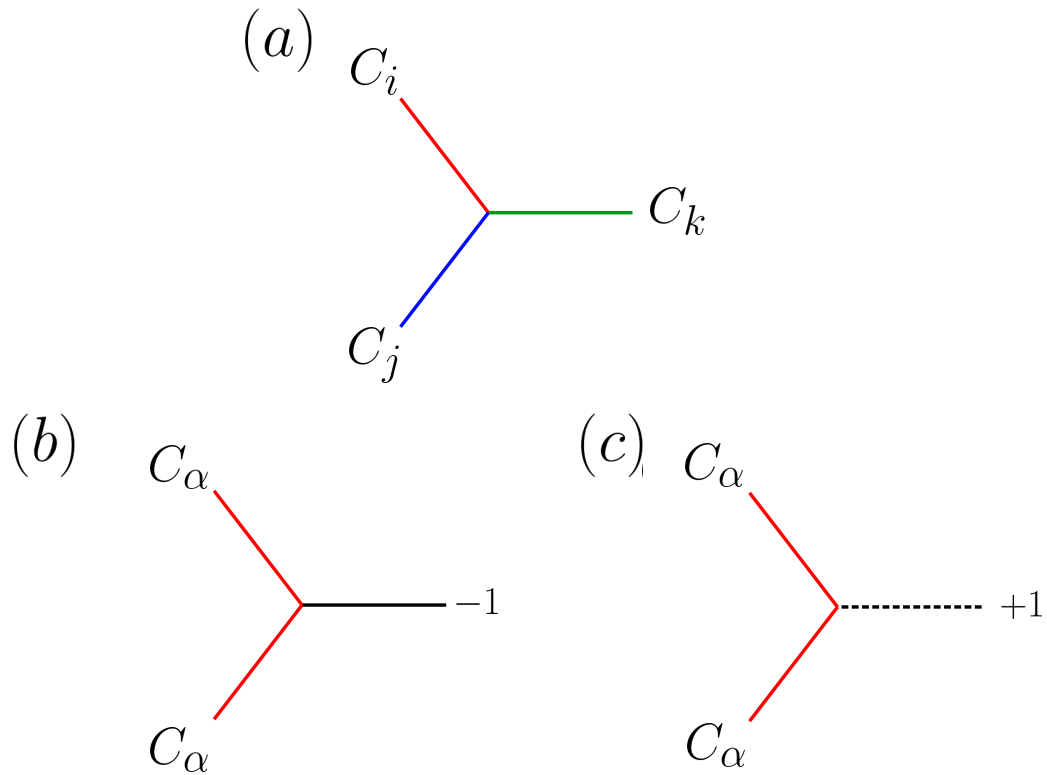
Figure 3.4: Three classes of trivalent junctions formed from the quaternion algebra. (a) Junction consisting of three disclinations belonging to three distinct conjugacy classes (b-c) Junctions that represent the path-dependent result of combining two disclinations in the same conjugacy class, $C_i^2 = +1 \oplus -1$, respectively. Note that similar junctions as (b) and (c) exist for C_j and C_k classes.

creating a closed two-junction structure (see Fig. 3.5(c)).

Here we focus on more complex structures. One such structure can be realized from the entanglement viewpoint as follows: considering several defect lines of alternating defect classes, we then perform the braid operation shown in Fig. 3.5(a). This structure is topologically equivalent to the set of junctions shown in Fig. 3.5(b). Such a structure can then be repeated to form an arbitrarily long hexagonal network, which can be seen as either a network or a braid. In practice, implementation of a network of this kind will have the topology shown in Fig. 3.5, although the geometry may not the exactly hexagonal. This is due to energetic differences in the elastic tension of each defect line.
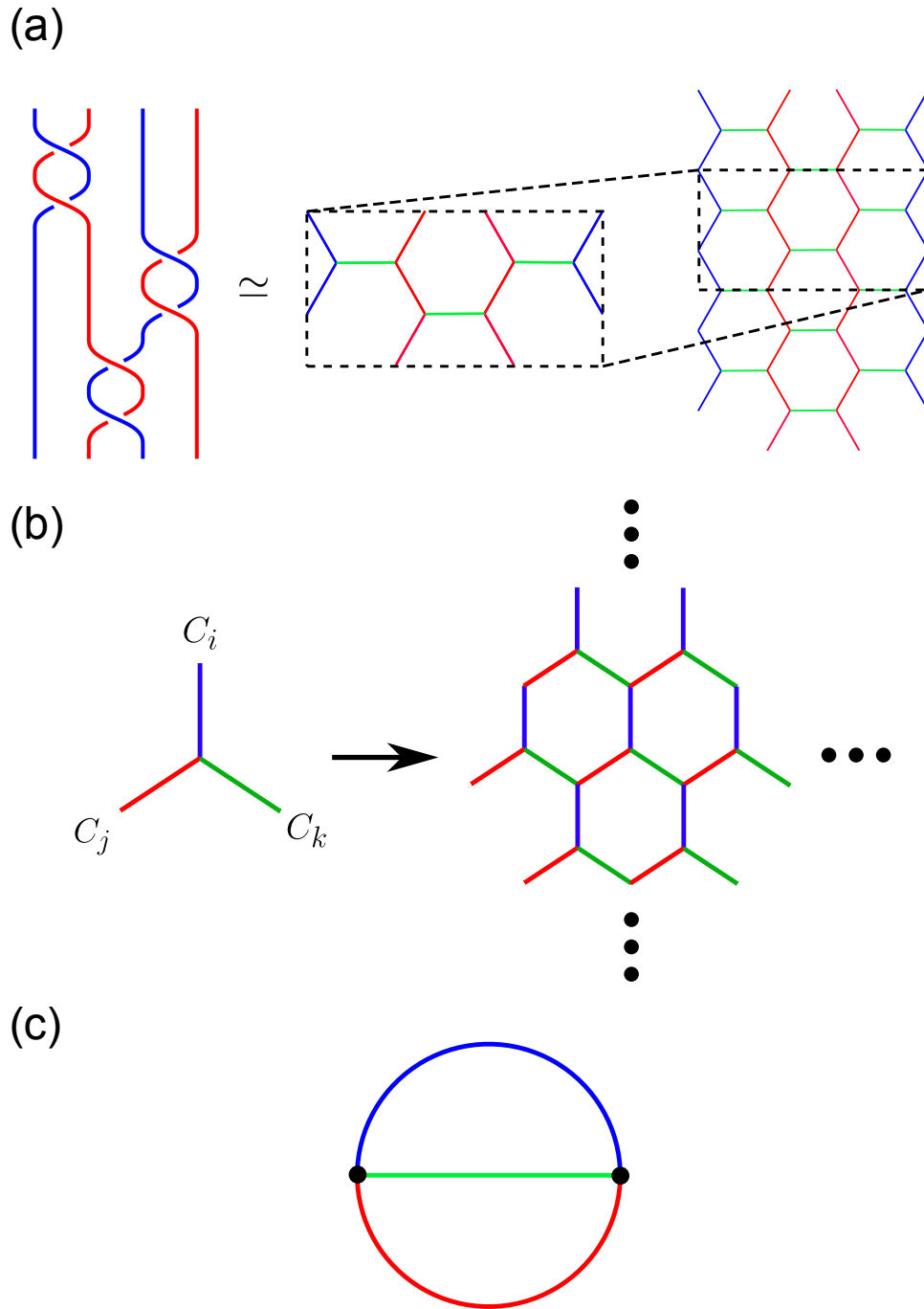
(a)

(b)

(c)

Figure 3.5: (a) Braided structure of four defect lines belonging to two different con-jugacy classes gives rise to a topologically equivalent network "unit cell" where the green line belongs to the -1 class. This unit cell can be repeated to form a junction network (right). (b) A stable junction of three defect lines belonging to separate con-jugacy classes also generates a unit cell for more complex lattice structures (right). (c) Simplest possible connected structure made from connecting all the free ends from the junction in (b) together.

An experimental verification requires a suitable biaxial system. Recent work on the phases of molecular-colloidal systems has shown that they are biaxial even in the very dilute "colloidal-gas" phase [56]. This allows for a biaxial interpretation of CLCs. Chiral systems also admit a stable braid structure in the form of a kink; a half-braided $\lambda\tau$ pair [57]. We will touch upon the chiral nematic system and its biaxial signature later in this chapter.

Note that Fig. 3.5(a) admits a braid interpretation. This braid makes use of the simple entangled structure introduced in Fig. 3.3, however, we can have more complex braids that can be topologically stable in the non-Abelian algebra. Classical mathematical braid theory does not assign types to different strands as works in analogy to physical braiding of strands. However, here we need a way to distinguish strand types and to allow for reconnections in the case where we have two strands of the same type physically entangled. To do so, we device an extension to classical braid theory and apply it to the algebra of the quaternions to determine the topological stability of not only braids, but also links.

3.2   Topological stable structures in Biaxial nematics – Colored Braid theory

We work in analogy with classical braid theory[2] and define our "colored" braid group on n strands, denoted $\mathcal{B}_n(\mathcal{C})$ where the set $\mathcal{C}$ is a a set of m colors. The color set $\mathcal{C}$, mathematically speaking, is a group whose conjugacy classes will label the strands of a braid in $\mathcal{B}_n(\mathcal{C})$. We can then construct the colored braid group on n strands and m colors, $\mathcal{B}_n(\mathcal{C})$, via a family of colored braid generators. These can be defined as $\left\{ \sigma_i^{(\alpha,\beta)} \right\}_{i=1,\dots,n-1}^{\alpha,\beta\in\mathcal{C}}$

---

[2]see Appendix E for a brief review

where

$$\sigma_i^{(\alpha,\beta)} = \quad \overset{i^{(\alpha)} \quad (i+1)^{(\beta)}}{\text{\Large{\char`X}}} \tag{3.5}$$

and $i^{(\alpha)}$ is the i-th strand decorated by color α. We can then see that the inverse of this generator is then

$$\left(\sigma_i^{(\alpha,\beta)}\right)^{-1} \equiv \left(\sigma_i^{-1}\right)^{(\beta,\alpha)} = \quad \overset{i^{(\beta)} \quad (i+1)^{(\alpha)}}{\text{\Large{\char`X}}} \tag{3.6}$$

which can be easily visually verified:

$$\sigma_i^{(\alpha,\beta)} \left(\sigma_i^{(\alpha,\beta)}\right)^{-1} = \tag{3.7}$$

$$= \tag{3.8}$$

$$= \tag{3.9}$$

$$= \left(\sigma_i^{(\alpha,\beta)}\right)^{-1} \sigma_i^{(\alpha,\beta)}. \tag{3.10}$$

Here we have used the definition of the identity in within this group which is intuitively given by n undeformed strands:
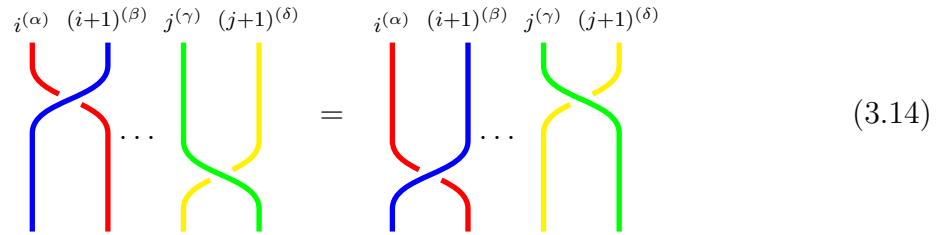
$$1_n = \quad \Big|\Big| \tag{3.11}$$

As in the regular Artin braid group (see Appendix E), we must establish genera-

tor relations in order to ensure we can perform braid moves without breaking isotopy invariance. Using the colored generators, these are
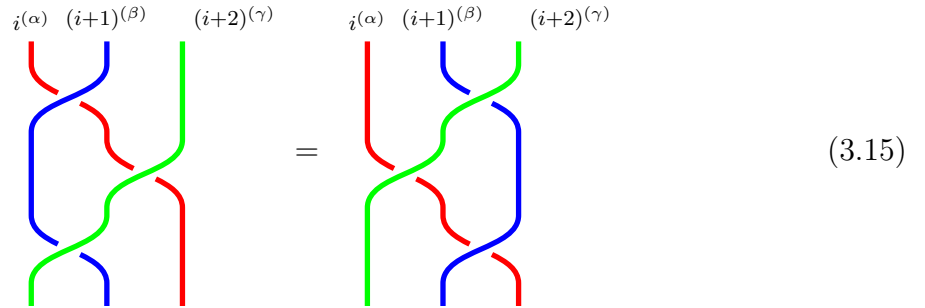
$$\sigma_i^{(\alpha,\beta)}\sigma_j^{(\gamma,\delta)} = \sigma_j^{(\gamma,\delta)}\sigma_i^{(\alpha,\beta)}, \qquad \text{for } |i-j| \geq 2 \tag{3.12}$$

$$\sigma_i^{(\alpha,\beta)}\sigma_{i+1}^{(\alpha,\gamma)}\sigma_i^{(\beta,\gamma)} = \sigma_{i+1}^{(\beta,\gamma)}\sigma_i^{(\alpha,\gamma)}\sigma_{i+1}^{(\alpha,\beta)}, \tag{3.13}$$

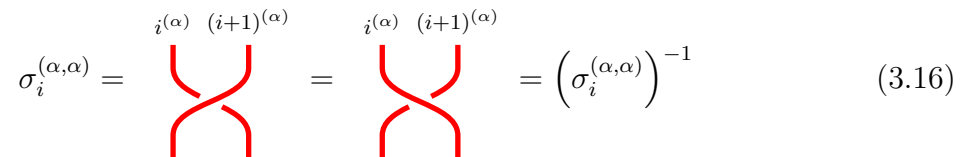for $\alpha, \beta, \gamma, \delta \in \mathcal{C}$, or, diagrammatically,

$$\tag{3.14}$$

$$\tag{3.15}$$

which establish the far commutativity and allowed moves in braids.

In addition to the usual relations, we have to impose a constraint that allows for crossings to be reversed if two strands have the same color. Note that we are relating a defect's conjugacy class to a strand's color. We can impose this constraint on the generators as follows

$$\sigma_i^{(\alpha,\alpha)} = \quad = \quad = \left(\sigma_i^{(\alpha,\alpha)}\right)^{-1} \tag{3.16}$$

or, multiplying both sides by $\sigma_i^{(\alpha,\alpha)}$,

$$\left(\sigma_i^{(\alpha,\alpha)}\right)^2 = \quad\overset{i^{(\alpha)}\ (i+1)^{(\alpha)}}{\underset{}{}} \quad = \quad\overset{i^{(\alpha)}\ (i+1)^{(\alpha)}}{\underset{}{}} \quad = \quad\overset{i^{(\alpha)}\ (i+1)^{(\alpha)}}{\underset{}{}} \quad = 1_2 \qquad (3.17)$$

.

We can now form the group $\mathcal{B}_n(\mathcal{C})$ via the group presentation

$$\mathcal{B}_n(\mathcal{C}) = \left\langle \sigma_1^{(\alpha_1,\alpha_2)}, \ldots, \sigma_n^{(\alpha_{n-1},\alpha_n)} \,\middle|\, 3.14, 3.15, 3.17, \, \alpha_1, \ldots, \alpha_n \in \mathcal{C} \right\rangle \qquad (3.18)$$

We mentioned that this mathematical description of non-Abelian braids can also help us describe links made up of the same non-Abelian strands. This can be seen through the notion of braid closures which for braid $\mathcal{B}$ is denoted $\operatorname{tr}\mathcal{B}$. For this, we need to define a sense of *purity*. Pure braids are braids that have the same ordering of strands at the start and end of the braid. However, here we don't need to impose this strong sense of purity. Instead, we require only the colors of the braid to match at the endpoints of the braid. We will refer to a colored braid with such property as simply as a *colored pure* braid. Consider the most simple non-trivial colored pure braid. The most basic non-trivial link can be obtained via the closure (connecting strands the first strand on top to the first strand on the bottom and second strand to second strand and so on) of the braid described above. The result of closing the braid above is none other than the

Hopf link[3]:

$$\mathrm{tr}\left(\begin{matrix} \alpha & \beta \\ & \end{matrix} \right) = \qquad\qquad (3.19)$$

which, depending on the particular conjugacy classes that defects α and β belong to, may or may not become unlinked.

It is easy to see that every pure colored braid $\mathcal{B}$ has a link representation given by $L = \mathrm{tr}\,\mathcal{B}$. But is the reverse true? A major result of classical braid theory linking braids to links is known as *Alexander's theorem*, which states that any oriented link can be deformed to be the closure of a braid [59]. Alexander's theorem only proves the existence of such braid but to obtain the braid, one must resort to algorithms, one of such being the Yamada-Vogel algorithm [60]. Here, we will present a modified version of the Yamada-Vogel algorithm to admit colored braids.

Suppose we have a colored link L. We begin by assigning each crossing of L a sign $\pm$ based on the following convention:

$$ = +, \qquad = - \qquad\qquad (3.20)$$

. We then put the split every crossing into two arcs, minding orientation and ignoring color combinations (see Fig. 3.6). This should result in k oriented circles (maybe of mixed colors). Connect circles that were joined by a crossing using an edge that will carry a tuple $(\eta, \vec{c})$, where η is the sign of the original crossing, and $\vec{c}$ is a color "vector" written as $\vec{c} = (\alpha, \beta)$ where α, β are the colors of the two strands that made up the original

---

[3]Technically there will be a mismatch in orientations when one looks at the fundamental group loop assignments of each strand before and after the crossing, however the example is instructive to show the idea behind closures. For more details see [58].
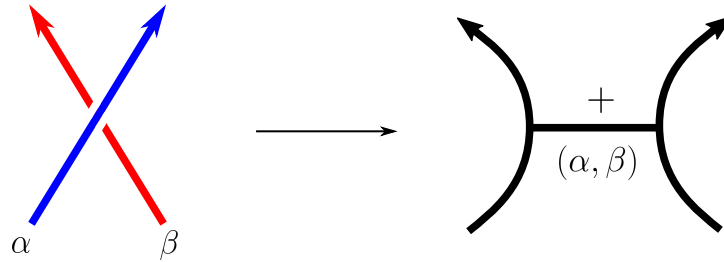
crossings.

Figure 3.6: Splitting process used to obtain Seif(L).

The resulting graph is the modified *Seifert graph*, Seif(L), of L. This will be made up of multiple oriented circles connected by edges. We say two circles are *coherent* if they are (a) connected by an edge, (b) nested and in the same orientation, or (c) un-nested and oriented in the opposite direction. Otherwise they're are incoherent. The goal is to make every circle coherent. If two circles C_i and C_j are incoherent, we can draw a line, ℓ, between the two. We perform a reducing move by merging C_i and C_j along ℓ and create a nested coherent partner inside the merged circle, connected to the outer circle with edges perpendicular to ℓ, carrying opposite signs and appropriate color vector (see Fig. 3.7).
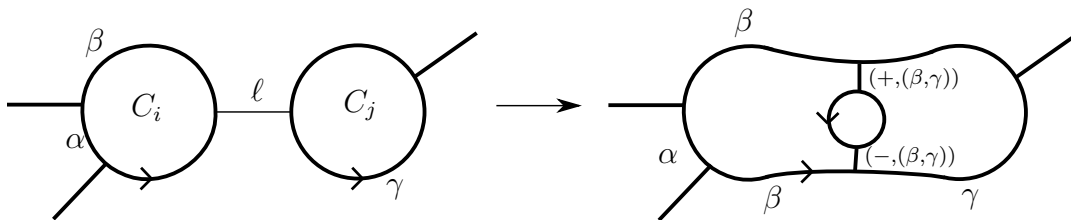
Figure 3.7: Reducing move turning a pair of incoherent circles into a coherent pair.

The previous move is equivalent to a Reidemeister move that eliminates the incoherent pair and performing the move helps determine the appropriate color vector for the internal edges. We repeat this process until all circles are coherent. We can then perform "changes of infinity" to nest all the circles (see Fig. 3.8) The final structure will be a series of nester

64
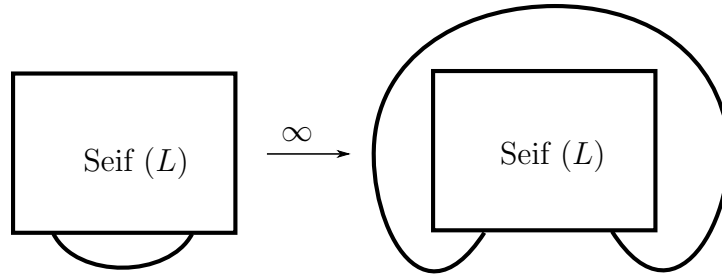
Figure 3.8: Change of infinity move

Seifert circles from which the braid word can be read out. The number of circles is the braid index, or number of strands, and an edge with sign η and color vector $\vec{c}$ connecting circles C_i and C_{i+1} correspond to the braid generator $\left(\sigma_i^{\vec{c}}\right)^{\eta}$. The resulting braid word is the braid representation of L.

Take as an example the Whitehead link (Fig. 3.9), which under the algebra of $\mathbb{Q}$ is trivial. Its Seifert circle representation is given in Fig. 3.10
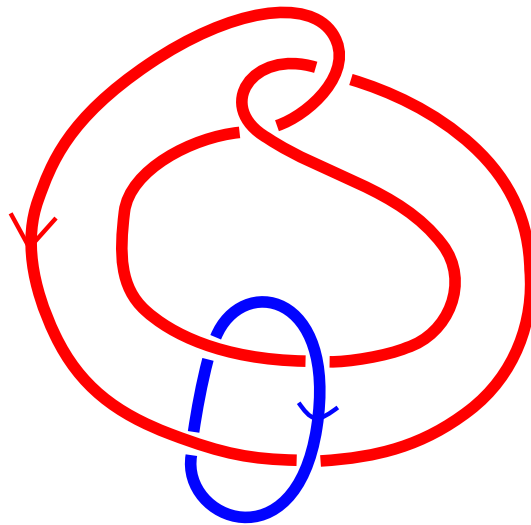
Figure 3.9: Colored Whitehead link

Figure 3.10: Seifert circle representation of the colored Whitehead link

The corresponding braid word is then:

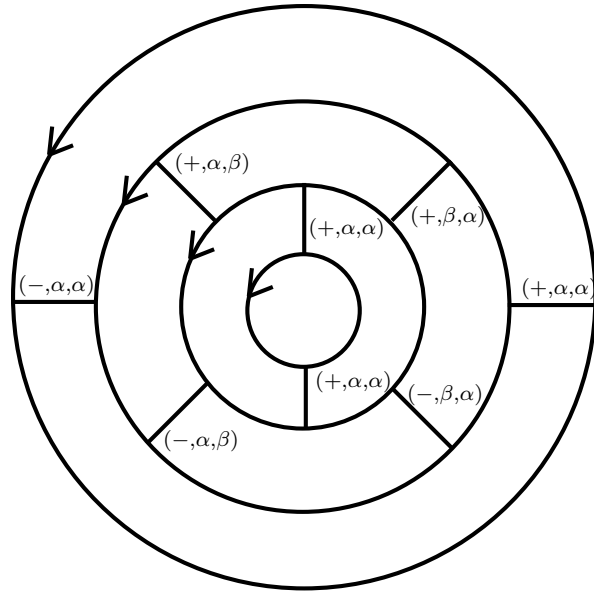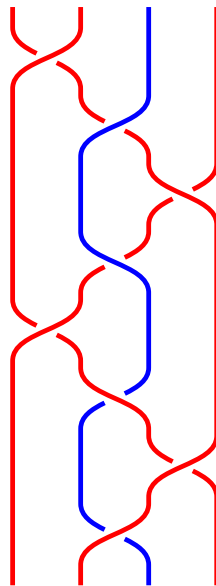$$\sigma_1^{(\alpha,\alpha)}\sigma_2^{(\alpha,\beta)}\left(\sigma_3^{(\alpha,\alpha)}\right)^{-1}\left(\sigma_2^{(\alpha,\beta)}\right)^{-1}\sigma_1^{(\alpha,\alpha)}\left(\sigma_2^{(\beta,\alpha)}\right)^{-1}\sigma_3^{(\alpha,\alpha)}\sigma_2^{(\beta,\alpha)} \tag{3.21}$$

which corresponds to the following braid:

Now that we have a braid word for the link, we should be able to apply the colored braid relations established by the presentation 3.18. We know that the whitehead link is trivial under our biaxial relations, so the braid should reduce to the identity under the closure. Also, note that we will be taking advantage of the fact that we are working with the closure of the braid, which allows us to "transport" sections of the braid along the trace strands and move them from the bottom to the top of the braid (or vice versa). This calculation, although tedious, is relatively simple and is deferred to the appendix (Appendix G).

This theory of colored braids is useful in giving a seemingly diagrammatic problem, an algebraic structure that can be easily computed whether by hand or by some algebraic solver. As of recent, there have been attempts at mathematically classifying knots and links defined over some non-Abelian group [58, 61]. However, they are quite limited in structure, due to the self-connected nature of links. While the latter extends the theory from links to spatial graphs which account for crossings of defects, the former only looks at topologically stable linked structures with no interactions.

3.3   Experimental Realizations

There have been countless experimental efforts to find or synthesize a pure biaxial system since its theoretical inception. However, the success of such efforts has been contested by the liquid crystal community.

One of the systems that have been often cited as having biaxial symmetry are chiral nematic liquid crystals or CLCs (see Fig. 1.9 and the end of Chapter 1 for an introduction). CLCs have a local ground state configuration that is clearly biaxial. That is, there exist three orthogonal directions $(\mathbf{n}, \mathbf{P}, \mathbf{n} \times \mathbf{P})$, defined by the molecular director, the pitch direction, and their cross product respectively. In literature, these are often assigned the

labels, $(\boldsymbol{\lambda}, \boldsymbol{\chi}, \boldsymbol{\tau})$ This set of fields spans a local biaxial triad and thus provides a direct connection to the elasticity the pure biaxial model [62, 63, 64]. While the ground states are topologically identical, excitations upon this ground states will deviate from the pure biaxial model. However, the locally biaxial CLC should provide a decent approximation and testing ground for non-Abelian properties of defects.

Current work tries to establish a more concrete mapping between locally D_2 (biaxial) chiral liquid crystals (D2CLCs) by relating the tensorial and Frank-Oseen models of biaxials to yield a biaxial description of a chiral nematic system [33]. Additionally, molecular-colloidal hybrid systems exhibit unavoidable biaxiality that persists even at low colloid concentration [56] reducing to the biaxial model of Priest and Lubensky at zero concentration [65]. Here, we focus on non-colloidal D2CLCs and we treat the biaxial interpretation of CLCs as an approximation that is exact on the ground state manifold.

Recall that one of the signatures of the non-Abelian quaternion algebra is the existence of junctions categorized as in Fig. 3.4. Simulations of D2CLCs reveal stable structures in the form of junctions consisting of defects in all three of the (λ, τ, χ) fields. These junctions are found to be both topologically and energetically stable for the chosen simulation parameters that mimic real D2CLC systems. These simulated junctions come in two categories: "L"-shaped and "T"-shaped (see Fig. 3.11(a) and (b), respectively), the latter of which are more reminiscent of the theoretically proposed junctions.

Experimentally, the defect junctions are realized via surface patterning techniques that fix the boundary conditions of the cell. However, the only stable junction found is of the "L" type. This is because of the anisotropy of elastic constant effectively making isolated τ-type junctions, energetically unfavorable.

To further explain this, we turn to explain the stability of the $\lambda\tau$ bound state. Inspired by the approach in Ref. [66] for a three-constant achiral model with no anisotropic term, we now analyze the bound state of parallel defect lines in the elastic model given by the
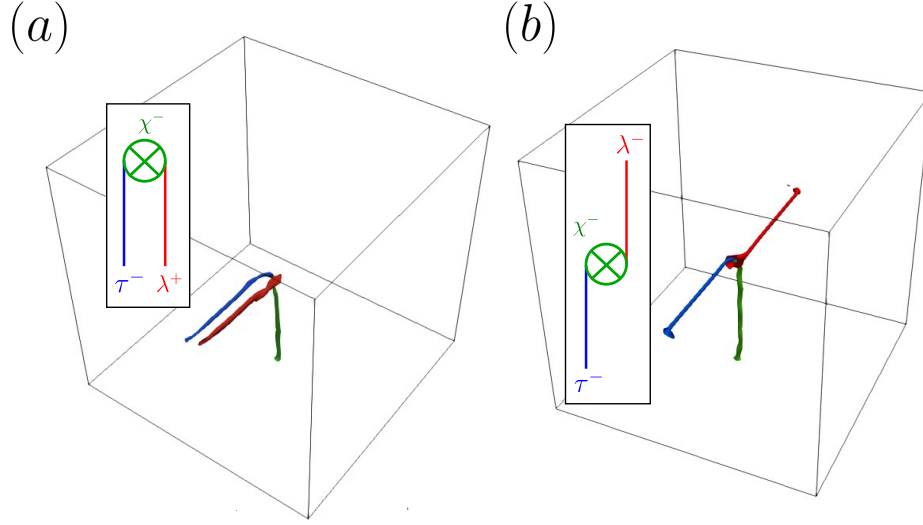
Figure 3.11: Numerically simulated $\chi/\lambda/\tau$ 3-fold junctions for the cases (a) "L"-shaped $\tau^-\lambda^+ \longleftrightarrow \chi^-$ and (b) "T"-shaped $\tau^- \longleftrightarrow \chi^-\lambda^-$ with their respective diagrams shown. The results are obtained from minimization of the Landau-de Gennes energy. Simulations performed by J.S. WU [33].

standard elastic model

$$f_{\text{elastic}} = \gamma_1 \partial_k Q_{ij} \partial_k Q_{ij} + \gamma_2 \partial_j Q_{ij} \partial_k Q_{ik} + \gamma_6 Q_{ij} \partial_i Q_{kl} \partial_j Q_{kl} \tag{3.22}$$

with Q_{ij} given by Eq. 1.22. In addition to the anisotropy provided by γ_6 we include the lowest order chiral term

$$f_{\text{chiral}} = \gamma_4 \epsilon_{ijk} Q_{il} \partial_j Q_{kl} \tag{3.23}$$

where ϵ_{ijk} is the Levi-Civita tensor [67].

Suppose we have two defect lines with topological charge q_1 and q_2 living at a distance ρ from each other in a cylindrical region $\Omega = D_R \times [0, L]$ where D_R is a disc of radius R. The region of interest away from the defect core with radius r_c is the annular region $r_c \ll r \ll R$. Here, the Q-tensor may be continuously deformed to satisfy the sliding boundary condition $\partial_r Q_{ij} = 0$ which allows us to assume that the order parameter mostly depends on the azimuthal angle. The elastic free energy density can then be

approximated as

$$f_{elastic} \approx \frac{f(\phi)}{r^2} + \frac{g(\phi)}{r} \qquad (3.24)$$

where $f(\phi)$ is the angular dependence of the expansion of the γ_1, γ_2, and γ_6 terms in Eq. 3.22 with the addition of the chiral term. Similarly, $g(\phi)$ is the angular dependence for the chiral γ_4 term. The free energy can now be approximated by integrating over the volume of Ω which, for convenience, can be split into three terms:

$$\mathcal{F} = \mathcal{F}_{q_1} + \mathcal{F}_{q_2} + \mathcal{F}_{q_3}. \qquad (3.25)$$

The first two terms are identical up to the exchange $q_1 \leftrightarrow q_2$ and represent the individual energies of each defect. The radial integrals for these two terms are calculated in the annulus $r_c < r < \rho$ surrounding each defect line and take the form

$$\mathcal{F}_{q_{1,2}} \approx \int_0^L dz \int_0^{2\pi} d\phi \int_{r_c}^{\rho} r dr \left(\frac{f(\phi)}{r^2} + \frac{g(\phi)}{r} \right) \qquad (3.26)$$

$$= \gamma_1 L S^2 K_{q_{1,2}}^{(1)} \ln \left(\frac{\rho}{r_c} \right) + \gamma_4 L S^2 (\rho - r_c) K_{q_{1,2}}^{(6)}. \qquad (3.27)$$

Similarly, the third term is computed over the annular region $\rho < r < R$ surrounding the bound state

$$\mathcal{F}_{q_3} \approx \int_0^L dz \int_0^{2\pi} d\phi \int_{\rho}^{R} r dr \left(\frac{f(\phi)}{r^2} + \frac{g(\phi)}{r} \right) \qquad (3.28)$$

$$= \gamma_1 L S^2 K_{q_3}^{(1)} \ln \left(\frac{R}{\rho} \right) + \gamma_4 L S^2 (R - \rho) K_{q_3}^{(4)}, \qquad (3.29)$$

where we have defined the elastic constants obtained from the azimuthal integrals:

$$\bar{K}_{q_i}^{(1)} \equiv F_{q_i}^{(1)}\left(\frac{T}{S}, \frac{\gamma_2}{\gamma_1}\right) + \frac{\gamma_6}{\gamma_1}SF_{q_i}^{(6)}\left(\frac{T}{S}\right) \tag{3.30}$$

$$\equiv K_{q_i}^{(1)} + \frac{\gamma_6}{\gamma_1}SK_{q_i}^{(6)} \tag{3.31}$$

$$K_{q_i}^{(4)} \equiv G_{q_i}\left(\frac{T}{S}\right) \tag{3.32}$$

Additionally, upon defining the elastic energy losses:

$$\Delta\bar{K}^{(1)} \equiv \bar{K}_{q_1}^{(1)} + \bar{K}_{q_2}^{(1)} - \bar{K}_{q_3}^{(1)} \tag{3.33}$$

$$\Delta K^{(4)} \equiv K_{q_1}^{(4)} + K_{q_2}^{(4)} - K_{q_3}^{(4)}. \tag{3.34}$$

The energy then becomes:

$$\mathcal{F} = \gamma_1 S^2 L\left[\Delta\bar{K}^{(1)} \ln\left(\frac{\rho}{r_c}\right) + K_{q_3}^{(1)} \ln\left(\frac{R}{r_c}\right)\right]$$
$$+ \gamma_4 S^2 L\left[\Delta K^{(4)}(\rho - r_c) + K_{q_3}^{(4)}(R - r_c)\right], \tag{3.35}$$

The energy may now be minimized to find that there exists a minimum at separation

$$\rho_{min} = -\frac{\gamma_1 \Delta\bar{K}^{(1)}}{\gamma_4 \Delta K^{(4)}} \tag{3.36}$$

and the second derivative evaluated at this point is

$$\left.\frac{\partial^2\mathcal{F}}{\partial\rho^2}\right|_{\rho_{min}} = -\frac{\gamma_4^2(\Delta K^{(4)})^2}{\gamma_1\Delta\bar{K}^{(1)}}. \tag{3.37}$$

which requires $\Delta\bar{K}^{(1)} < 0$ or, in other words, defect repulsion for ρ_{min} to truly be a minimum.

Recall that the sign of γ_4 determines the handedness of the system. In the case that $\gamma_4 > 0$, $\rho_{min} > 0$ requires $\Delta K^{(4)} > 0$. On the other hand, if $\gamma_4 < 0$, we must have $\Delta K^{(1)} < 0$. Seemingly, the sign of the $\Delta K^{(4)}$ term changes based on the handedness, however, if we instead focus on the sign of the product $\gamma_4 \Delta K^{(4)}$, we see that it is required to be positive in both cases. This must be the case because unlike the constants $\bar{K}_{q_i}^{(1)}$, which have some recollection of the elastic moduli γ_1 and γ_6, the $K_{q_i}^{(4)}$ is agnostic to the elastic dependence of the system as seen in Eq. 3.32. Thus, it is more appropriate to consider the sign of $\gamma_4 \Delta K^{(4)} > 0$ for a minimum to exist in the repulsive case, with $\Delta \bar{K}^{(1)} < 0$.

Unlike the achiral non-anisotropic case, where the repulsion condition leads to the energy being minimized when the defects are as far apart as possible, here we have a minimum separation distance that is stabilized within the bounds of the medium by none other than the elastic tension provided by the intrinsic chiral nature of the bulk. This agrees with the observation of bound states of λ and τ defect pairs in the D2CLCs.

We can further compare this to the braided achiral non-anisotropic case in which there is a stable minimum radius. However, the tension that creates the bound state in that case is provided by an extrinsic chirality generated by physically braiding the two defects.

Appendix A

Derivation of the effective elastic theory of membranes

We start with the in full elastic free energy of the thin elastic sheet

$$\mathcal{F}[h(\mathbf{x}), \mathbf{u}(\mathbf{x})] = \int d^2\mathbf{x} \left(\frac{\kappa}{2}(\nabla^2 h)^2 + \mu u_{ij}^2 + \frac{\lambda}{2}u_{kk}^2 \right) \tag{A.1}$$

where $h(\mathbf{x})$ is the out of plane displacement and the non-linear strain tensor $u_{ij} = (\partial_i u_j + \partial_j u_i + \partial_i h \partial_j h)/2$. Note that the in plane displacement modes, $u_i(\mathbf{x})$, appear quadratically in the free energy above. This means we can integrate out u_i from the free energy to derive an effective theory in the out-of-plane modes. That is, we can write

$$\mathcal{F}_{\text{eff}}[h(\mathbf{x})] = -k_B T \ln \int \mathcal{D}u_i \, e^{-\mathcal{F}[h(\mathbf{x}), \mathbf{u}(\mathbf{x})]/k_B T} \tag{A.2}$$

where T is the temperature and k_B is the Boltzmann constant.

We proceed using the method laid out in [13] and define a vector potential given by

$$\mathcal{A}_{ij}(\mathbf{x}) = \frac{1}{2}\partial_i h \partial_j h \tag{A.3}$$

which is a rank-2 symmetric tensor that can be decomposed into longitudinal and transverse parts as follows,

$$\mathcal{A}_{ij} = \frac{1}{2}\left(\partial_i v_j + \partial_j v_i\right) + P_{ij}^T \Phi(\mathbf{x}) \tag{A.4}$$

where $\mathbf{v}$ is some vector appropriate to the decomposition, $P_{ij}^T = \delta_{ij} - \partial_i \partial_j / \partial^2$ is the transverse projection operator, and $\Phi(\mathbf{x})$ is some scalar field. Note that we can find Φ by applying the projection P_{ij}^T to both sides of Eqn. A.4 and using the fact that $(P^T)^2 = \mathbf{1}$ to obtain

$$\Phi(\mathbf{x}) = \frac{1}{2}P_{ij}^T \partial_i h \partial_j h \tag{A.5}$$

We can now rewrite the strain tensor in terms of these transverse and logitudinal modes:

$$u_{ij} = \frac{1}{2}\left(\partial_i u_j + \partial_j u_i + \partial_i v_j + \partial_j v_i\right) + P_{ij}^T \Phi \tag{A.6}$$

$$= \frac{1}{2}\left(\partial_i \bar{u}_j + \partial_j \bar{u}_i\right) + P_{ij}^T \Phi, \tag{A.7}$$

where we defined a shifted displacement $\bar{u}_i = u_i + v_i$. We can now redefine the effective energy in terms of these shifted variables as follows,

$$\mathcal{F}_{eff}[h(\mathbf{x})] = -k_B T \ln \int \mathcal{D}\bar{\mathbf{u}} \, \mathcal{D}u_{ij}^0 \, e^{-\mathcal{F}[\langle(\mathbf{x}), \mathbf{u}(\mathbf{x})]} \tag{A.8}$$

We can now proceed by expanding the strain tensor into its Fourier components and

separate the $\mathbf{q} = 0$ components

$$u_{ij}(\mathbf{x}) = u_{ij}^0 + A_{ij}^0 + \sum_{q \neq 0} \left\{ \frac{i}{2} \left[q_i \bar{u}_j(\mathbf{q}) + q_j \bar{u}_i(\mathbf{q}) \right] + P_{ij}^T \Phi(\mathbf{q}) \right\} e^{i\mathbf{q}\cdot\mathbf{x}} \qquad (A.9)$$

and we plug into the stretch component of the free energy A.1, which I will expand term by term. Starting with the μ term,

$$\int d^2\mathbf{x} \, u_{ij}^2$$

$$= 2(u_{ij}^0 + \mathcal{A}_{ij}^0) \sum_{q \neq 0} \left(\frac{i}{2} \left[q_i \bar{u}_j(\mathbf{q}) + q_j \bar{u}_i(\mathbf{q}) \right] + P_{ij}^T \Phi(\mathbf{q}) \right) \int d^2\mathbf{x} \, e^{i\mathbf{q}\cdot\mathbf{x}}$$

$$+ \sum_{q,q' \neq 0} \left(\frac{i}{2} \left[q_i \bar{u}_j(\mathbf{q}) + q_j \bar{u}_i(\mathbf{q}) \right] + P_{ij}^T \Phi(\mathbf{q}) \right) \left(\frac{i}{2} \left[q_i' \bar{u}_j(\mathbf{q}') + q_j' \bar{u}_i(\mathbf{q}') \right] + P_{ij}^T \Phi(\mathbf{q}') \right)$$

$$\times \int d^2\mathbf{x} \, e^{i(\mathbf{q}+\mathbf{q}')\cdot\mathbf{x}} + \int d^2\mathbf{x} \, (u_{ij}^0 + A_{ij}^0)^2 \qquad (A.10)$$

$$= \sum_{q \neq 0} \left(\frac{i}{2} \left[q_i \bar{u}_j(\mathbf{q}) + q_j \bar{u}_i(\mathbf{q}) \right] + P_{ij}^T \Phi(\mathbf{q}) \right) \left(-\frac{i}{2} \left[q_i \bar{u}_j(-\mathbf{q}) + q_j \bar{u}_i(-\mathbf{q}) \right] + P_{ij}^T \Phi(-\mathbf{q}) \right)$$

$$+ A_{sheet}(u_{ij}^0 + A_{ij}^0)^2 \qquad (A.11)$$

$$= A_{sheet}(u_{ij}^0 + \mathcal{A}_{ij}^0)^2 + \sum_{q \neq 0} \left[\frac{1}{2} \left(q^2 |\bar{u}_i(\mathbf{q})|^2 + q_i q_j \bar{u}_i(\mathbf{q}) \bar{u}_j(-\mathbf{q}) \right) + |\Phi(\mathbf{q})|^2 \right] \qquad (A.12)$$

and, similarly, the λ term becomes

$$\int d^2\mathbf{x} \, \bar{u}_{kk}^2 = \int d^2\mathbf{x} \, \bar{u}_{ii} \bar{u}_{jj}$$

$$= 2(u_{ii}^0 + \mathcal{A}_{ii}^0) \sum_{q \neq 0} \left(i q_j \bar{u}_j(\mathbf{q}) + P_{jj}^T \Phi(\mathbf{q}) \right) \int d^2\mathbf{x} \, e^{i\mathbf{q}\cdot\mathbf{x}}$$

$$+ \sum_{q,q' \neq 0} \left(i q_i \bar{u}_i(\mathbf{q}) + P_{ii}^T \Phi(\mathbf{q}) \right) \left(i q_j' \bar{u}_j(\mathbf{q}') + P_{jj}^T \Phi(\mathbf{q}') \right) \int d^2\mathbf{x} \, e^{i(\mathbf{q}+\mathbf{q}')\cdot\mathbf{x}}$$

$$+ \int d^2\mathbf{x} \, (u_{kk}^0 + \mathcal{A}_{kk}^0)^2 \qquad (A.13)$$

$$= \sum_{q \neq 0} \left(i q_i \bar{u}_i(\mathbf{q}) + \Phi(\mathbf{q}) \right) \left(-i q_j \bar{u}_j(-\mathbf{q}) + \Phi(-\mathbf{q}) \right) + A_{sheet}(u_{kk}^0 + \mathcal{A}_{kk}^0)^2 \qquad (A.14)$$

$$= A_{sheet}(u_{kk}^0 + \mathcal{A}_{kk}^0)^2 + \sum_{q \neq 0} \left[q_i q_j \bar{u}_i(\mathbf{q}) \bar{u}_j(-\mathbf{q}) + 2i q_i \bar{u}_i(\mathbf{q}) \Phi(-\mathbf{q}) + |\Phi(\mathbf{q})|^2 \right].$$

(A.15)

Putting this together we obtain

$$\int d^2\mathbf{x} \, \mu \bar{u}_{ij}^2 + \frac{\lambda}{2} \bar{u}_{kk}^2$$

$$= A_{sheet} \left(\mu(u_{ij}^0 + \mathcal{A}_{ij}^0)^2 + \frac{\lambda}{2}(u_{kk}^0 + \mathcal{A}_{kk}^0)^2 \right)$$

$$+ \sum_{\mathbf{q}} \left\{ \frac{\mu}{2} q^2 |\bar{u}_i(\mathbf{q})|^2 + \frac{\mu + \lambda}{2} q_i q_j \bar{u}_i(\mathbf{q}) \bar{u}_j(-\mathbf{q}) + \frac{2\mu + \lambda}{2} |\Phi(\mathbf{q})|^2 \right\} \quad \text{(A.16)}$$

$$= A_{sheet} \left(\mu(u_{ij}^0 + \mathcal{A}_{ij}^0)^2 + \frac{\lambda}{2}(u_{kk}^0 + \mathcal{A}_{kk}^0)^2 \right)$$

$$+ \sum_{q} \left\{ \bar{u}_i(\mathbf{q}) \left[\mu q^2 \left(\delta_{ij} - \frac{q_i q_j}{q^2} \right) + (2\mu + \lambda) q^2 \frac{q_i q_j}{q^2} \right] \bar{u}_j(-\mathbf{q}) \right.$$

$$\left. + i\lambda q_i \bar{u}_i(\mathbf{q}) \Phi(-\mathbf{q}) + \frac{2\mu + \lambda}{2} |\Phi(\mathbf{q})|^2 \right\} \quad \text{(A.17)}$$

$$= A_{sheet} \left(\mu(u_{ij}^0 + \mathcal{A}_{ij}^0)^2 + \frac{\lambda}{2}(u_{kk}^0 + \mathcal{A}_{kk}^0)^2 \right)$$

$$+ \sum_{q} \left\{ \bar{u}_i(\mathbf{q}) \left[\mu q^2 P_{ij}^T + (2\mu + \lambda) q^2 P_{ij}^L \right] \bar{u}_j(-\mathbf{q}) \right.$$

$$\left. + i\lambda q_i \bar{u}_i(\mathbf{q}) \Phi(-\mathbf{q}) + \frac{2\mu + \lambda}{2} |\Phi(\mathbf{q})|^2 \right\} \quad \text{(A.18)}$$

We can now evaluate Eqn. A.8 by rewriting it into a more familiar form

$$\mathcal{F}_{eff} = \int d^2\mathbf{x} \left[\frac{\kappa}{2} (\nabla^2 h(\mathbf{x}))^2 + \frac{2\mu + \lambda}{2} \Phi(\mathbf{x})^2 \right] + k_B T \ln \int \mathcal{D}\bar{\mathbf{u}} \, e^{-\frac{1}{2}\bar{\mathbf{u}}\mathbf{M}\bar{\mathbf{u}}^T + \mathbf{J}^T \bar{\mathbf{u}}} \quad \text{(A.19)}$$

where

$$k_B T M_{ij} = \mu q^2 P_{ij}^T + (2\mu + \lambda) q^2 P_{ij}^L \tag{A.20}$$

$$k_B T J_i = i\lambda q_i \Phi(\mathbf{q}) \tag{A.21}$$

The functional integral can be evaluated using the following identity:

$$\ln \int \mathcal{D}\bar{\mathbf{u}} \, e^{-\frac{1}{2}\bar{\mathbf{u}}\mathbf{M}^{-1}\bar{\mathbf{u}}^T + \mathbf{J}^T\bar{\mathbf{u}}} = \frac{1}{2}\mathbf{J}^T\mathbf{M}^{-1}\mathbf{J} \tag{A.22}$$

which with the definitions given in Eqns. A.20 and A.21 we obtain

$$J_i M_{ij}^{-1} J_j = -k_B T \lambda^2 \frac{q_i q_j}{q^2} |\Phi(\mathbf{q})|^2 \left(\frac{1}{\mu} P_{ij}^T + \frac{1}{2\mu + \lambda} P_{ij}^L \right) \tag{A.23}$$

$$= -k_B T \lambda^2 |\Phi(\mathbf{q})|^2 \left(\frac{1}{\mu} P_{ij}^L P_{ij}^T + \frac{1}{2\mu + \lambda} P_{ij}^L P_{ij}^L \right) \tag{A.24}$$

$$= -k_B T \frac{\lambda^2}{2\mu + \lambda} |\Phi(\mathbf{q})|^2 \tag{A.25}$$

Thus, Eqn. A.19 becomes

$$\mathcal{F}_{eff} = \int d^2\mathbf{x} \left[\frac{\kappa}{2} \left(\nabla^2 h(\mathbf{x}) \right)^2 + \left(\frac{2\mu + \lambda}{2} - \frac{\lambda^2}{2\mu + \lambda} \right) \Phi(\mathbf{x})^2 \right] \tag{A.26}$$

for which, recalling the form of Φ in Eqn. A.5, we obtain the final expression for the effective height field theory:

$$\mathcal{F}_{eff}[h(\mathbf{x})] = \int d^2\mathbf{x} \left[\frac{\kappa}{2} \left(\nabla^2 h(\mathbf{x}) \right)^2 + \frac{Y}{8} (P_{ij}^T \partial_i h \partial_j h)^2 \right] \tag{A.27}$$

where we have also defined the 2D Young's modulus, Y,

$$Y = \frac{4\mu(\mu + \lambda)}{2\mu + \lambda}.$$

$$(A.28)$$

Appendix B

The thermal lengthscale, ℓ_{th}

In the previous appendix, Eq. A.27 describes an effective theory of the height field, $h(\mathbf{x},$ by integrating out the in-plane degrees of freedom. Recall that in the thermalized limit $(\ell \gg \ell_{\text{th}})$, thermal fluctuations renormalize the elastic moduli. One can then describe the effect of renormalization beyond a Gaussian, non-interacting theory by writing a *renormalized* bending rigidity,

$$\kappa_R(\mathbf{q}) \equiv \frac{1}{q^4 \langle h(-\mathbf{q})h(\mathbf{q}) \rangle}, \tag{B.1}$$

and we calculate the correlation function in the denominator perturbatively in Y.

We can diagrammatically write the non-linear stretching interaction as follows: which,

$$\frac{Y}{8} \left(P_{ij}^T \partial_i h \partial_j h \right)^2 =$$

upon expanding up to one loop gives the following expression for the renormalized bend-

ing rigidity

$$\kappa_R(\mathbf{q}) = \kappa_0 + Y_0 k_B T \int \frac{d^2 k}{(2\pi)^2} \frac{q_i P_{ij}^T(\mathbf{k}) q_j}{\kappa |\mathbf{k} + \mathbf{q}|} + \mathcal{O}(Y_0^2). \tag{B.2}$$

The integral above diverges as

$$\int d^2 k \frac{q_i P_{ij}^T(\mathbf{k}) q_j}{|\mathbf{k} + \mathbf{q}|} \sim \frac{1}{q^2} \tag{B.3}$$

for small q. This means that the first correction to the normalized bending rigidity, $\kappa_R^{(1)}$, has the form

$$\kappa_R^{(1)} \sim \frac{Y_0 k_B T}{\kappa_0 q^2}, \tag{B.4}$$

and becomes of order κ_0 when thermal fluctuations are important. The lengthscale at which this happens is then

$$q_{\text{th}} \sim \sqrt{\frac{Y_0 k_B T}{\kappa_0^2}}, \tag{B.5}$$

or,

$$\ell_{\text{th}} \sim \sqrt{\frac{4\pi^2 \kappa_0^2}{Y_0 k_B T}}, \tag{B.6}$$

which is the thermal lengthscale.

Appendix C

The Rotational Ward Identity

In the flat phase, the membrane breaks the rotational symmetry of $O(3) \times O(2)$ down to $O(3) \times O(2)/O(2)$. Upon renormalization of the elastic theory, the remaining rotational symmetry requires the full nonlinear strain tensor Eq. 1.3 to be preserved. That is, in the elastic continuum theory, the rotationally invariant term,

$$\int d^2x \, u_{kk}^2, \tag{C.1}$$

must remain invariant under the following scaling transformation:

$$\mathbf{x} \mapsto b\mathbf{x}' \tag{C.2}$$

$$\mathbf{u}(\mathbf{x}) \mapsto b^{\zeta_u}\mathbf{u}'(\mathbf{x}') \tag{C.3}$$

$$h(\mathbf{x}) \mapsto b^{\zeta_h}h'(\mathbf{x}'). \tag{C.4}$$

We can now expand:

$$u_{kk}^2 = (\partial_k u_k)^2 + \partial_k u_k \partial_j h \partial_j h + (\partial_k h \partial_k h)^2, \tag{C.5}$$

and note that we must require the first two terms to scale the same way. Applying the transformation gives the following

$$2\zeta_u - 2 = \zeta_u + 2\zeta_h - 3. \tag{C.6}$$

Recall that the mean-square fluctuations of the fields scale with anomalous dimensions

$$\langle h(\mathbf{x}) \rangle \sim L^{2\zeta_h} \tag{C.7}$$

$$\langle u_i(\mathbf{x}) \rangle \sim L^{2\zeta_u}. \tag{C.8}$$

These can also be calculated in Fourier space via their respective correlation functions:

$$\langle h(q)h(-q) \rangle = \frac{k_B T}{\kappa_0 q^{4-\eta}} \sim q^{-(4-\eta)} \tag{C.9}$$

$$\langle u_i(q)u_j(-q) \rangle = \frac{k_B T}{\mu_0 q^{2-\eta_u}} P_{ij}^T + \frac{k_B T}{(2\mu_0 + \lambda_0)q^{2-\eta_u}} P_{ij}^L \sim q^{-(2-\eta_u)}, \tag{C.10}$$

which, for a 2D membrane, gives

$$2\zeta_h = 2 - \eta \tag{C.11}$$

$$2\zeta_u = -\eta_u. \tag{C.12}$$

Thus, plugging into Eq. C.6 gives the identity required for rotational invariance in terms of the exponents η and η_u:

$$\eta_u = 2 - 2\eta. \tag{C.13}$$

Appendix D

Discussion of data analysis methods

D.1 The jackknife procedure

Given a large data set of size $N \gg 1$, we can block our data into a set of N/b data blocks of size b (similar to block spins in renormalization of the Ising model) and define an observable, O_t, at time t as the block average

$$O_{b,i} = \frac{1}{b} \sum_{t=(i-1)b+1}^{bi} O_t. \tag{D.1}$$

The jackknife procedure is a resampling method for estimating errors of functions of R observables

$$f\left(\langle O^{(1)} \rangle_\beta, \langle O^{(2)} \rangle_\beta, \dots, \langle O^{(R)} \rangle_\beta\right) \tag{D.2}$$

where $\langle O^{(i)} \rangle_\beta$ is the mean value of O_i without initialization bias (first n_{dis} data points discarded) [46, 68].

The jackknife estimate is obtained as follows:

1. Estimate the function D.2 by $f(\overline{O^{(1)}}, \overline{O^{(2)}} \dots, \overline{O^{(R)}})$ where $\overline{O^i}$ is the sample estimate

of $\langle O^{(i)} \rangle$.

2. Form jackknife blocks from the blocked data D.1 and define the block averages as follows:

$$O^{(r)}_{jack,b,i} \equiv \frac{1}{\frac{N}{b} - 1} \sum_{j \neq i} O^{(r)}_{b,j} \tag{D.3}$$

$$f_{jack,b,i} \equiv f(O^{(1)}_{jack,b,i}, O^{(2)}_{jack,b,i}, \ldots, O^{(R)}_{jack,b,i}) \tag{D.4}$$

which in simpler terms, is a block of data with one data point omitted.

3. The square error of D.4 is then

$$\overline{\Delta_f^2} = \left(\frac{N}{b} - 1 \right) \left[\frac{b}{N} \sum_{i=1}^{N/b} f_{jack,b,i}^2 - \left(\frac{b}{N} \sum_{i=1}^{N/b} f_{jack,b,i} \right)^2 \right] \tag{D.5}$$

There are other sampling methods such as bootstrapping which is a non-linear version of the jackknife, and are more useful for fitting. However, since we are only estimating errors, the jackknife should be appropriate using different runs as our jackknife blocks.

D.2   The discrete gradient

We introduce here a method of numerically calculating gradients on triangularized surfaces This is a method that is commonly implemented on various differential operators defined on meshes [69, 70], and here we apply it to compute strains on simulated sheets.

Consider a graph $G = \{V, E\}$ with vertices V coinciding with the vertices V and edges E of our simulated lattice and we define some vector field $\vec{f_i} : V \to \mathbb{R}^2$, for $i \in V$. We start by focusing on a single vertex $v_i \in V$ and its neighborhood (or star) $\mathcal{N}(v_i) = \{T_I\}_{I=1}^6$ where T_I is 1 of the 6 triangles making up the neighborhood of v_i. We then compute

the gradient defined in each triangle T_I. This is done via barycentric interpolation of the three values of f_i on the vertices T_I. The gradient at triangle T_I is given by

$$(\nabla f_{T_I})_{ij} = (f_i - f_k)\frac{(v_k - v_j)^\perp}{2A_{T_I}} + (f_j - f_k)\frac{(v_i - v_k)^\perp}{2A_{T_I}} \tag{D.6}$$

where $v^\perp$ is the 90° rotation of vector v and A_{T_I} is the area of triangle T_I. This gives a gradient tensor in the basis of the faces of G.

In order to move back to the basis of vertices we compute a weighted average over the neighborhood of vertex v and define the gradient at v as

$$(\nabla f_v)_{ij} = \frac{1}{\sum_{T_I \in \mathcal{N}(v)} A_{T_I}} \sum_{T_I \in \mathcal{N}(v)} A_{T_I}(\nabla f_{T_I})_{ij}$$

We can now compute the mesh gradient of the in-plane displacement field, u_i, as defined on the vertices of the deformed lattice. The in-plane gradient is then obtained by symmetrizing the gradient as computed above, that is, $U_{ij} = (\partial_i u_j + \partial_j u_i)/2$.

Appendix E

Brief overview of classical braid theory

Classical braid theory is built in analogy to physical braids. That is, strands that can become physically entangled by moving one strand over the other in some succession. Mathematically, this is formulated by what is known as the Artin braid group [59].

The Artin braid group on n strands, B_n is a finite group generated by the braid generators, σ_i and σ_i^{-1}, which are defined as the exchange operators on strands i and $i + 1$. Diagramatically, these are

$$\sigma_i = \quad \vcenter{\hbox{\includegraphics{braid_positive}}} \qquad\qquad\text{(E.1)}$$

and

$$\sigma_i^{-1} = \quad \vcenter{\hbox{\includegraphics{braid_negative}}} \qquad\qquad\text{(E.2)}$$

The Artin braid group generators are subject to the following relations:

$$\sigma_i \sigma_j = \sigma_j \sigma_i \tag{E.3}$$

for $|i - j| \leq 2$ which states that crossings commute as long as they don't share a strand
and

$$\sigma_i \sigma_{i+1} \sigma_i = \sigma_{i+1} \sigma_i \sigma_{i+1} \tag{E.4}$$

for all $1 \leq i < n$. These are simply mathematical expressions that establish physical
isotopy that is to be expected from physical strands.

The Artin braid broup is then written as the presentation

$$B_n = \langle \sigma_i, \sigma_i^{-1} | \sigma_i \sigma_j = \sigma_j \sigma_i, \sigma_i \sigma_{i+1} \sigma_i = \sigma_{i+1} \sigma_i \sigma_{i+1} \rangle. \tag{E.5}$$

Appendix F

Proof of $\pi_1(SO(3)/D_2) \simeq \mathbb{Q}$

The fact that biaxial nematic systems have disclinations whose algebra is that of the quaternion group, $\mathbb{Q}$, is well known and quoted with confidence. However, for the sake of self-containment, here we sketch the proof of the statement. In a more mathematical language, we want to prove that

$$\pi_1(SO(3)/D_2) \simeq \mathbb{Q} \tag{F.1}$$

To do so, we require the following theorem which proves useful in computing homotopy groups of coset spaces:

Theorem 1 *Let G be a simply connected Lie group with subgroup $H \leq G$ and identity component $H_0 \trianglelefteq G$. Then*

$$\pi_1(G/H) \simeq H/H_0 \tag{F.2}$$

Proof of this statement establishes an isomorphism between the fundamental group and the quotient space H/H_0 by relating the loops in G/H based at H to paths in G

from a connected piece of H to the piece that contains the identity, H_0.

Theorem 1 allows one to compute $\pi_1(SO(3)/D_2)$ by lifting to a universal cover map. This is

$$SO(3) \longrightarrow SU(2) \tag{F.3}$$

$$D_2 \longrightarrow Q_8 \tag{F.4}$$

Here, the covering map sends π rotations about each symmetry axis of the rectangle, into π rotations in $SU(2)$ parametrized by the Pauli matrices. The set of such rotations forms the lift of D_2, that is

$$\{\pm 1, \pm i\sigma_x, \pm i\sigma_y, \pm i\sigma_z\} \tag{F.5}$$

which is simply the group of quaternions, $\mathbb{Q}$.

Now, applying theorem 1, we have

$$\pi_1(SO(3)/D_2) \simeq \pi_1(SU(2)/\mathbb{Q}) \simeq \mathbb{Q}/\mathbb{Q}_0 = \mathbb{Q} \tag{F.6}$$

since $\mathbb{Q}_0 = \{1\}$.

Note that in 1 this result was summarized by the short exact sequence

$$0 \longrightarrow \pi_1(SU(2)) \longrightarrow \pi_1(SU(2)/\mathbb{Q}) \longrightarrow \pi_0(\mathbb{Q}) \simeq \mathbb{Q} \longrightarrow 0 \tag{F.7}$$

which is a restatement of theorem 1 using the language of exact sequences.

Appendix G

Triviality of the Whitehead link

Here, we show the closure of the braid word 3.21 is trivial:

$$
\text{Tr}\left[\sigma_1^{(\alpha,\alpha)}\sigma_2^{(\alpha,\beta)}\left(\sigma_3^{(\alpha,\alpha)}\right)^{-1}\left(\sigma_2^{(\alpha,\beta)}\right)^{-1}\sigma_1^{(\alpha,\alpha)}\left(\sigma_2^{(\beta,\alpha)}\right)^{-1}\sigma_3^{(\alpha,\alpha)}\sigma_2^{(\beta,\alpha)}\right]
$$

$$
= \text{Tr}\left[\left(\sigma_2^{(\beta,\alpha)}\right)^{-1}\sigma_3^{(\alpha,\alpha)}\sigma_2^{(\beta,\alpha)}\sigma_1^{(\alpha,\alpha)}\sigma_2^{(\alpha,\beta)}\left(\sigma_3^{(\alpha,\alpha)}\right)^{-1}\left(\sigma_2^{(\alpha,\beta)}\right)^{-1}\sigma_1^{(\alpha,\alpha)}\right] \qquad \text{(cycle)}
$$

$$
= \text{Tr}\left[\left(\sigma_2^{(\beta,\alpha)}\right)^{-1}\sigma_3^{(\alpha,\alpha)}\sigma_1^{(\alpha,\beta)}\sigma_2^{(\alpha,\alpha)}\sigma_1^{(\beta,\alpha)}\left(\sigma_3^{(\alpha,\alpha)}\right)^{-1}\left(\sigma_2^{(\alpha,\beta)}\right)^{-1}\sigma_1^{(\alpha,\alpha)}\right] \qquad \text{(slide)}
$$

$$
= \text{Tr}\left[\left(\sigma_2^{(\beta,\alpha)}\right)^{-1}\sigma_1^{(\alpha,\beta)}\sigma_3^{(\alpha,\alpha)}\sigma_2^{(\alpha,\alpha)}\left(\sigma_3^{(\alpha,\alpha)}\right)^{-1}\sigma_1^{(\beta,\alpha)}\left(\sigma_2^{(\alpha,\beta)}\right)^{-1}\left(\sigma_1^{(\alpha,\alpha)}\right)^{-1}\right] \qquad \text{(commute)}
$$

$$
= \text{Tr}\left[\left(\sigma_2^{(\beta,\alpha)}\right)^{-1}\sigma_1^{(\alpha,\beta)}\left(\sigma_2^{(\alpha,\alpha)}\right)^{-1}\sigma_3^{(\alpha,\alpha)}\sigma_2^{(\alpha,\alpha)}\left(\sigma_2^{(\alpha,\alpha)}\right)^{-1}\left(\sigma_1^{(\alpha,\beta)}\right)^{-1}\sigma_2^{(\beta,\alpha)}\right] \qquad \text{(slide)}
$$

$$
= \text{Tr}\left[\left(\sigma_2^{(\beta,\alpha)}\right)^{-1}\sigma_1^{(\alpha,\beta)}\left(\sigma_2^{(\alpha,\alpha)}\right)^{-1}\sigma_3^{(\alpha,\alpha)}1_2^{(\alpha.\alpha)}\left(\sigma_1^{(\alpha,\beta)}\right)^{-1}\sigma_2^{(\beta,\alpha)}\right]
$$

$$
= \text{Tr}\left[\left(\sigma_1^{(\alpha,\beta)}\right)^{-1}\sigma_2^{(\beta,\alpha)}\left(\sigma_2^{(\beta,\alpha)}\right)^{-1}\sigma_1^{(\alpha,\beta)}\left(\sigma_2^{(\alpha,\alpha)}\right)^{-1}\sigma_3^{(\alpha,\alpha)}\cancel{1}_2^{(\alpha.\alpha)}\right] \qquad \text{(cycle)}
$$

$$
= \text{Tr}\left[1_2^{(\beta,\alpha)}\left(\sigma_2^{(\alpha,\alpha)}\right)^{-1}\sigma_3^{(\alpha,\alpha)}\right]
$$

$$
= \text{Tr}\left[1_2^{(\beta,\alpha)}\sigma_2^{(\alpha,\alpha)}\sigma_3^{(\alpha,\alpha)}\right]
$$

$$
= \text{Tr}\left[1_2^{(\beta,\alpha)}\right]
$$

Bibliography

[1] S. J. Streichan, M. F. Lefebvre, N. Noll, E. F. Wieschaus, and B. I. Shraiman, *Global morphogenetic flow is accurately predicted by the spatial distribution of myosin motors*, *Elife* **7** (2018) e27454.

[2] Y. Liu, X. Xue, S. Sun, N. Kobayashi, Y. S. Kim, and J. Fu, *Morphogenesis beyond in vivo*, *Nature Reviews Physics* **6** (2024), no. 1 28–44.

[3] J. Toner and Y. Tu, *Flocks, herds, and schools: A quantitative theory of flocking*, *Physical review E* **58** (1998), no. 4 4828.

[4] T. J. Byers and D. Branton, *Visualization of the protein associations in the erythrocyte membrane skeleton.*, *Proceedings of the National Academy of Sciences* **82** (1985), no. 18 6153–6157.

[5] L. D. Landau and E. Lifshitz, *The theory of elasticity*. Elsevier, 1986.

[6] A. W. Leissa, *Vibration of plates*, vol. 160. Scientific and Technical Information Division, National Aeronautics and . . . , 1969.

[7] T. Castle, Y. Cho, X. Gong, E. Jung, D. M. Sussman, S. Yang, and R. D. Kamien, *Making the Cut: Lattice Kirigami Rules*, *Physical Review Letters* **113** (Dec., 2014) 245502. Publisher: American Physical Society.

[8] B. F. Grosso and E. Mele, *Bending Rules in Graphene Kirigami*, *Physical Review Letters* **115** (Nov., 2015) 195501. Publisher: American Physical Society.

[9] M. Moshe, E. Esposito, S. Shankar, B. Bircan, I. Cohen, D. R. Nelson, and M. J. Bowick, *Kirigami mechanics as stress relief by elastic charges*, *Physical Review Letters* **122** (Jan., 2019) 048001. arXiv: 1808.00925.

[10] U. Nath, B. C. W. Crawford, R. Carpenter, and E. Coen, *Genetic Control of Surface Curvature*, *Science* **299** (Feb., 2003) 1404–1407. Publisher: American Association for the Advancement of Science.

[11] A. Elgsaeter, B. T. Stokke, A. Mikkelsen, and D. Branton, *The molecular basis of erythrocyte shape*, *Science* **234** (1986), no. 4781 1217–1223, [https://www.science.org/doi/pdf/10.1126/science.3775380].

[12] K. Svoboda, C. F. Schmidt, D. Branton, and S. M. Block, *Conformation and elasticity of the isolated red blood cell membrane skeleton*, Biophysical Journal **63** (1992), no. 3 784–793.

[13] D. Nelson, T. Piran, and S. Weinberg, *Statistical mechanics of membranes and surfaces*. World Scientific, 2004.

[14] D. Nelson and L. Peliti, *Fluctuations in membranes with crystalline and hexatic order*, Journal de Physique **48** (1987), no. 7 1085–1092.

[15] M. Katsnelson, *Graphene: Carbon in Two Dimensions*. Cambridge University Press, 2012.

[16] P. Le Doussal and L. Radzihovsky, *Self-consistent theory of polymerized membranes*, Physical Review Letters **69** (Aug., 1992) 1209–1212. Publisher: American Physical Society.

[17] P. Le Doussal and L. Radzihovsky, *Anomalous elasticity, fluctuations and disorder in elastic membranes*, Annals of Physics **392** (May, 2018) 340–410.

[18] K. Essafi, J.-P. Kownacki, and D. Mouhanna, *First-order phase transitions in polymerized phantom membranes*, Physical Review E **89** (Apr., 2014) 042101. Publisher: American Physical Society.

[19] J.-P. Kownacki and D. Mouhanna, *Crumpling transition and flat phase of polymerized phantom membranes*, Phys. Rev. E **79** (Apr., 2009) 040101.

[20] F. L. Braghin and N. Hasselmann, *Thermal fluctuations of free-standing graphene*, Phys. Rev. B **82** (July, 2010) 035407.

[21] O. Coquand, D. Mouhanna, and S. Teber, *Flat phase of polymerized membranes at two-loop order*, Physical Review E **101** (June, 2020) 062104. Publisher: American Physical Society.

[22] S. Metayer, D. Mouhanna, and S. Teber, *Three-loop order approach to flat polymerized membranes*, Physical Review E **105** (Jan., 2022) L012603. Publisher: American Physical Society.

[23] R. Abril Valenzuela, P. Z. Hanakata, and M. J. Bowick, *Geometric control of tilt transition dynamics in single-clamped thermalized elastic sheets*, Physical Review E **108** (2023), no. 4 045002.

[24] R. C. Regan, J. J. Wiman, and J. A. Sauls, *Half-quantum vortices in nematic and chiral phases of* ^{3}He, Phys. Rev. B **104** (Jul, 2021) 024513.

[25] Y. Maroudas-Sacks, L. Garion, L. Shani-Zerbib, A. Livshits, E. Braun, and K. Keren, *Topological defects in the nematic order of actin fibres as organization centres of hydra morphogenesis*, *Nature Physics* **17** (2021), no. 2 251–259.

[26] P. M. Chaikin, T. C. Lubensky, and T. A. Witten, *Principles of condensed matter physics*, vol. 10. Cambridge university press Cambridge, 1995.

[27] G. Toulouse, *Pour les nématiques biaxes*, *Journal de Physique Lettres* **38** (1977), no. 2 67–68. Publisher: Edp sciences.

[28] G. Toulouse and M. Kléman, *Principles of a classification of defects in ordered media*, *Journal de Physique Lettres* **37** (1976), no. 6 149–151.

[29] N. D. Mermin, *The topological theory of defects in ordered media*, *Reviews of Modern Physics* **51** (July, 1979) 591–648. Publisher: American Physical Society.

[30] A. Hatcher, *Algebraic topology*. Cambridge University Press, Cambridge, 2002.

[31] C. Nayak, S. H. Simon, A. Stern, M. Freedman, and S. Das Sarma, *Non-abelian anyons and topological quantum computation*, *Reviews of Modern Physics* **80** (2008), no. 3 1083–1159.

[32] V. Poenaru and G. Toulouse, *The crossing of defects in ordered media and the topology of 3-manifolds*, *Journal de Physique* **38** (1977), no. 8 887–895.

[33] J.-S. Wu, R. Abril Valenzuela, S. I. I., and M. J. Bowick, *Realization of non-abelian defect junctions and entanglement in chiral nematic systems with locally biaxial symmetry reconstruction in orientational order*, *(In preparation)* (2024).

[34] M. K. Blees, A. W. Barnard, P. A. Rose, S. P. Roberts, K. L. McGill, P. Y. Huang, A. R. Ruyack, J. W. Kevek, B. Kobrin, D. A. Muller, and P. L. McEuen, *Graphene kirigami*, *Nature* **524** (Aug., 2015) 204–207. Number: 7564 Publisher: Nature Publishing Group.

[35] R. J. Nicholl, H. J. Conley, N. V. Lavrik, I. Vlassiouk, Y. S. Puzyrev, V. P. Sreenivas, S. T. Pantelides, and K. I. Bolotin, *The effect of intrinsic crumpling on the mechanics of free-standing graphene*, *Nature Communications* **6** (Nov., 2015) 8789.

[36] P. Z. Hanakata, S. S. Bhabesh, M. J. Bowick, D. R. Nelson, and D. Yllanes, *Thermal buckling and symmetry breaking in thin ribbons under compression*, *Extreme Mechanics Letters* **44** (Apr., 2021) 101270.

[37] Z. Chen, D. Wan, and M. J. Bowick, *Spontaneous Tilt of Single-Clamped Thermal Elastic Sheets*, *Physical Review Letters* **128** (Jan., 2022) 028006. Publisher: American Physical Society.

[38] S. P. Timoshenko and J. M. Gere, *Theory of elastic stability*. Courier Corporation, 2009.

[39] A. Košmrlj and D. R. Nelson, *Response of thermalized ribbons to pulling and bending*, *Physical Review B* **93** (Mar., 2016) 125431. Publisher: American Physical Society.

[40] R. P. Feynman, R. B. Leighton, and M. Sands, *The Feynman lectures on physics*, vol. III. Basic books, 2011.

[41] L. Gammaitoni, P. Hänggi, P. Jung, and F. Marchesoni, *Stochastic resonance*, *Rev. Mod. Phys.* **70** (Jan, 1998) 223–287.

[42] R. Zwanzig, *Nonequilibrium statistical mechanics*. Oxford University Press, 2001.

[43] A. Amir, *Thinking Probabilistically: Stochastic Processes, Disordered Systems, and Their Applications*. Cambridge University Press, 2020.

[44] D. Nelson, T. Piran, and S. Weinberg, *Statistical Mechanics of Membranes and Surfaces*. WORLD SCIENTIFIC, 2nd ed., 2004.

[45] J. A. Anderson, J. Glaser, and S. C. Glotzer, *HOOMD-blue: A Python package for high-performance molecular dynamics and hard particle Monte Carlo simulations*, *Computational Materials Science* **173** (2020) 109363.

[46] D. J. Amit and V. Martin-Mayor, *Field theory, the renormalization group, and critical phenomena: graphs to computers*. World Scientific Publishing Company, 2005.

[47] A. M. v. d. Zande, R. A. Barton, J. S. Alden, C. S. Ruiz-Vargas, W. S. Whitney, P. H. Pham, J. Park, J. M. Parpia, H. G. Craighead, and P. L. McEuen, *Large-scale arrays of single-layer graphene resonators*, *Nano letters* **10** (2010), no. 12 4869–4873.

[48] P. Masih Das, G. Danda, A. Cupo, W. M. Parkin, L. Liang, N. Kharche, X. Ling, S. Huang, M. S. Dresselhaus, V. Meunier, and M. Drndić, *Controlled sculpture of black phosphorus nanoribbons*, *ACS nano* **10** (2016), no. 6 5687–5695.

[49] D. Yllanes, S. S. Bhabesh, D. R. Nelson, and M. J. Bowick, *Thermal crumpling of perforated two-dimensional sheets*, *Nature Communications* **8** (Nov., 2017) 1381. Number: 1 Publisher: Nature Publishing Group.

[50] B. Xu, P. Zhang, J. Zhu, Z. Liu, A. Eichler, X.-Q. Zheng, J. Lee, A. Dash, S. More, S. Wu, Y. Wang, H. Jia, A. Naik, A. Bachtold, R. Yang, P. X.-L. Feng, and Z. Wang, *Nanomechanical Resonators: Toward Atomic Scale*, *ACS Nano* **16** (Oct., 2022) 15545–15585. Publisher: American Chemical Society.

[51] R. Lifshitz and M. C. Cross, *Nonlinear Dynamics of Nanomechanical and Micromechanical Resonators*, in *Reviews of Nonlinear Dynamics and Complexity*, pp. 1–52. John Wiley & Sons, Ltd, 2008.

[52] M. Freiser, *Ordered states of a nematic liquid*, *Physical Review Letters* **24** (1970), no. 19 1041.

[53] G. P. Alexander, B. G.-g. Chen, E. A. Matsumoto, and R. D. Kamien, *Colloquium: Disclination loops, point defects, and all that in nematic liquid crystals*, *Rev. Mod. Phys.* **84** (Apr, 2012) 497–514.

[54] A. Hatcher, *Algebraic Topology*. Cambridge University Press, 2002.

[55] G. P. Alexander and R. D. Kamien, *Entanglements and whitehead products: generalizing kleman's construction to higher-dimensional defects*, *Liquid Crystals Reviews* **10** (2022), no. 1-2 91–97.

[56] J.-S. Wu, M. T. Lazaro, S. Ghosh, H. Mundoor, H. H. Wensink, and I. I. Smalyukh, *Unavoidable emergent biaxiality in chiral molecular-colloidal hybrid liquid crystals*, *arXiv preprint arXiv:2304.07447* (2023).

[57] I. I. Smalyukh and O. Lavrentovich, *Three-dimensional director structures of defects in grandjean-cano wedges of cholesteric liquid crystals studied by fluorescence confocal polarizing microscopy*, *Physical Review E* **66** (2002), no. 5 051703.

[58] T. Annala, R. Zamora-Zamora, and M. Möttönen, *Topologically protected vortex knots and links*, *arXiv:2204.03612 [cond-mat]* (Apr., 2022). arXiv: 2204.03612.

[59] K. Murasugi and B. I. Kurpita, *A study of braids*. No. v. 484 in Mathematics and its applications. Kluwer Academic Publishers, Dordrecht ; Boston, 1999.

[60] S. Yamada, *The minimal number of seifert circles equals the braid index of a link*, *Inventiones mathematicae* **89** (1987), no. 2 347–356.

[61] Y. Nozaki, T. Kálmán, M. Teragaito, and Y. Koda, *Homotopy classification of knotted defects in ordered media*, Feb., 2024. arXiv:2402.16079 [cond-mat].

[62] G. E. Volovik and V. P. Mineev, *Investigation of singularities in superfluid he/sup 3/ in liquid crystals by the homotopic topology methods*, *Sov. Phys. - JETP (Engl. Transl.); (United States)* **45:6** (6, 1977).

[63] M. Kleman and O. D. Lavrentovich, *Soft matter physics: an introduction*. Springer, 2003.

[64] J. Pollard and G. P. Alexander, *Contact Topology and the Classification of Disclination Lines in Cholesteric Liquid Crystals*, *Physical Review Letters* **130** (June, 2023) 228102. Publisher: American Physical Society.

[65] R. G. Priest and T. C. Lubensky, *Biaxial model of cholesteric liquid crystals*, *Physical Review A* **9** (Feb., 1974) 893–898. Publisher: American Physical Society.

[66] M. I. Monastyrskiĭ and P. V. Sasorov, *Bound states of linear defects in biaxial nematics and superfluid liquids*, *Journal of Experimental and Theoretical Physics* **102** (Jan., 2006) 149–154.

[67] L. Longa, D. Monselesan, and H.-R. Trebin, *An extension of the Landau-Ginzburg-de Gennes theory for liquid crystals*, *Liquid Crystals* **2** (Nov., 1987) 769–796. Publisher: Taylor & Francis _eprint: https://doi.org/10.1080/02678298708086335.

[68] M. E. Newman and G. T. Barkema, *Monte Carlo methods in statistical physics*. Clarendon Press, 1999.

[69] C. Mancinelli, M. Livesu, and E. Puppo, *A comparison of methods for gradient field estimation on simplicial meshes*, *Computers & Graphics* **80** (2019) 37–50.

[70] M. Meyer, M. Desbrun, P. Schröder, and A. H. Barr, *Discrete Differential-Geometry Operators for Triangulated 2-Manifolds*. Springer Berlin Heidelberg, Berlin, Heidelberg, 2003.